

1-1-2001

## The geochemistry of gold-bearing and gold-free pyrite and marcasite from the Getchell gold deposit, Humboldt County, Nevada

Kelli Diane Weaver  
*University of Nevada, Las Vegas*

Follow this and additional works at: <https://digitalscholarship.unlv.edu/rtds>

---

### Repository Citation

Weaver, Kelli Diane, "The geochemistry of gold-bearing and gold-free pyrite and marcasite from the Getchell gold deposit, Humboldt County, Nevada" (2001). *UNLV Retrospective Theses & Dissertations*. 1344.

<http://dx.doi.org/10.25669/rwv9-1zgy>

This Thesis is protected by copyright and/or related rights. It has been brought to you by Digital Scholarship@UNLV with permission from the rights-holder(s). You are free to use this Thesis in any way that is permitted by the copyright and related rights legislation that applies to your use. For other uses you need to obtain permission from the rights-holder(s) directly, unless additional rights are indicated by a Creative Commons license in the record and/or on the work itself.

This Thesis has been accepted for inclusion in UNLV Retrospective Theses & Dissertations by an authorized administrator of Digital Scholarship@UNLV. For more information, please contact [digitalscholarship@unlv.edu](mailto:digitalscholarship@unlv.edu).

## **INFORMATION TO USERS**

**This manuscript has been reproduced from the microfilm master. UMI films the text directly from the original or copy submitted. Thus, some thesis and dissertation copies are in typewriter face, while others may be from any type of computer printer.**

**The quality of this reproduction is dependent upon the quality of the copy submitted. Broken or indistinct print, colored or poor quality illustrations and photographs, print bleedthrough, substandard margins, and improper alignment can adversely affect reproduction.**

**In the unlikely event that the author did not send UMI a complete manuscript and there are missing pages, these will be noted. Also, if unauthorized copyright material had to be removed, a note will indicate the deletion.**

**Oversize materials (e.g., maps, drawings, charts) are reproduced by sectioning the original, beginning at the upper left-hand corner and continuing from left to right in equal sections with small overlaps.**

**Photographs included in the original manuscript have been reproduced xerographically in this copy. Higher quality 6" x 9" black and white photographic prints are available for any photographs or illustrations appearing in this copy for an additional charge. Contact UMI directly to order.**

**ProQuest Information and Learning  
300 North Zeeb Road, Ann Arbor, MI 48106-1346 USA  
800-521-0600**

**UMI<sup>®</sup>**



**THE GEOCHEMISTRY OF GOLD-BEARING AND GOLD-FREE PYRITE AND  
MARCASITE FROM THE GETCHELL GOLD DEPOSIT,  
HUMBOLDT COUNTY, NEVADA**

by

**Kelli D. Weaver**

**Bachelor of Science  
Ohio Wesleyan University  
1992**

**A thesis submitted in partial fulfillment  
of the requirements for the**

**Master of Science Degree  
Department of Geoscience  
College of Sciences**

**Graduate College  
University of Nevada, Las Vegas  
November 2001**

**UMI Number: 1409054**



---

**UMI Microform 1409054**

**Copyright 2002 by ProQuest Information and Learning Company.**

**All rights reserved. This microform edition is protected against  
unauthorized copying under Title 17, United States Code.**

---

**ProQuest Information and Learning Company  
300 North Zeeb Road  
P.O. Box 1346  
Ann Arbor, MI 48106-1346**



**Thesis Approval**  
The Graduate College  
University of Nevada, Las Vegas

November 21, 2001

The Thesis prepared by

Kelli D. Weaver

Entitled

The Geochemistry of Gold-bearing and Gold-free Pyrite and Marcasite  
from the Gatchell Gold Deposit, Humboldt County, Nevada

is approved in partial fulfillment of the requirements for the degree of

Master of Science

Examination Committee Chair

Dean of the Graduate College

J. W. Backlund for Margaret Rees

Examination Committee Member

Elizabeth Jacobson

Examination Committee Member

Barbara A. Rake

Graduate College Faculty Representative

## **ABSTRACT**

### **The Geochemistry of Gold-Bearing and Gold-Free Pyrite and Marcasite from the Getchell Gold Deposit, Humboldt County, Nevada**

by

**Kelli D. Weaver**

**Dr. Jean S. Cline, Examination Committee Chair  
Professor of Geoscience  
University of Nevada, Las Vegas**

Petrographic and geochemical investigations of pyrite and marcasite from the Getchell Carlin-type gold deposit show that elevated concentrations of a characteristic suite of trace metals correlate with ore-stage pyrite morphology. Secondary ion mass spectrometry analyses revealed a significant positive correlation between As and Au in ore-stage Fe-sulfide minerals. High-resolution transmission electron microscopy analyses revealed that gold-bearing Fe-sulfide crystals are arsenic-rich marcasite, rather than pyrite. These analyses failed to identify gold as microinclusions in ore-stage pyrite/marcasite, and support the conclusion that gold is present in solid solution.

Analyses reflect the chemistry of fluids responsible for precipitation of the pyrite and marcasite. Near stoichiometric, pre-ore pyrite precipitated from fluids that were not saturated in Hg, Tl, As, Cu, Au and Sb. Ore-stage pyrite textures suggest rapid precipitation from fluids that contained Hg, Tl, As, Cu, Au and Sb. Late-ore stage marcasite indicates that late fluids continued to transport significant As.

## TABLE OF CONTENTS

ABSTRACT .....	iii
LIST OF FIGURES.....	vi
LIST OF TABLES .....	viii
ACKNOWLEDGMENTS .....	ix
CHAPTER 1 INTRODUCTION.....	1
CHAPTER 2 CARLIN-TYPE GOLD DEPOSITS .....	4
Characteristics of Carlin-Type Gold Deposits .....	4
CHAPTER 3 THE GETCHELL GOLD DEPOSIT .....	7
Location and General Regional Geology .....	7
Getchell Stratigraphy .....	9
Granodiorite Intrusion.....	12
Structural Controls of the Getchell Au Deposit.....	13
Carlin-Type Gold Mineralization at Getchell.....	13
CHAPTER 4 SAMPLING AND ANALYTICAL METHODS.....	16
Petrographic Analyses .....	18
Electron Microprobe Analyses .....	18
Secondary Ion Mass Spectrometry.....	19
High-Resolution Transmission Microscopy .....	21
Cathodoluminescence.....	22
Statistical Analysis .....	22
CHAPTER 5 MINERAL PARAGENESIS .....	23
Stage 1 – Pre-Ore Stage Mineral Assemblage.....	24
Discussion of Pre-Ore Paragenesis .....	31
Stage 2 – Ore-Stage Mineral Assemblage.....	31
Discussion of Ore-Stage Paragenesis .....	44
Stage 3 – Late-Ore Stage Mineral Assemblage.....	46
Discussion of Late-Ore Stage Paragenesis.....	56



<b>CHAPTER 6 TRACE ELEMENT STUDY AND STATISTICAL EVALUATION.....</b>	<b>61</b>
Pyrite Geochemistry .....	61
Discussion of Trace Element Analyses .....	69
Statistical Analysis of Sulfide Geochemistry.....	70
Cluster Analysis of Sulfide Geochemistry.....	83
<b>CHAPTER 7 GOLD QUANTIFICATION AND LOCATION.....</b>	<b>85</b>
SIMS Analyses .....	85
SIMS Ion Mapping .....	87
SIMS Depth Profiles .....	88
SIMS Discussion .....	88
Location of Gold.....	90
TEM Analysis .....	90
<b>CHAPTER 8 DISCUSSION .....</b>	<b>92</b>
Pyrite Geochemistry.....	92
Chemical State of Au.....	93
Trace Element Substitution in Fe-Sulfide Minerals .....	94
Formation of Trace Element-Rich Fe-Sulfide Minerals .....	96
Pyrite and Marcasite Formation.....	97
Model for Fe-Sulfide Precipitation at Getchell.....	100
<b>CHAPTER 9 CONCLUSIONS .....</b>	<b>102</b>
<b>APPENDIX 1 .....</b>	<b>104</b>
List of Samples Collected from the Getchell Mine.....	105
<b>APPENDIX 2.....</b>	<b>106</b>
List of Thin Sections Prepared for EMP, SIMS, and TEM Analyses.....	107
<b>APPENDIX 3.....</b>	<b>108</b>
EMP Detection Limits .....	109
<b>APPENDIX 4.....</b>	<b>110</b>
EMP Trace Element Analyses of Sulfosalt Minerals .....	111
<b>APPENDIX 5.....</b>	<b>113</b>
EMP Trace Element Data for Fe-Sulfide Minerals .....	114
<b>APPENDIX 6.....</b>	<b>122</b>
Cluster Analysis of Sulfide Geochemistry.....	123
<b>REFERENCES .....</b>	<b>124</b>
<b>VITA .....</b>	<b>132</b>

## LIST OF FIGURES

Figure 1.	Location map showing the linear trends of both the Getchell and Carlin gold deposits.....	2
Figure 2.	Tectono-stratigraphy of Getchell mine area.....	10
Figure 3.	Cross section showing sample locations and underground mine levels of the Getchell underground mine in 1997. ....	17
Figure 4.	Transmitted light, crossed polarized light photomicrograph of C1a Calcite within vugs. ....	25
Figure 5.	Reflected light photomicrograph of P1a euhedral pyrite.....	26
Figure 6.	Reflected light photomicrograph of P1b euhedral pyrite.....	26
Figure 7.	Transmitted light, crossed polarized light photomicrograph of C1a limestone, P1a pyrite, C1b calcite and Q1 quartz.....	27
Figure 8.	Transmitted light, plane-polarized light photomicrograph of apatite. ....	28
Figure 9.	Transmitted light, plane-polarized light photomicrograph of C1b calcite .....	29
Figure 10.	Transmitted light, crossed polarized light photomicrograph of apatite inclusions within barite.....	30
Figure 11a.	Reflected light photomicrograph of P1a or b core and P2a rim.....	33
Figure 11b.	Reflected light photomicrograph of Figure 11a at lower power .....	34
Figure 11c.	BEI of P1a or b pyrite core rimmed by P2a.....	34
Figure 12.	BEI of P1a or b pyrite, rimmed by high-grade P2c pyrite/ marcasite.....	35
Figure 13.	Reflected light, photomicrograph of P2d porous pyrite/ marcasite.....	36
Figure 14.	Transmitted light, crossed polarized light photomicrograph of Q2 jasperoid .....	38
Figure 15.	Transmitted light, crossed polarized light photomicrograph of Q2a.....	39
Figure 16.	Transmitted light, crossed polarized light photomicrograph of Q2b .....	40
Figure 17a.	Transmitted light, plane-polarized light photomicrograph of Q2c.....	41
Figure 17b.	Transmitted light photomicrograph of Q2c jasperoid.....	41
Figure 18.	Cathodoluminescence image of ore-stage and late-ore stage quartz .....	42
Figure 19a.	Transmitted light, plane-polarized light photomicrograph of galkhaite crystals overgrown by late-ore stage R3 realgar .....	43
Figure 19b.	BEI of galkhaite .....	44
Figure 20.	Transmitted light, plane-polarized photomicrograph of Q3a .....	47
Figure 21.	Transmitted light, crossed polarized light photomicrograph of Q3b .....	48
Figure 22.	Cathodoluminescence image showing late-ore stage drusy quartz.....	49
Figure 23a.	Reflected light photomicrograph showing P3a euhedral and prismatic marcasite.....	50
Figure 23b.	Reflected light photomicrograph showing fine crystals of lath-shaped P3a marcasite.....	51
Figure 23c.	Reflected light photomicrograph showing P3b marcasite .....	51

Figure 24.	Transmitted light, crossed polarized light photomicrograph of realgar inclusions.....	52
Figure 25.	Reflected light photomicrograph showing textural relationships between O3 orpiment, R3 realgar, and Q3b quartz.....	53
Figure 26.	Transmitted light, crossed polarized light photomicrograph of R3 realgar with euhedral faces.....	54
Figure 27a.	Transmitted light, plane-polarized light photomicrograph showing textural relationships between P2d pyrite/marcasite, G2 galkhaite, Q2 jasperoid quartz, R3 realgar, O3 orpiment and S3 stibnite.....	55
Figure 27b.	BEI of same region as previous figure.....	55
Figure 28a.	Transmitted light, crossed polarized light photomicrograph of C3a, C3c, and possibly C3b.....	57
Figure 28b.	Cathodoluminescence image of Figure 28a .....	57
Figure 29.	Transmitted light, crossed polarized light photomicrograph of Q3c chalcedony.....	58
Figure 30.	BEI and trace element maps of P1a or b pyrite and P2a and b Fe-sulfide minerals .....	65
Figure 31.	BEI and trace element map of P1a or b pyrite and P2c Fe-sulfide minerals .....	66
Figure 32.	Trace element transect data for Figures 30 and 31.....	67
Figure 33.	Trace and major element linear regression plots for ore-stage P2a, P2b, and P2c pyrite/marcasite.....	74
Figure 34.	Trace and major element linear regression plots for ore-stage P2a, P2b, and P2c pyrite/marcasite.....	75
Figure 35.	Trace and major element linear regression plots for ore-stage P2d pyrite/marcasite .....	76
Figure 36.	Trace and major element linear regression plots for ore-stage P2d pyrite/marcasite .....	79
Figure 37.	Trace and major element linear regression plots for P2d pyrite/marcasite.....	80
Figure 38.	Trace and major element linear regression plots for P3 marcasite.....	82
Figure 39.	Mean standardized concentrations of non-ore stage and ore-stage Fe-sulfide minerals .....	84
Figure 40.	SIMS map showing concentrations of <sup>34</sup> S, <sup>75</sup> As, and <sup>197</sup> Au.....	87
Figure 41.	SIMS depth profiles .....	89
Figure 42.	TEM diffraction pattern of ore-stage Fe-sulfide mineral.....	91

## LIST OF TABLES

Table 1.	Experimental parameters for ion microprobe analyses. ....	20
Table 2.	Paragenetic sequence observed for pre-ore minerals.....	24
Table 3.	Paragenetic sequence observed for ore-stage minerals.....	32
Table 4.	Paragenetic sequence observed for late-ore minerals .....	46
Table 5.	Averages for EMP trace element data for Fe-sulfide minerals .....	62
Table 6.	EMP trace element transect data for Figures 30 and 31 .....	68
Table 7.	Correlation table for all analyzed Fe-sulfide minerals .....	71
Table 8.	Trace element correlation matrices for P1a and P1b pyrite .....	72
Table 9.	Trace element correlation matrix for P2a, P2b, and P2c pyrite/ marcasite.....	73
Table 10.	Trace element correlation matrix for P2d pyrite/ marcasite .....	77
Table 11.	Trace element correlation matrix for P3 marcasite .....	81
Table 12.	SIMS analyses for pre-ore, ore-stage, late-ore stage pyrite and realgar....	86

## ACKNOWLEDGEMENTS

I would like to give my sincere thanks to my committee members Dr. Jean S. Cline, Dr. Margaret N. Rees, Dr. Elizabeth Jacobson, and Dr. Maralee Mayberry. I would also like to acknowledge the Ralph J. Roberts Center for Research in Economic Geology (CREG) at the Mackay School of Mines, National Science Foundation (NSF) Award EAR - 9614460 to Jean S. Cline, The Society of Economic Geologists Foundation Student Research Grant, the PROMISE program at UNLV, American Geological Institute Geoscience Scholarship Program, the University of Nevada, Las Vegas Planning Initiative Award (PIA), the University of Nevada, Las Vegas Department of Geoscience Bernada French Scholarships, and the UNLV Graduate Student Association Summer Research Grant for providing funds for this project.

I am especially grateful to Dick Nanna and his staff at Getchell Gold for their continuing support of this research and notable contributions toward understanding the Getchell underground ore body. Our current understanding of the Getchell mineral system is built upon a strong foundation of sound geologic observations and interpretations made by many Getchell geologists, without whose help and cooperation this research would not have been possible.

I would also like to thank and acknowledge Mike Spilde at the University of New Mexico, for his assistance with the electron microprobe and the cathodoluminescence study; Dr. Huifang Xu at the University of New Mexico, for conducting HRTEM analyses; Irene Farnham at the University of Nevada, Las Vegas

for generating the statistical data, plotting and help with interpretation; Dr. Margaret Rees, at UNLV for her valuable input and three years of valuable support through the PROMISE program; and Dr. Richard Omdorff at UNLV for his laser plotter expertise. Additional thanks to Dr. Wanda Taylor and Carole Hoeffle of the University of Nevada, Las Vegas; Richard Cahill of the University of Illinois, Champaign Urbana; and Dr. Karen Fryer of Ohio Wesleyan University, and Myrna Floyd my 7<sup>th</sup> grade Science teacher.

I am especially grateful to Michiko Shigehiro for her support, friendship and thoughtful discussions. My deepest honor to Dr. Jean S. Cline without whose help, patient editing, and cooperation this thesis would not have been possible.

I would also like to thank the folks at the Gorton's Fish Stickery, the potato farmers of America, the sour cream producers of the world, Boone's Farms, Wyders Pear Cider, The Peppermill, Luv It's Custard, La Taqueria, Sam Woo's Bar-B-Q and Steak Escape for providing me the nourishment that I have needed through the years.

I very much thank Tracy Cail, Cheryl Radeloff, Jamie Philips, Nick Wilson and Sarah Lundberg, for being such wonderful friends. I never could have done it with out you all.

Very special thanks to Jim. Without your friendship, love, support, and frozen custard, I don't know how I ever would have finished. Last, but never least, a special thanks to my parents for their love and patience through all of the years, and through all of the tons of dirt, clay, sticks and rocks that went through the washer and dryer; my first set of industrial rock tumblers.

## CHAPTER 1

### INTRODUCTION

Nevada currently ranks third in the world for gold production, behind South Africa and Australia (Driesner and Coyner, 2001). In 2000, Nevada produced 8.6 million troy ounces of gold worth about \$2.5 billion (Driesner and Coyner, 2001), a yield equivalent to almost 70% of the gold produced for the United States. This production was primarily from the sediment-hosted Carlin-type deposits of north-central Nevada, making Carlin-type gold deposits a significant source of world gold production.

The focus of this study is one of several Carlin-type gold systems located in north-central Nevada: the Getchell deposit, approximately 72 km northeast of Winnemucca, Nevada (Figure 1). Ore associated with Carlin-type gold deposits is characterized by decarbonatized and silicified sedimentary host rocks containing angstrom-sized gold particles (Bakken et al., 1989; Arehart et al., 1993a). The sub-microscopic gold commonly is included within arsenic-rich pyrite (Wells and Mullens, 1973; Hausen, 1981; Hausen and Park, 1985; Bakken et al., 1989, 1991; Arehart et al., 1993a; Sha, 1993; Fleming and Bakken, 1995; Cline et al., 1997; Cline and Hofstra, 2000). This disseminated gold also is associated with orpiment, realgar, stibnite (Bagby and Berger, 1985), galkhaite (Tretbar et al., 2000) and jasperoid (Cline et al., 1997). The highest concentrations of gold-ore mineralization at Getchell are within, and related to, the high-angle normal fault called the Getchell fault zone (Joralemon, 1951).

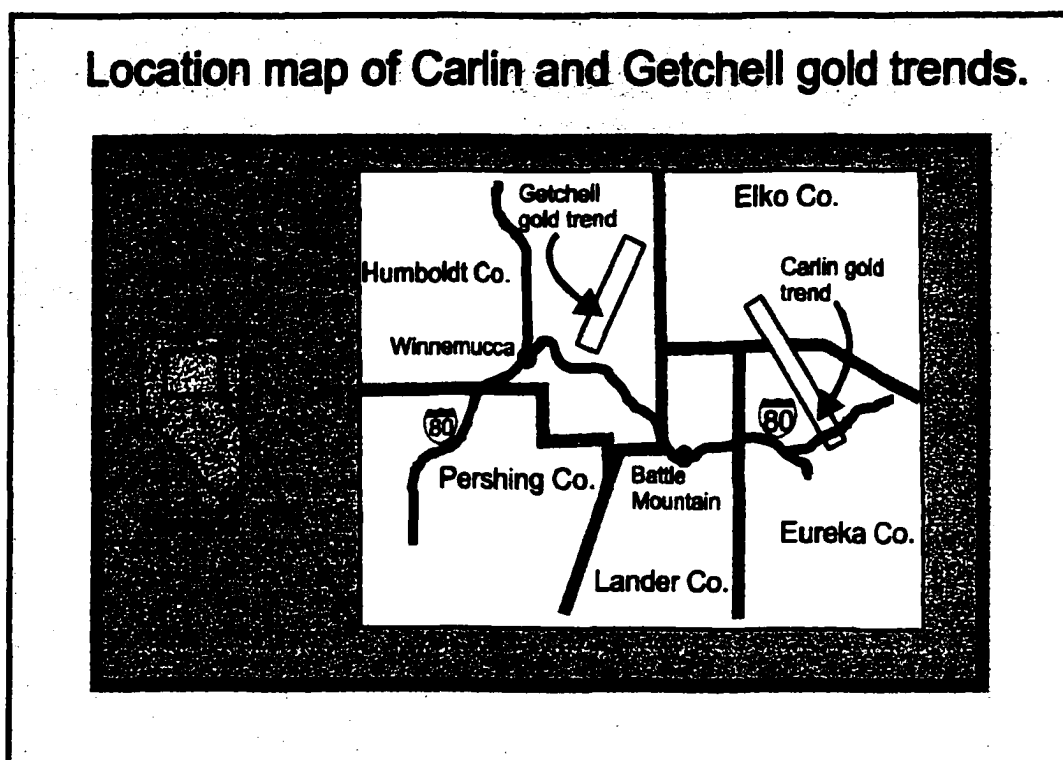


Figure 1. Location map showing the Getchell and Carlin gold trends (modified from Hauff et al., 1990).

Gold was first discovered at Getchell in 1934 within the Getchell fault zone, on the northeastern flank on the Osgood Mountains. Production of the arsenic-enriched, oxidized gold ore began 1936, and between the years of 1936 to 1999 over two million ounces of gold were produced from the Getchell property (Savio, 1999).

Despite the economic significance of the disseminated gold found at Getchell and other similar deposits, the genesis of sediment-hosted Carlin-type gold deposits is poorly understood. Origins of auriferous fluids, precipitation mechanisms, and the age and timing of mineralization all have been topics of heated debate. The scarcity of minerals unequivocally related to the gold mineralization and the very finely



crystalline nature of the ore-stage minerals have made the development of a detailed genetic model difficult.

Previous studies at Getchell indicate that gold is present in arsenic-rich rims on gold- and arsenic-free cores (Cline et al., 1997; Cline, 2001). In this study, the geochemistry of gold-bearing and gold-free pyrite and marcasite was examined closely to identify the trace-metal concentrations within Fe-sulfide minerals from the Getchell deposit. Petrographic analyses revealed textural relationships between gold-bearing and gold-free Fe-sulfide minerals. Electron microprobe analyses and secondary ion mass spectrometry were used to quantify major- and trace-metal compositions of the ore-bearing and gold-free Fe-sulfide minerals. Transmitted electron microscopy was used to determine how the gold is held within the Fe-sulfide mineral lattice.

Collectively, these results provide further information on the chemistry of the fluids that were responsible for precipitating and concentrating the gold-bearing pyrite and marcasite at the Getchell gold deposit.

## CHAPTER 2

### CARLIN-TYPE GOLD DEPOSITS

#### Characteristics of Carlin-Type Gold Deposits

Carlin-type gold deposits have been documented only in the western United States. However, Carlin-type deposits have been described in Peru (Alvarez and Noble, 1988), southern China (Ashley et al., 1991; Mao, 1991), Indonesia and southeast Asia (Sillitoe and Bonham, 1990; Garwin et al., 1995). Unfortunately, characteristic and descriptive data for most Carlin-type deposits outside of the western United States is not readily available.

The largest Carlin-type deposits in northern Nevada are located in three gold belts known as the Carlin trend, the Battle Mountain-Eureka trend, and the Getchell trend. The Carlin-type gold deposits within these trends are commonly aligned with and occur within a few hundred meters of large, high-angle normal faults (Rota, 1993; Arehart, 1996; Teal and Jackson, 1997) and are associated with decarbonatized and silicified host rocks (Bakken and Einaudi, 1986; Kuehn and Rose, 1995). The linear-trending mineralization may reflect the amount and orientation of mid-Tertiary extension and the regional-scale controls on fluid circulation and mineralization (Hausen and Kerr, 1968; Radtke, 1985; Rye, 1985; Maher et al., 1993). Fault zones provided the fracture system necessary for the transportation of hydrothermal solutions

through the host rock (Radtke and Dickenson, 1976; Adkins and Rota, 1984; Rota, 1993; Arehart, 1996).

Calcareous and fine-grained siliciclastic lithologies that favor Carlin-type gold mineralization are extensively silicified and decarbonatized, and they are gold-enriched through sulfidation (Hofstra et al., 1991; Stenger et al., 1997; Teal and Jackson, 1997). Carlin-type mineralization is characterized by significant decalcification, causing host-rock mass loss. Decalcification is then followed by the addition of 20 to 99 weight-percent silica (Radtke et al., 1980; Bakken, 1990; Ilchik, 1990; Sillitoe and Bonham, 1990; Kuehn and Rose, 1995; Hofstra, 1994; Arehart, 1996; Teal and Jackson, 1997) in many deposits. Rocks peripheral to the decarbonatized and silicified gold-bearing zones in Carlin-type deposits typically remain calcareous and contain gold concentrations several orders of magnitude below concentrations found in the adjacent mineralized zones (Radtke et al., 1980; Christensen, 1993; Arehart, 1996).

Carlin-type gold occurs as angstrom-sized particles disseminated within sedimentary host rocks (Hausen and Kerr, 1968; Radtke, 1985; Bakken et al., 1989; Bakken, 1990; Arehart et al., 1993a; Arehart, 1996). This angstrom-sized gold is present commonly within arsenic-rich Fe-sulfide minerals that typically form rims on arsenic- and gold-poor pyrite cores (Wells and Mullens, 1973; Radtke, 1985; Bakken, 1990; Arehart et al., 1993a; Fleet and Mumin, 1997). Gold-bearing rims on pyrite typically contain 1 to 10 percent As and an accompanying accessory suite of trace metals that are 10 to over 1000 times enriched above host-rock background levels (Wells and Mullens, 1973; Arehart et al., 1993b). Trace metals identified as associated with disseminated gold mineralization were incorporated into the sulfide crystals during ore deposition,

and they include Au (Hausen, 1981; Hausen and Park, 1985; Radtke, 1985; Bakken et al., 1989; Arehart et al., 1993a), As (Wells and Mullens, 1973; Radtke, 1985; Landis and Hofstra, 1991; Arehart et al., 1993a), Hg, Sb, and Tl (Hausen and Kerr, 1968; Radtke, 1985; Irkamuddin et al., 1996; Fleet and Mumin, 1997) and Cu (Fleet et al., 1989).

## CHAPTER 3

### THE GETCHELL GOLD DEPOSIT

#### Location and General Regional Geology

The Getchell gold deposit is located in the Basin and Range Province of northern Nevada, approximately 72 km northeast of Winnemucca, Nevada. The Getchell mine lies along the northeastern flank of the Osgood Mountains in the northern end of the Getchell trend. Getchell consists of 3 open pits and an underground mine below these pits. The Getchell property also contains the Turquoise Ridge gold deposit that lies a few hundred meters east of the Getchell gold mine.

The major structural features in the Getchell mine region include the Roberts Mountain thrust (Merriam and Anderson, 1942; Joralemon, 1951; Roberts et al., 1958; Berger and Taylor, 1980), which is associated with latest Devonian or early Mississippian contraction (Roberts et al., 1958), and tectonic features related to mid-Tertiary extension (Joralemon, 1951; Hofstra et al., 1999). During early Paleozoic time, the area lay along the western passive margin of Laurentia (Stewart and Suczek, 1977; Speed, 1979). The Antler orogenic event of latest Devonian or early Mississippian age emplaced Paleozoic, siliceous, deep-marine sediments and marine volcanic rocks eastward over Cambrian and Ordovician shallow-water, carbonate sedimentary units (Roberts et al., 1958). This tectonic event involved the collision and accretion of a

volcanic arc system onto the western margin of the North American plate that generated a series of imbricated thrust faults and folded the underlying Paleozoic sediments into a series of isoclinal and drag folds (Stewart, 1978; Coney, 1978). This orogenic activity formed the regionally extensive Roberts Mountain thrust system (Joralemon, 1951; Roberts et al., 1958).

The Antler orogeny was followed by the late Permian to early Triassic Sonoma orogeny (Miller et al., 1984; Saleeby and Busby-Spera, 1992). The tectonism of the Sonoma orogeny involved the subduction, collision, and accretion of the Sonomia microplate onto the deformed western margin of North America. The period of time between the late Permian to early Triassic involved periods of complex sedimentation, deformation, and igneous activity within the continental foreland (Speed, 1979; Saleeby and Busby-Spera, 1992).

The compressional regimes of the mid-late Jurassic to mid-Cretaceous Sevier orogeny involved coincident magmatism and eastward contraction of terranes that were accreted during the earlier Antler and Sonoma orogenies (Miller et al., 1992; Dickinson, 1992). Both the Sonoma and Sevier tectonic events led to over 100 km of crustal shortening in portions of Nevada and Utah and resulted in scattered plutonism across the northern Great Basin (Miller et al., 1988). During the late Cretaceous (~90 Ma), large granodiorite plutons and andesite dikes intruded the accreted terranes causing regional metamorphism of the surrounding carbonate host rock and formed tactite-tungsten, and wollastonite-hornfels-marble facies ore-bodies (Getchell Gold Corporation, 1997).

Approximately 42 Ma, major mid-Tertiary extension was initiated (Gans et al., 1989). This extensional event produced highly complex systems of Basin and Range

structures that extend for more than 1500 km along the western Cordillera of North America (Stewart, 1978; Seedorff, 1991; Fricke et al., 1992).

### Getchell Stratigraphy

The sedimentary units that are exposed in the Osgood Mountains and within the Getchell mine range in age from early Cambrian to early Silurian. These units occur in two distinct fault-bounded terranes (Figure 2): the Osgood and Getchell terranes (Madden-McGuire and Marsh, 1991). These terranes are lithologically and structurally distinct and represent two different stratigraphic successions (Madden-McGuire and Marsh, 1991).

### Osgood Terrane

The lower Cambrian to lower Ordovician Osgood terrane consists of the Osgood Mountain Quartzite, the intensely deformed and regionally metamorphosed sedimentary rocks of the Preble Formation, and some of the rocks currently mapped as the Comus Formation (Madden-McGuire and Marsh, 1991).

The Osgood Mountain Quartzite is composed predominantly of well-sorted, quartz-rich metamorphosed sandstone, but also contains very poorly sorted feldspathic-rich successions (Ferguson et al., 1951; Hotz and Willden, 1964; Madden-McGuire and Marsh, 1991). The uppermost part of this unit is characterized by interbedded shale, which marks the gradational transition between Osgood Mountain Quartzite and the overlying Preble Formation (Hotz and Willden, 1964; Erickson and Marsh, 1974). The Preble Formation, first named by Ferguson et al. (1951), is host to gold ore in the

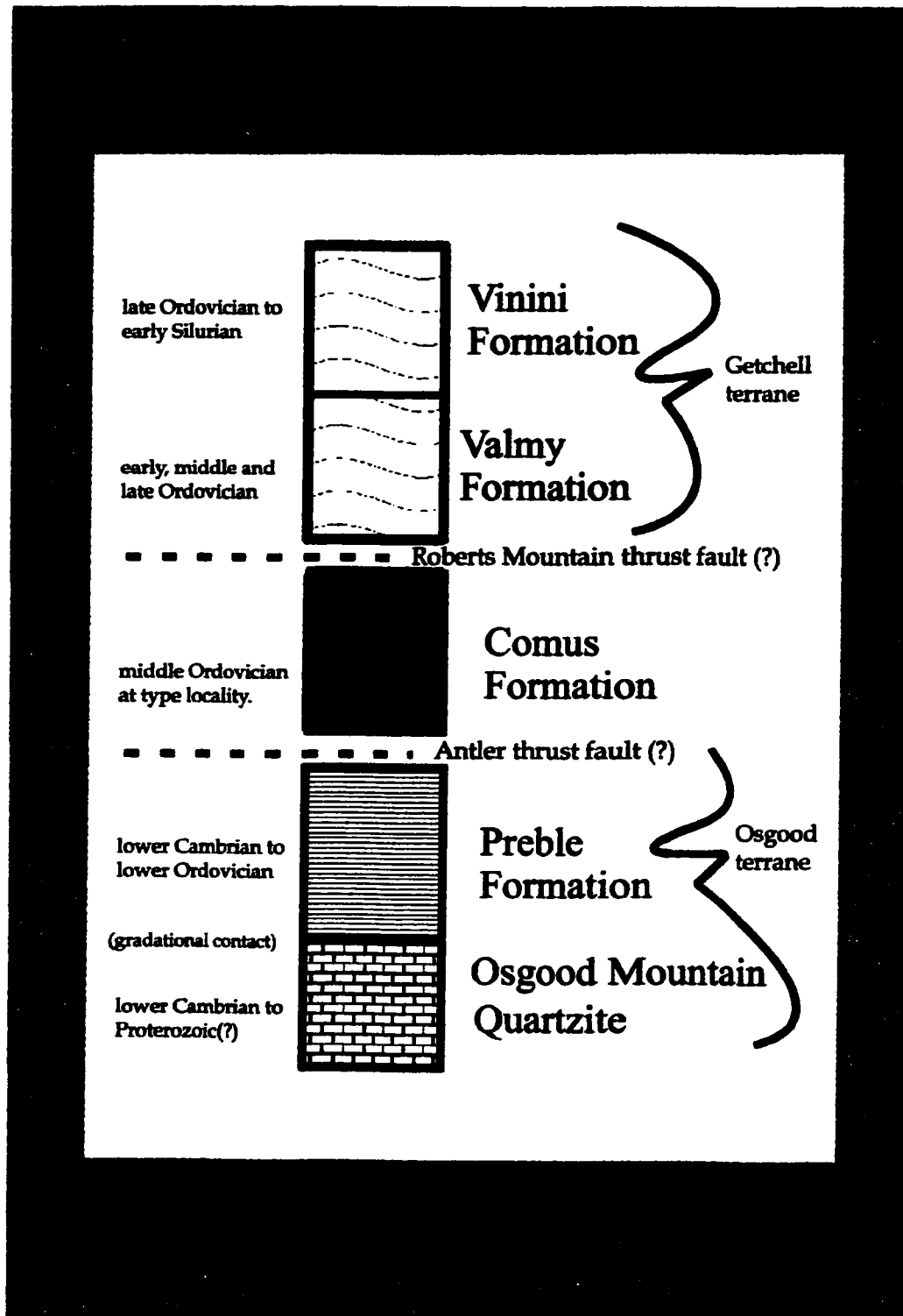


Figure 2. Tectono-stratigraphy of Getchell mine area, adapted from Silberman et al. (1974), Berger and Taylor (1980), Madden-McGuire and Marsh (1991), and Groff et al. (1997).



Getchell underground deposit. Locally, it consists of metamorphosed and intensely deformed shale interbedded with limestone and sandstone (Rees and Rowell, 1980; McCollum and McCollum, 1990; Madden-McGuire and Marsh, 1991).

### **Comus Formation**

The Comus Formation, which also was named by Ferguson et al. (1951), is a fault-bounded lithologic package that structurally overlies the upper portion of the Osgood terrane, and is structurally situated below the Getchell terrane (Madden-McGuire and Marsh, 1991). At its type locality, the Comus is middle Ordovician in age (Erickson and Marsh, 1974; Madden-McGuire and Marsh, 1991), but the age may range into the late Ordovician (Berger and Taylor, 1980).

Although the Comus Formation lithologically resembles the Preble Formation, the Comus Formation contains more limestone, is less deformed, and is not as intensely regionally metamorphosed as the Preble Formation (Madden-McGuire and Marsh, 1991).

### **Getchell Terrane**

The Getchell terrane (Madden-McGuire and Marsh, 1991) structurally overlies the Comus Formation and is composed of rocks assigned to the Valmy (Hotz and Willden, 1964; Madden-McGuire and Marsh, 1991) and Vinini (Merriam and Anderson, 1942; Erickson and Marsh, 1974; Madden-McGuire and Marsh, 1991) formations. The Valmy Formation consists of interbedded chert, quartzite, argillite, slate, and basalt with poorly preserved pillow structures and volcanic breccia (Madden-McGuire and Marsh, 1991). The age of the unit is constrained to early to late Ordovician (Hotz and Willden, 1964; Madden-McGuire and Marsh, 1991). Further studies conducted by Madden-

McGuire and Marsh (1991) determined that the Valmy is possibly the remnant of a much more extensive thrust sheet.

The Vinini Formation, originally defined by Merriam and Anderson (1942), was determined to be late Ordovician to early Silurian in age by Finney et al. (1989). The Vinini Formation is composed of thinly bedded chert, vanadium-enriched shale, and fine-grained quartzite (Hotz and Willden, 1964; Erickson and Marsh, 1974).

The rocks mapped as the Valmy and Vinini are not as deformed nor as metamorphosed as the rocks in the Osgood terrane. Additionally, the folds in the Valmy and Vinini formations are more open and plunge and trend to the southeast, in contrast to the north-plunging, tight folds in the Preble and Comus (Madden-McGuire and Marsh, 1991). The Valmy and Vinini crop out at the Getchell mine but are not generally mineralized.

#### Granodiorite Intrusion

The Osgood Mountains of eastern Humboldt County, Nevada, are composed in part of a 92 Ma granodiorite stock and associated andesite porphyry dikes (Silberman et al., 1974; Groff et al., 1997) that intruded the intensely folded and thrust-faulted lower Paleozoic sedimentary units (Silberman et al., 1974). The emplacement of the dikes was controlled in part by the northerly striking Getchell fault zone (Berger and Taylor, 1980). Many of the Osgood Mountain andesite dikes were deformed and hydrothermally altered by subsequent faulting and hydrothermal fluid movement along the Getchell fault.

The intrusion of the stock and dikes into the lower Paleozoic sedimentary units produced hornfels, marble, and tungsten-molybdenum skarn deposits (Getchell Gold Corporation, 1997). The shaley limestone, skarn, marble, and other meta-sedimentary calc-silicate rocks form the protoliths upon which the later gold mineralization was superimposed (Joralemon, 1951; Hotz and Willden, 1964).

#### **Structural Controls of the Getchell Au deposit**

Regionally, the Roberts Mountain thrust emplaced rocks of the Getchell terrane over Osgood terrane. The thrust itself was most likely not a single thrust sheet, but consisted of numerous imbricate slices that have, in some areas, shuffled isolated slabs of lower plate rocks between upper plate thrust slices (Adkins and Rota, 1984).

The Getchell fault zone is a north-northwest striking, northeast dipping complex of anastomosing faults with strike-slip and dip-slip motion that extend for more than 25 km (Joralemon, 1951; Silberman et al., 1974). This major fault zone crosscuts the Preble and Comus sedimentary assemblages and the Roberts Mountains thrust fault (Joralemon, 1951; Berger and Taylor, 1980). The Osgood Mountain granodiorite is also displaced by the fault, showing that the latest movement on the fault was less than 92 Ma.

#### **Carlin-Type Gold Mineralization at Getchell**

Gold mineralization at Getchell is restricted to calcareous siltstone, silty carbonate, calcareous shale, and limestone units within the Preble Formation (Joralemon, 1951; Hotz and Willden, 1964; and Berentsen et al., 1996).

The largest gold-ore bodies at Getchell are linear zones aligned within major northwest faults related to the trend of Getchell fault zone (Joralemon, 1951; Berger and Taylor, 1980; Getchell Gold Corporation, 1997). The disseminated gold is especially concentrated within the Getchell fault zone where the fault is crosscut by other fault zones (Berentsen et al., 1996; Getchell Gold Corporation, 1997).

Unoxidized ore at the Getchell gold mine is generally characterized by pyrite, marcasite, and jasperoid quartz mineralization, and low-temperature arsenic minerals (Joralemon, 1951; Groff et al., 1997; Cline et al., 1997). Two episodes of sulfide mineralization are readily visible as early arsenic- and gold-free pyrite and later arsenic- and gold-rich, Fe-sulfide minerals (Getchell Gold Corporation, 1997; Cline and Hofstra, 2000). Gold is disseminated within arsenic- and trace element-rich Fe-sulfide rims and crystals (Joralemon, 1951; Cline et al., 1997; Cline and Hofstra, 2000). The Fe-sulfide content of the mineralized sedimentary rock units of the Getchell mine typically range from 1 to 6% (Getchell Gold Corporation, 1997). The average ore grade mined from the Getchell underground is 0.335 oz/ton (Getchell Gold Corporation, 1997).

Historically, much of the uncertainty about the age of Carlin-type gold mineralization was related to the difficulty in identifying dateable minerals that are clearly of hydrothermal origin and temporally associated with gold. According to Joralemon (1951) and Cline and Hofstra (2000), the bulk of the economic gold at Getchell is localized in the Getchell fault zone, which crosscuts the 92 Ma granodiorite stock (Silberman et al., 1974). Additionally, altered and mineralized dikes are located within the ore zones at Getchell, suggesting that the gold deposit at Getchell is younger than

the 98, 95, and 92 Ma altered and mineralized basalt dikes dated by Groff et al. (1997).

More recent work and review of ages for Carlin-type gold mineralization suggests that most gold was deposited between 42 and 30 Ma (Hofstra et al., 1999). Galkhaite from Getchell was recently dated using Rb-Sr at  $39.0 \pm 2.1$  Ma (Tretbar et al., 2000). The Tretbar et al. (2000) study demonstrates that galkhaite is a gold-ore stage mineral, and that gold and minerals associated with the gold precipitated at the Getchell deposit between 37-41 Ma.

## CHAPTER 4

### SAMPLING AND ANALYTICAL METHODS

The purpose of this study is to identify the petrographic characteristics and trace element compositions of the Fe-sulfide minerals from the Getchell underground mine. Samples were collected from the northwest, main, and south ore zones of the Getchell underground mine (Figure 3). A total of ~1400 underground core samples representing 70 drill-hole transects were selected from these three regions. Samples were selected from cores exhumed from the operating underground mine, and from rocks held in storage at the mining facility (Appendix 1). The samples are from mine depths ranging from 5100' asl (feet above sea level) to 4655' asl. Core length, lithologic competence, and composition of the core determined the number of samples collected within each transect.

Samples were collected over a large area of the mine to compare mineral assemblages in ore and non-ore specimens and to observe mineralogical variations. In particular, samples were selected for analyses using the following criteria:

1. visible pyrite in samples that contained high Au ( $\geq 0.2$  oz/ton).
2. high assays ( $\geq 0.2$  oz/ton) and sooty pyrite.
3. crosscutting mineral relationships in hand specimen.
4. assays indicated low to nil Au ( $\leq 0.1$  oz/ton) and visible pyrite present.
5. assays indicated low to nil Au ( $\leq 0.1$  oz/ton) and no visible pyrite present.
6. alteration such as decarbonatization or silicification present, associated with high-grade assay values.
7. carbonaceous and calcite-rich samples with low to nil Au and little to no evidence of silicification.

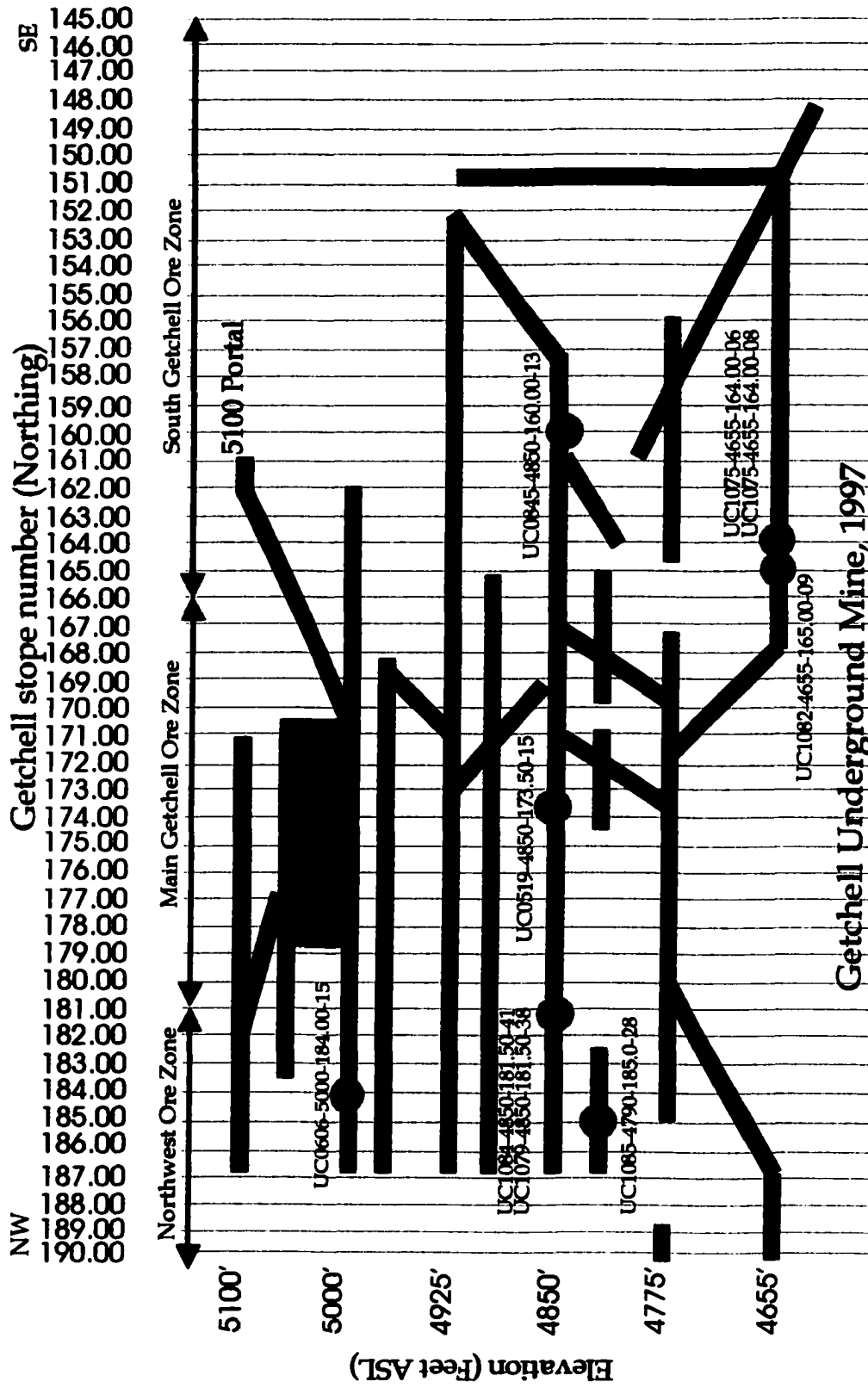


Figure 3. Cross section showing underground mine levels of the Getchell underground mine in 1997. Sample locations from the northwest, main, and south ore zones are shown by (●).

Based on these criteria, 32 samples from 9 transects through ore-grade zones were selected for thin section preparation. Fire-assay analyses conducted by the Getchell laboratory determined that the gold content in the selected samples varied from 0.0 oz/ton to 1.4 oz/ton.

## ANALYTICAL METHODS

### Petrographic Analyses

To construct the mineral paragenesis and discern morphologically distinct pyrite populations, 32 polished thin sections were examined using transmitted and reflected light microscopy (Appendix 2). Petrography was used to identify mineral textures and crosscutting relationships between the minerals.

### Electron Microprobe Analysis (EMP)

To determine the trace element composition of the pyrite populations, twenty-one polished thin sections were carbon coated and analyzed with a JEOL JXA733 microprobe at the University of New Mexico, Department of Earth and Planetary Science (Appendix 2). Reference profiles were collected on standards and correction factors calculated by analyzing secondary standards close in composition to the unknown material, where possible.

Correction factors were calculated for major elements Fe and S, and trace elements Pb, Hg, and Zn on natural standards of Taylor pyrite, galena, cinnabar, and sphalerite, respectively. Co, Ni, Cu, Au, Ag, and Mo were measured on pure element



standards only. Acceleration voltages used on the pure element standards were performed at 25kV with ~30 nA beam current. Higher acceleration voltage and longer residence times were necessary to obtain acceptable trace element totals.

The elements As, Tl, and Sb were measured on synthetic standards of GaAs, TlCl, and Sb<sub>2</sub>Te<sub>3</sub>, respectively. The acceleration voltages used to determine Tl and Sb were 25kV with ~30 nA beam current. Due to the high absorption by As and the volatilization of S, lower residence times and acceleration voltages (20kV at ~30 nA) on the synthetic standard GaAs were necessary for S and As analyses. Detection limits of one standard deviation for all elements analyzed are given in Appendix 3. The lowest total obtained and used in this study was 95.00 wt. %.

#### Secondary Ion Mass Spectrometry (SIMS)

Ion probe microanalysis was used to quantify submicroscopic gold and arsenic in pyrite, marcasite, and realgar in five samples (Appendix 2). A total number of 41 points approximately 20µm in diameter were analyzed using a Cameca IMS-3f ion microprobe at AMTEL in Ontario, Canada.

Experimental parameters and samples analyzed by ion microprobe analysis are shown in Table 1. The standard for gold was natural pyrite implanted with <sup>197</sup>Au, and an arsenian pyrite standard was used for As. The primary beam diameter and analysis crater for the quantitative analysis is approximately 20 µm. Crystal sizes of the pyrites analyzed by SIMS were typically much smaller than 100 µm in diameter. Many of the pyrite crystals were smaller than 20 µm, which likely led to dilution of As and Au in the pyrite by minerals adjacent to pyrite crystals chosen for SIMS analysis.

**Table 1. Experimental Parameters for Ion Microprobe Analysis**

Samples Analyzed		
UC1075-4655-164.00-06-86	UC0606-5000-184.00-15-157	UC0519-4850-173.50-15-62
UC1079-4850-181.50-38-197	UC1084-4850-181.50-41-197	
General Parameters		
Instrument	Cameca IMS-3f ion microprobe	
Standardization	External (ion implantation) Au implanted in pyrite, and As-rich pyrite.	
Ion Microprobe Operating Conditions		
Beam source	Cs+	
Secondary-ion polarity	negative	
Primary beam current	20 - 25 nA	
Impact energy (primary ions)	14.5 KV	
Sample charge compensation	none	
Primary beam diameter	20 μm	
Crater (analysis area) diameter	20 μm	
Mass interference	<sup>197</sup> CsS <sub>2</sub> , <sup>197</sup> FeAs <sub>2</sub> eliminated by -180V energy offset	
Minimum detection limits	150 ppb	
Depth of analyzed profile	0.8 - 1.2 μm	

Further details of the quantitative analytical procedures and standardization are given by Chrysoulis (1989, 1990).

The depth profiling capability of the ion microprobe permits the identification of subsurface, submicrometer-scale mineral inclusions. Depth profiling, or “sputtering”, gradually removes material from the sample surface and creates a crater. Au inclusions as small as about 100 angstroms (0.01  $\mu\text{m}$ ) can be detected by in-depth profiling, allowing identification of colloidal gold that is dispersed in the Fe-sulfide minerals (Chrysoulis, 1989, 1990).

## HRTEM

Preliminary high-resolution transmission electron microscopy (HRTEM) was conducted at the University of New Mexico Department of Earth and Planetary Science by Dr. Huifang Xu. HRTEM was conducted to determine the crystal chemistry of the Au- and As- bearing ore-stage Fe-sulfide minerals.

For HRTEM investigation, three petrographic thin sections were prepared with doubly polished surfaces (Appendix 2). Suitable pyrite minerals were then selected with the petrographic microscope and were mounted on Cu grids. The specimens chosen for HRTEM analyses were thinned with an Ar ion mill and then coated with a thin carbon film. The high resolution TEM study was performed with the SEM2010 HRTEM, operated at 200kV. Energy dispersive spectra (EDS) were collected with LINK ISIS system software for the HRTEM (Xu and Veblen, 1995).

## **Cathodoluminescence**

**Cathodoluminescence (CL) analysis was conducted at the University of New Mexico Department of Earth and Planetary Science. A JEOL 5800LV SEM equipped with secondary and back-scattered electron and CL imaging detectors was used to distinguish regions containing visibly different populations of quartz and calcite within ore-stage and late-ore stage assemblages.**

**Although reflected light, transmitted light, and EMP can allow optical and chemical identification of minerals, these analyses are incapable of imaging the internal crystal structures of minerals such as quartz and calcite. In minerals that luminesce, imaging readily resolves growth zones, because the CL detector provides good spectral response across the visible range into the near UV and IF wavelengths (Kearsley and Wright, 1988). By linking characteristic spectral intensities of CL emission to the trace element content of individual growth zones, cathodoluminescence can be used to identify discrete events during mineralization (Kearsley and Wright, 1988).**

## **Statistical Analysis**

**Statistical analyses were conducted at the Harry Reid Center, University of Nevada, Las Vegas. STATISTICA for Windows, Excel, and FOX PRO software were used to statistically distinguish the pyrite populations. Data of major elements Fe and S, and trace elements Pb, Co, Hg, Ag, Tl, Ni, As, Cu, Sb, Zn, and Mo obtained through EMP analyses, were used to generate correlation matrices. The trace element data were then analyzed further using K-means clustering (STATISTICA for Windows, 1995, V. III: Statistics, 2<sup>nd</sup> Edition, StatSoft Incorporation., p. 3197 – 3234).**

## CHAPTER 5

### MINERAL PARAGENESIS

Petrographic, electron microprobe, SIMS, and TEM analyses provided a basis for developing the paragenetic study of the Fe-sulfide minerals at Getchell. The combination of analyses provided data necessary to distinguish different Fe-sulfide mineral populations, identify Fe-sulfide populations associated with gold, and quantify trace elements associated with the gold mineralization event. Gold assays, EMP and SIMS analyses were used to distinguish between gold-poor and gold-bearing Fe-sulfide minerals.

Crosscutting relationships, open-space filling textures, crystal-growth patterns, overgrowth textures, and other textural relationships were used to identify temporal relationships between minerals. Analyses and textural relationships led to identification of pre-ore stage (Stage 1), ore-stage (Stage 2), and late-ore stage (Stage 3) assemblages. The following abbreviations are used in figures throughout this chapter: UC sample identification numbers for photomicrographs (see Appendix 2), RL = reflected light, TL = transmitted light, PPL = plane-polarized light, CPL = crossed polarized light, SEI = scanning electron image, and BEI = backscattered electron image.

### Stage 1 – Pre-Ore Stage Mineral Assemblage

The pre-ore stage mineral assemblage present in the Getchell underground mine is chiefly characterized by two types of calcite (C1a, C1b), two types of pyrite (P1a, P1b), vein quartz (Q1), barite (B1), and apatite. These minerals formed at different times and occur in a distinctive paragenetic sequence (Table 2). Gold is not present in this assemblage.

#### Stage 1 Pre-Ore Mineral Paragenesis

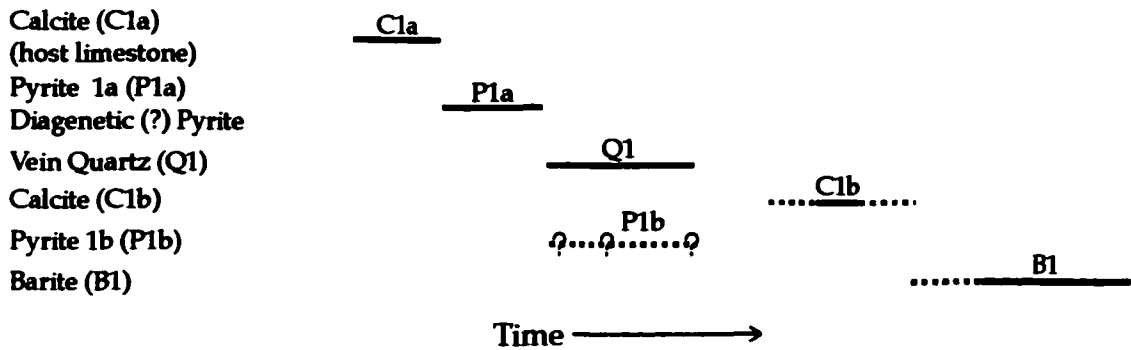
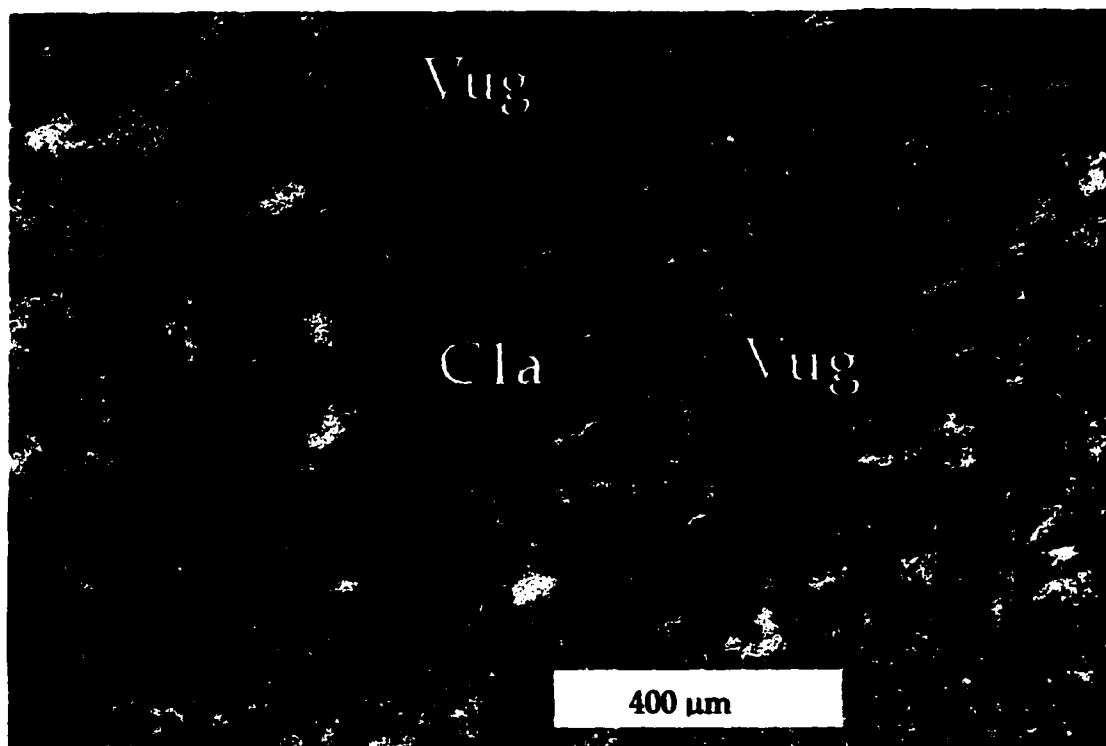


Table 2. Paragenetic sequence observed for pre-ore minerals.

#### Calcite (C1a)

C1a calcite occurs in meta-sedimentary rocks that were not silicified, and appears to be original limestone groundmass. This limestone protolith often exhibits relict sedimentary bedding. The C1a limestone groundmass (Figure 4) is very finely crystalline, is typically peppered with unidentifiable opaque minerals, and often contains vugs that may have contained other early minerals or from which calcite may have been dissolved.



**Figure 4.** TL, CPL photomicrograph showing C1a calcite with vugs in thin section UC1079-4850-181.50-38-85.

#### Pre-ore Pyrite (P1a and P1b)

Pre-ore stage P1a and P1b pyrite are generally coarse and euhedral to subhedral in shape. Both types exhibit typical cubic forms, high polish, high relief, and have a bright yellowish-white color (Figures 5 and 6). P1a pre-ore pyrite (Table 2) generally occurs as euhedral to subhedral crystals that are typically located along relict bedding planes within meta-sedimentary host rock that may be calcite-rich to very slightly silicified. P1a pyrite commonly exhibits evidence of chemical reaction and partial dissolution and replacement, forming atoll structures and vugs in the limestone groundmass. P1b pyrite occurs as euhedral to subhedral crystals enclosed in altered

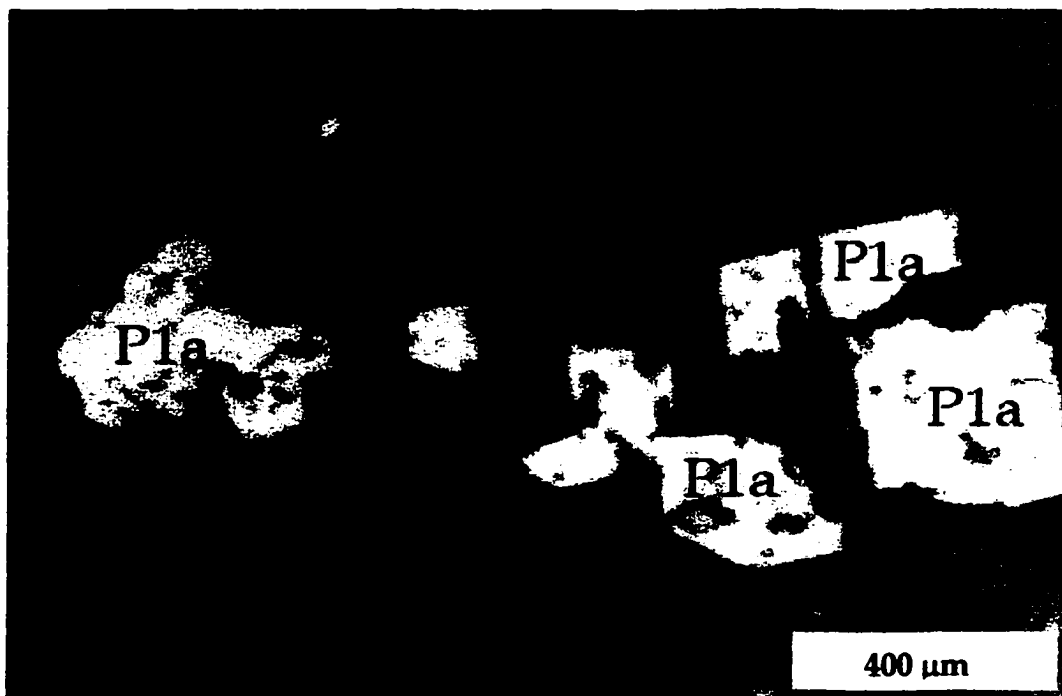


Figure 5. RL photomicrograph of thin section UC1079-4850-181.50-38-421 showing euhedral P1a pyrite within C1a calcite groundmass.

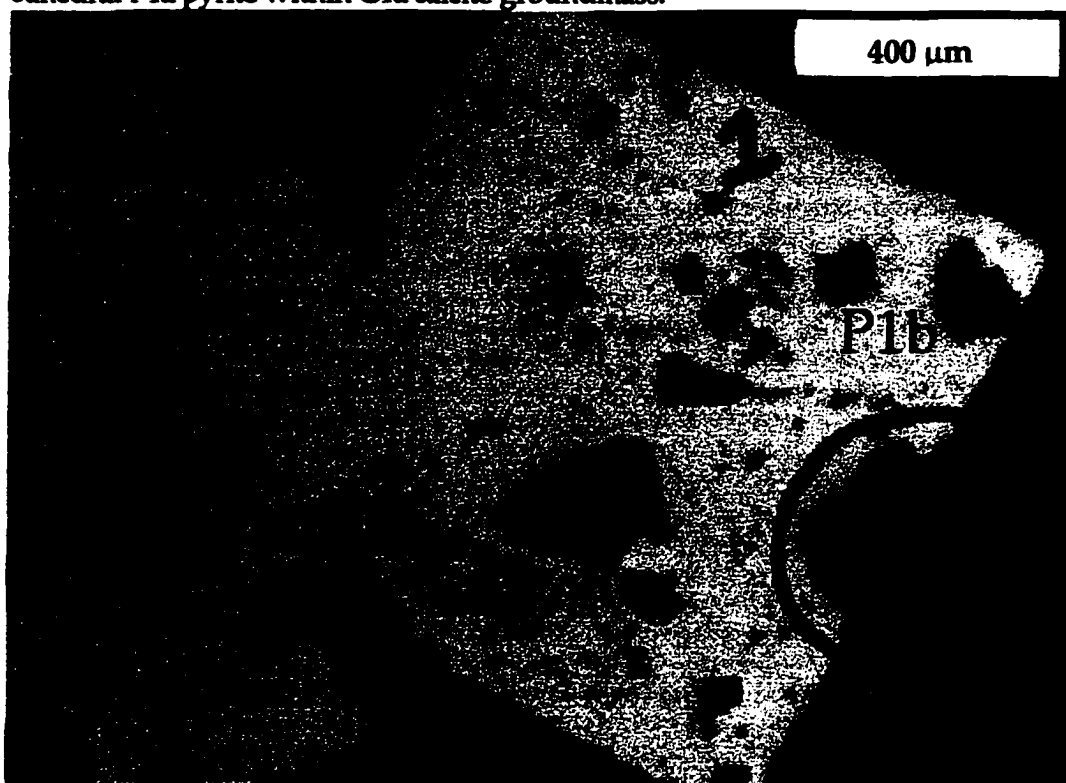


Figure 6. RL photomicrograph of thin section UC1079-4850-181.50-38-441 showing P1b euhedral pyrite within altered dike groundmass.



dacite porphyry groundmass; the crystal surfaces generally appear fresh and uncorroded.

#### Vein Quartz (Q1)

Q1 vein quartz is coarsely crystalline, commonly exhibits undulatory extinction, and is generally free of opaque mineral inclusions (Figure 7). These quartz crystals are anhedral and often contain trails of very small, abundant, secondary fluid inclusions following fractures. These fluid inclusion trails give the quartz crystals a “wispy” appearance. Phases observed within the fluid inclusions include vapor, liquid, +/- solid inclusions. These fluid inclusions are approximately 2.5  $\mu\text{m}$  in diameter.

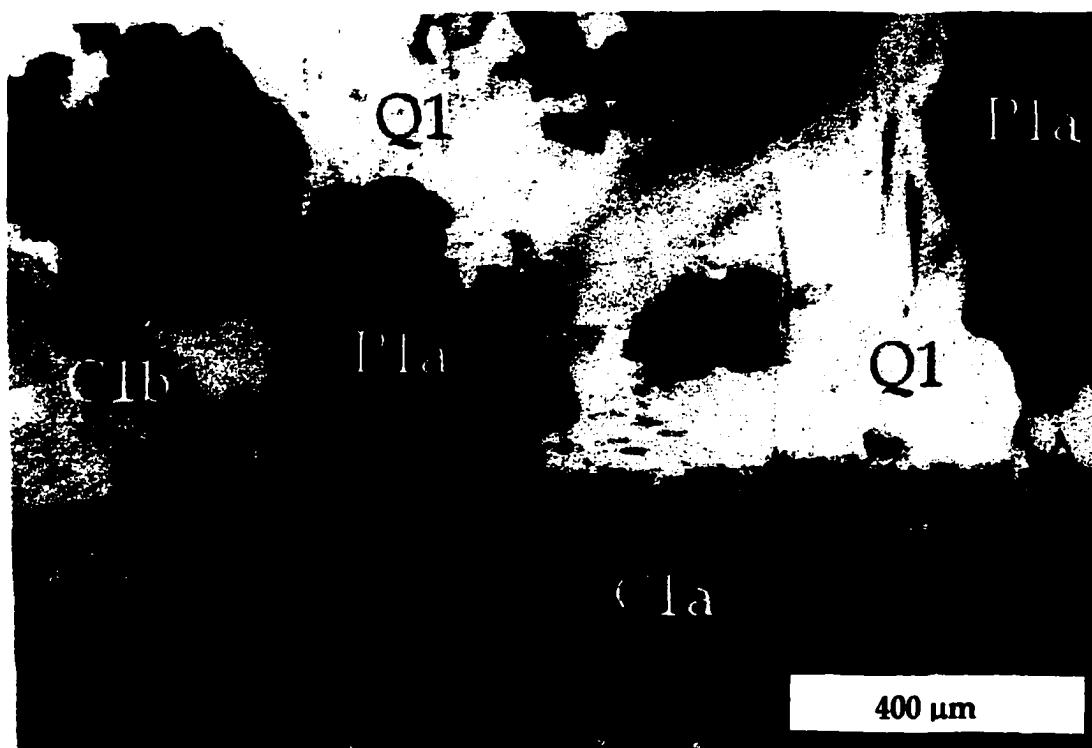


Figure 7. TL, CPL photomicrograph of thin section UC1079-4850-181.50-38-85 showing Cla groundmass limestone, Pla pyrite, C1b clean calcite, and Q1 quartz.

Q1 quartz veins may have formed in association with the granodiorite intrusion and/or the related dikes (Cline and Hofstra, 2000). The Q1 vein quartz typically contains ovoid apatite inclusions (Figure 8). Q1 vein quartz crosscuts and fills vugs in the C1a limestone. Q1 quartz also often encompasses P1a pyrite.

### Apatite

Commonly observed as small inclusions in Q1 vein quartz, apatite is present in the form of small ovoid crystals,  $\leq 2.5 \mu\text{m}$  in diameter, and occasionally  $50 \mu\text{m}$  in length (Figure 8). Light green in color and “potato-shaped”, this mineral is not uniformly dispersed within the Q1 quartz (Figure 8).

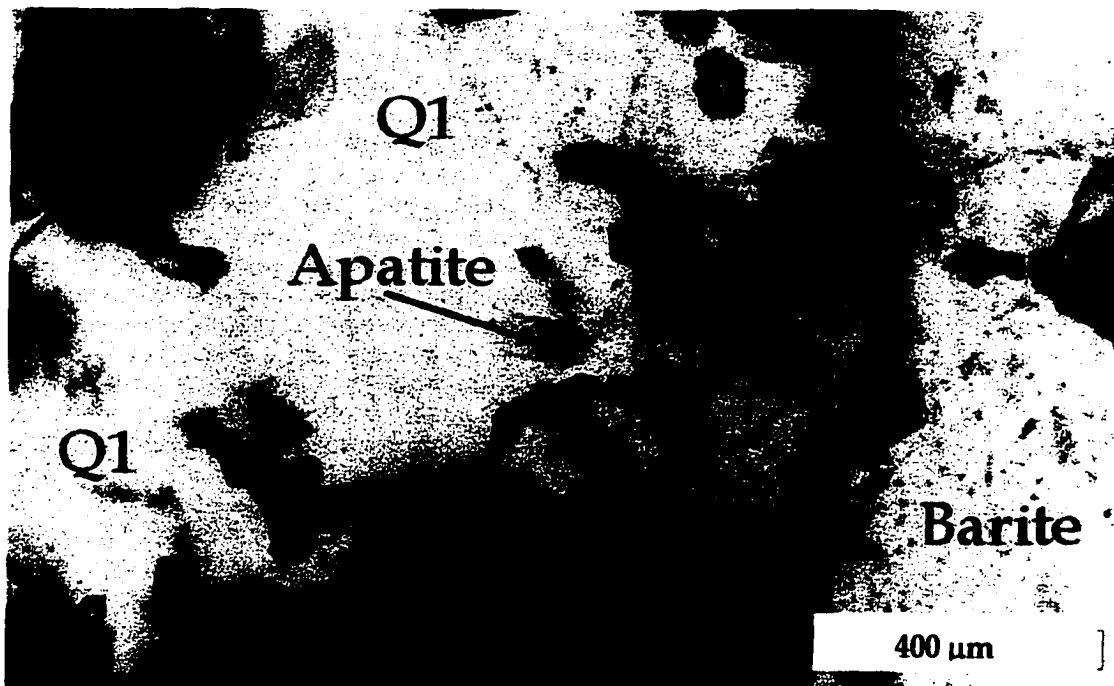


Figure 8. TL, PPL photomicrograph of thin section UC1079-4850-181.50-38-85 showing apatite mineral inclusions within Q1 vein quartz.

### Calcite (C1b)

C1b calcite is locally present and is a rare form of secondary calcite that is coarsely crystalline, “clean”, and free of opaque mineral inclusions. This calcite contains two-phase (liquid plus vapor), rectangular, secondary fluid inclusions that are approximately 5  $\mu\text{m}$  or less in size (Figure 9). The calcite is locally observed near or adjacent to corroded crystal boundaries of P1a pyrite, or filling vugs in C1a.

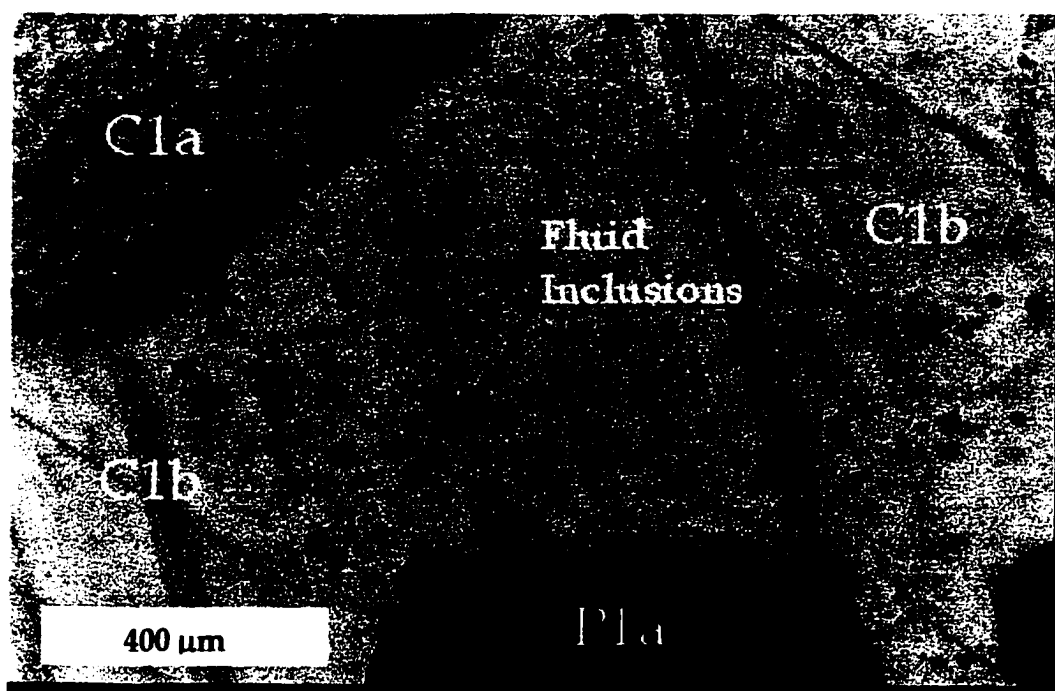


Figure 9. TL, PPL photomicrograph of thin section UC1079-4850-181.50-38-85, showing C1b calcite, adjacent to a mass of P1a pyrite, and a mass of C1a calcite. Small, rectangular fluid inclusions are visible within the C1b calcite crystal.

### Barite (B1)

Barite crosscuts C1a limestone matrix and encompasses P1a pyrite crystals. The barite contains many two-phase, liquid plus vapor fluid inclusions, generally  $< 2 \mu\text{m}$  in size (Figure 10). The fluid inclusions are unevenly distributed through the crystal and are not observed in growth zones. The barite crystal boundaries commonly exhibit vermicular intergrowths with C1b calcite. Additionally, barite commonly contains apatite inclusions.

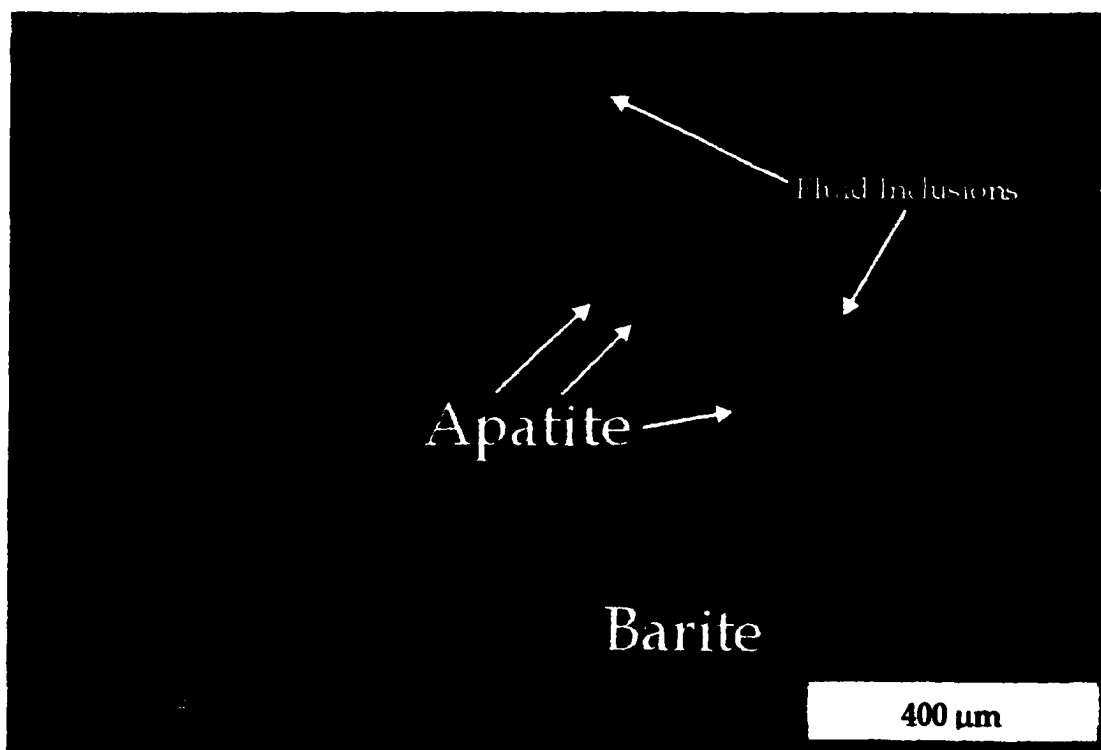


Figure 10. TL, CPL photomicrograph of thin section UC1079-4850-181.50-38-85 showing apatite inclusions within barite. The largest solid apatite inclusion measures almost  $175 \mu\text{m}$  in diameter.

## Discussion of Pre-Ore Paragenesis

Pre-ore mineralization contains minerals that formed in igneous and sedimentary environments and encompasses more than one single geologic event. The euhedral to subhedral shape of the P1a pyrite, and location along relict beds within calcite-rich to very slightly silicified meta-sedimentary host rocks suggests a diagenetic origin for the pyrite.

Q1 quartz veins were precipitated within fractures in the C1a limestone host rocks after formation of P1a diagenetic pyrite. Precipitation of Q1 vein quartz was probably related to fluids produced by the intrusion of the granodiorite (Cline et al., 1997). The processes that initiated the precipitation of Q1 could also have triggered the partial dissolution of the limestone groundmass and P1a, thus, liberating the P1a pyrite and allowing it to be locally encapsulated by the Q1 quartz. P1b pyrite is not encapsulated by Q1 quartz and is related to the later andesite dikes, which crosscut the granodiorite.

Following the deposition of the Q1 quartz veins, small amounts of C1b and barite were locally precipitated in the open spaces and within the corroded P1a pyrite crystals. Owing to the irregular distribution and rounded form of some of the apatite crystals within barite and Q1 quartz, they likely are inherited detrital crystals (Cline and Hofstra, 2000).

## Stage 2 – Ore-Stage Mineral Assemblage

Ore-stage mineralization is characterized by the alteration of the host rocks from limestone to jasperoid quartz. The Stage 2 assemblage is composed of four populations

of pyrite (P2a, P2b, P2c, and P2d), three forms of jasperoid quartz (Q2a, Q2b, and Q2c), and the mineral galkhaite (G2). These minerals exhibit the following paragenetic sequence (Table 3).

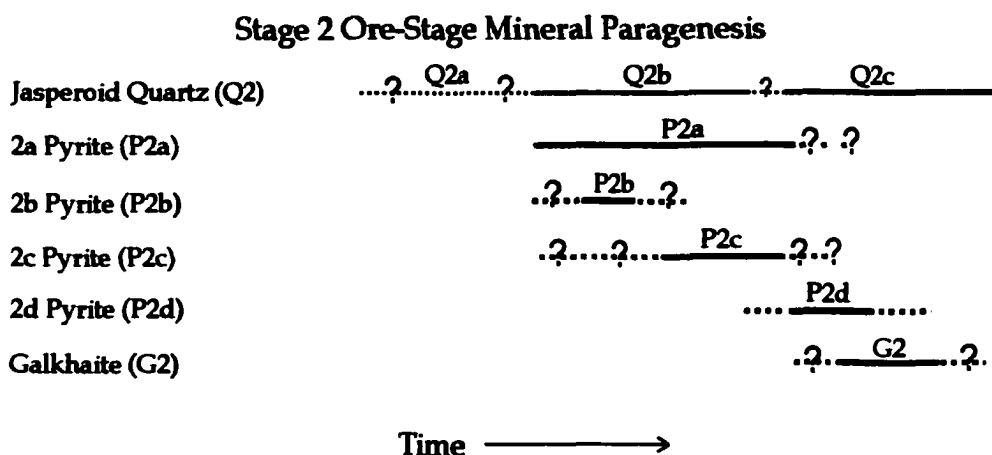


Table 3. Paragenetic sequence observed for ore-stage minerals.

#### Ore-Stage Fe-Sulfide Minerals (P2a, P2b, P2c, and P2d)

The ore-stage Fe-sulfide minerals in the Getchell underground deposit typically occur within the decarbonatized and silicified meta-sedimentary rocks of the Cambrian Preble Formation. Four distinct populations of As-bearing Fe-sulfide minerals were identified by microscopy, EMP, and SIMS analyses. Gold-ore stage Fe-sulfide minerals occur as anhedral rims that have overgrown non-ore, Stage 1 Fe-sulfide minerals, or occur as finely disseminated framboid-like crystals. Abundant ultra-fine crystals of pyrite and marcasite give the ore-bearing rocks a dark, sooty appearance (Fleet and Mumin, 1997). Petrographically, ore-stage Fe-sulfide minerals exhibit anisotropy typical of both pyrite and marcasite and therefore, are referred to as pyrite/marcasite or ore-

stage Fe-sulfide minerals.

#### Pyrite/Marcasite (P2a)

P2a sulfide overgrowth rims on non-ore pyrite cores are generally 2–5  $\mu\text{m}$  thick. This type of Fe-sulfide rim exhibits a poor polish and low polishing relief in contrast to the P1 pyrite core. P2a rim-forming Fe-sulfide minerals are unzoned, form sharp contacts with the core, and have a porous or spongy appearance (Figures 11a-c).

#### Pyrite/Marcasite (P2b)

P2b pyrite/marcasite minerals exhibit spherical framboid-like morphologies that are generally  $\leq 5 \mu\text{m}$  in diameter. Some appear as porous puff-balls and contain a low relief “hole” in the center. The porous or spongy appearance results from an uneven polish. This Au-bearing sulfide mineral commonly is disseminated throughout the jasperoid groundmass (Figures 11a-c).

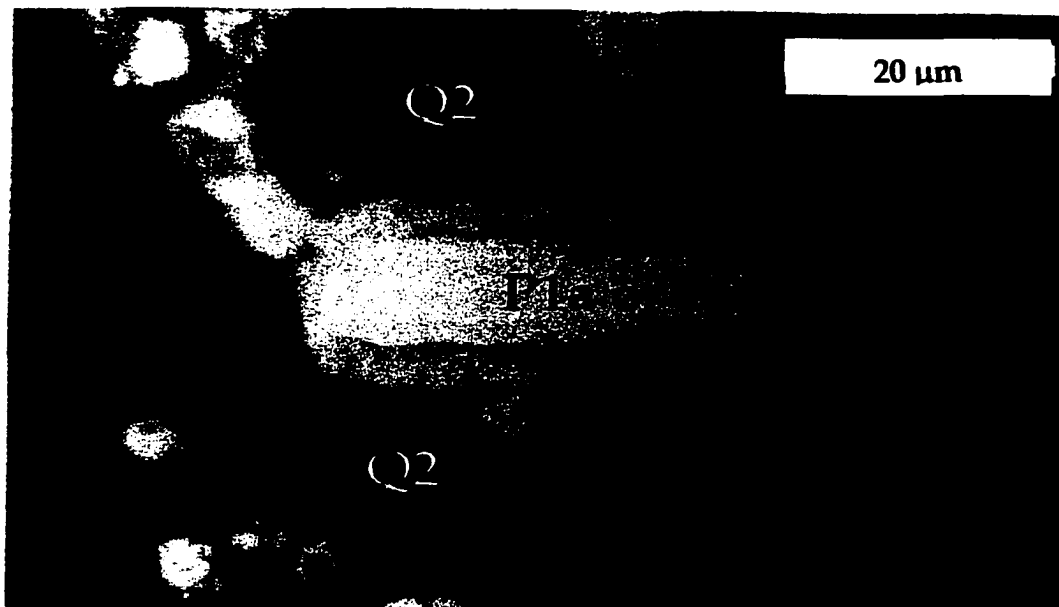


Figure 11a. RL photomicrograph of thin section UC0606-5000-184.00-15-157 showing P1a or b pyrite core rimmed by ore-grade P2a. Rim is approximately 2  $\mu\text{m}$  in diameter. The ore-stage P2a and P2b pyrite/marcasite is enclosed in Q2 jasperoid quartz.

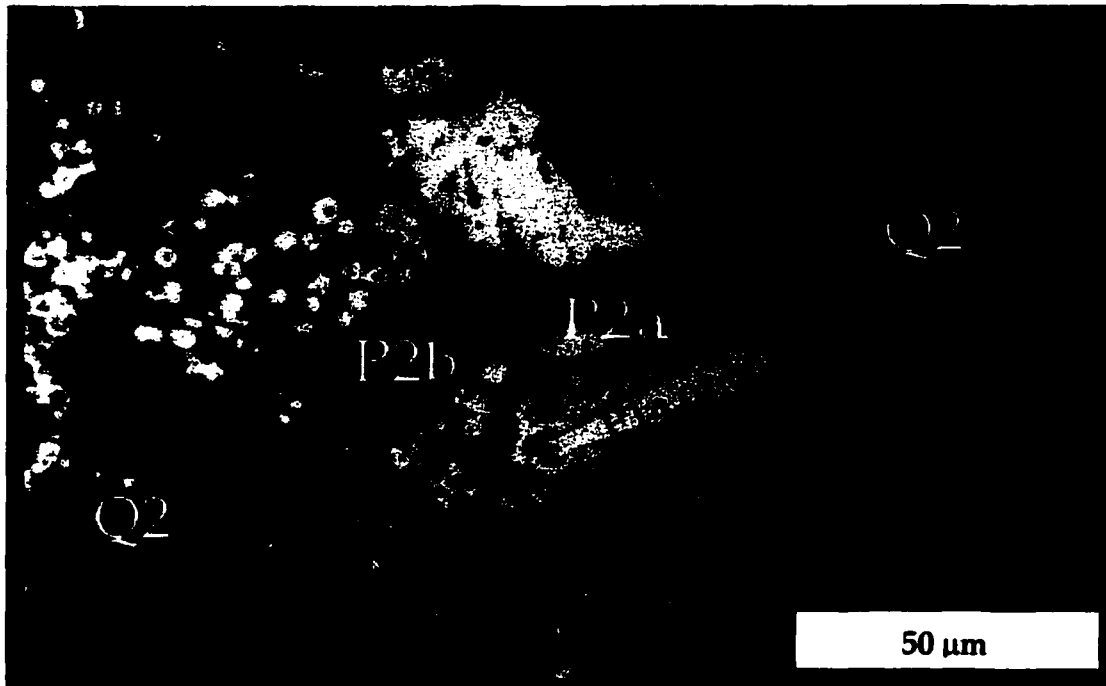


Figure 11b. RL photomicrograph of same Fe-sulfide crystal in Figure 11a at lower power; framboid-like crystals of P2b pyrite/marcasite are visible in surrounding Q2 jasperoid groundmass.

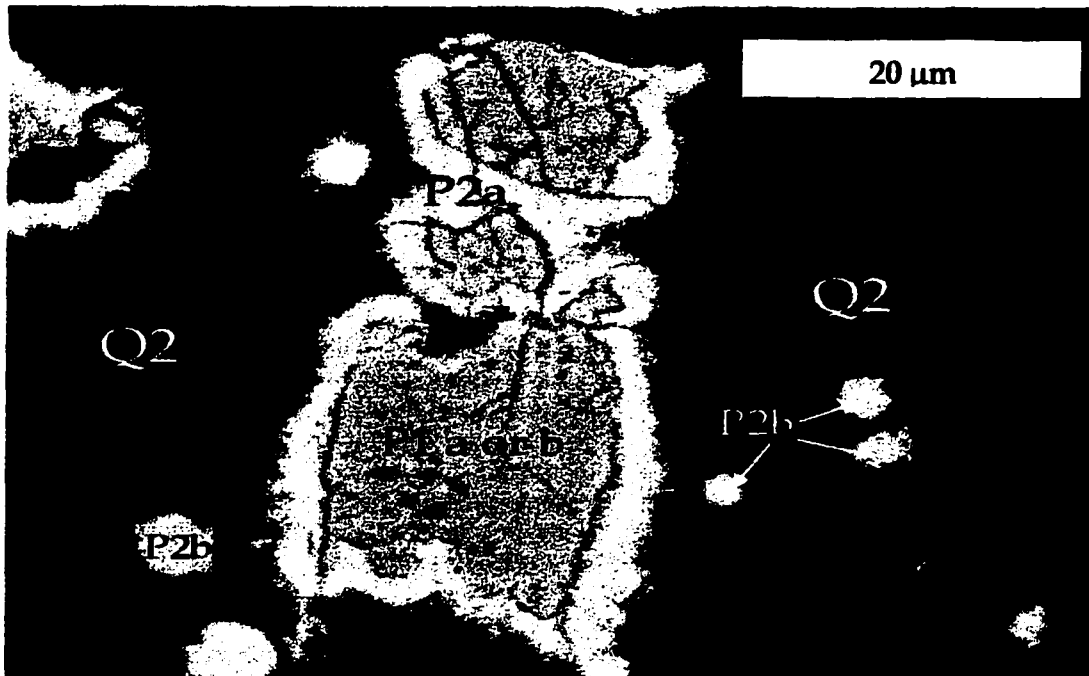


Figure 11c. BEI of P1a or b pyrite core rimmed by P2a pyrite/marcasite in thin section UC0606-5000-184.00-15-157. Note the textural differences between the P1 a/b core, the ore-stage P2a rims, and the P2b framboids.



### Pyrite/Marcasite (P2c)

Type P2c Fe-sulfide minerals form a second, very different type of rim. These rims, normally not visible with reflected light, become barely visible under reflected light in carbon-coated samples. The carbon coating gives the rims a very faint brownish-yellow color. The rims are unzoned and are highly visible under BEI and SEI because of the compositional differences from the cores. The polish, relief, and texture of this Fe-sulfide rim are similar to the core pyrite and the rims do not have a porous or spongy texture like the P2b pyrite/marcasite rims. The core pyrite is typically anhedral, rounded, and rarely, more porous than the rims. The P2c rims are the thickest rims observed, reaching 12  $\mu\text{m}$  (Figure 12).

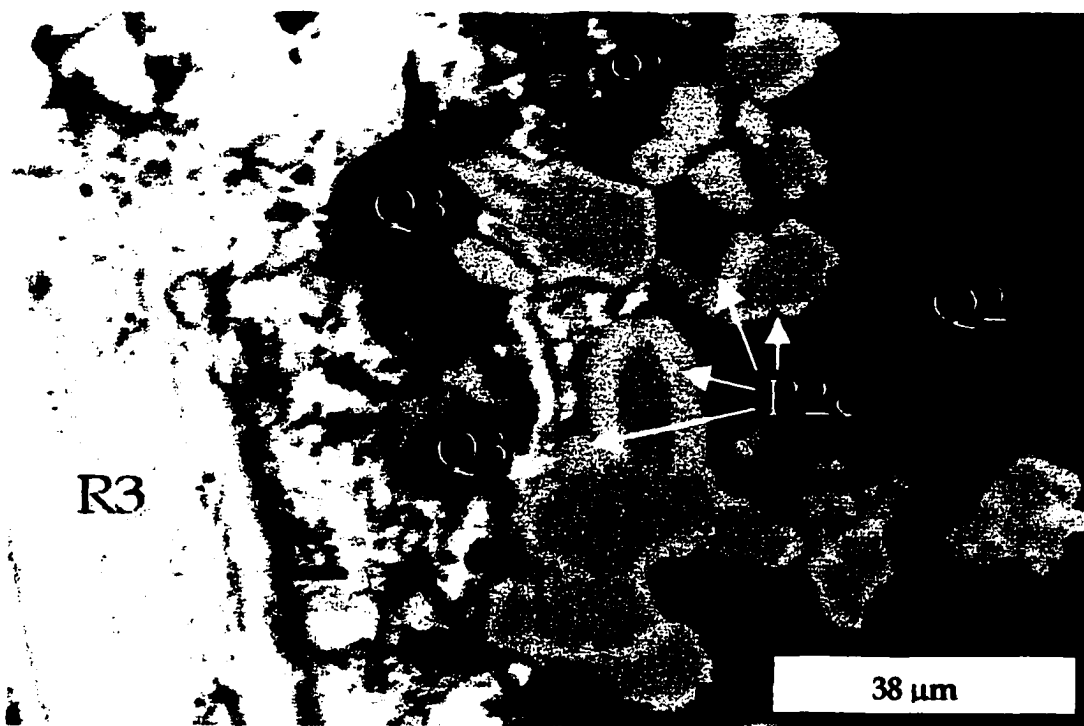


Figure 12. BEI of P1a or b pyrite core rimmed by high-grade P2c pyrite/marcasite in thin section UC0845-4850-160.00-13-32. Note the lack of textural relief between core pyrite and pyrite/marcasite rim. Bright white region is a vein of late-ore stage R3 realgar.

### Pyrite/Marcasite (P2d)

The fourth type of ore-stage pyrite is the most abundant and most morphologically distinct Fe-sulfide mineral present in the ore-stage minerals. P2d crystals are typically pink-brown to brownish-yellow in color and form large, irregularly shaped, coarse sulfide masses ranging in size from less than 5  $\mu\text{m}$  to greater than 1000  $\mu\text{m}$ . P2d pyrite/marcasite crystal surfaces have a good to poor polish and exhibit a cracked and porous texture (Figure 13). Faint pyrite/marcasite rims are occasionally observed; these rims are commonly 1  $\mu\text{m}$  in thickness and are barely visible by BEI. Murowchick (1992) concluded that pyrite/marcasite crystals with porous and cracked textures may have formed by inversion of marcasite to pyrite. Pyrite/marcasite inversion yields pyrite with an overall shape similar to the original marcasite crystal,

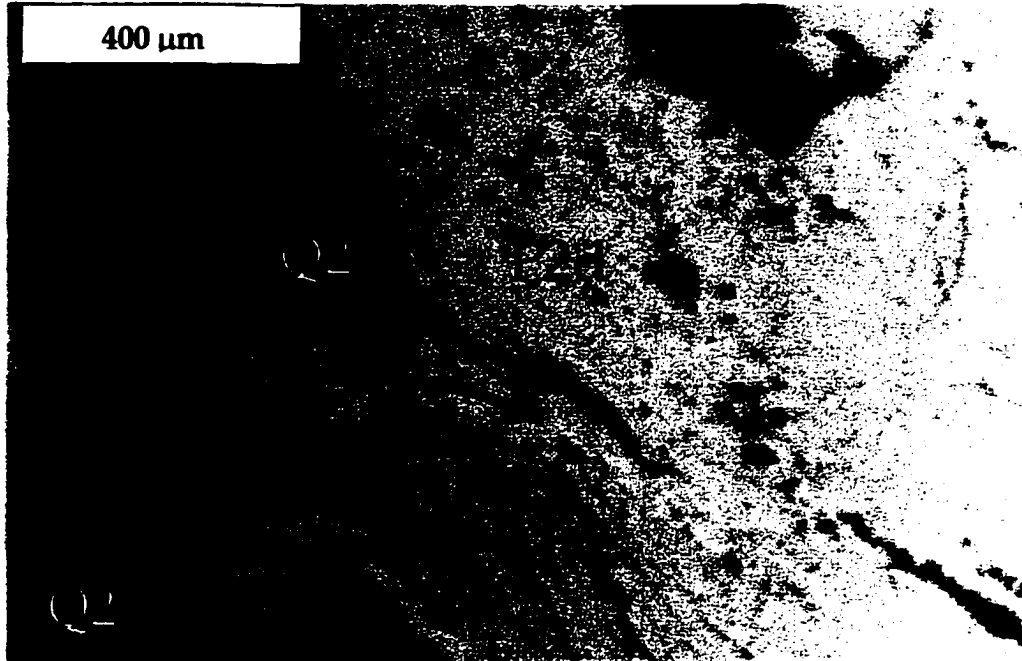


Figure 13. RL photomicrograph of thin section UC1079-4580-181.50-38-197 showing P2d porous pyrite/marcasite, within Q2 jasperoid quartz. Note the slightly lighter colored rims.

pores oriented along crystallographic axes, and crimson anisotropy (Murowchick, 1992). These attributes were not observed with P2d Fe-sulfide minerals in this study. The observed textures for P2d Fe-sulfide mineral masses suggest formation by intergrowth and agglomeration of irregularly shaped Fe-sulfide crystals.

### Jasperoid Quartz (Q2)

Several stages of jasperoid quartz make up the most abundant mineral in the ore-stage assemblage. The term “Q2” is used as a general term for all ore-stage jasperoid quartz (Table 3). Jasperoid quartz is an ore-stage mineral because ore-stage Fe-sulfide minerals are encompassed solely by ore-stage jasperoid. The ore-stage jasperoid quartz typically contains unidentifiable opaque solid inclusions and variable amounts of calcite and apatite as inclusions. Q2 typically exhibits a reticulate, jig-saw puzzle texture of variable crystal size. Apatite is irregularly distributed, and much of the jasperoid is free of apatite inclusions. Additionally, jasperoid quartz crosscuts pre-ore stage barite crystals, and Q1 pre-ore vein quartz.

The reticulate jig-saw puzzle texture, variable crystal size and the abundant calcite inclusions within the jasperoid crystals indicate that the jasperoid has replaced calcite (Cline and Hofstra, 2000). In regions where calcite replacement was incomplete, early calcite is present as calcite inclusions within the jasperoid quartz crystals. The reticulate texture of the jasperoid provides evidence for the precipitation of silica as crystalline quartz rather than as a silica gel; this conclusion implies that jasperoid formation occurred at moderate, rather than low, hydrothermal temperatures (Lovering, 1972).

In samples from mineralized zones within the Gatchell mine, P2a and P2b pyrite/marcasite were encompassed within the outer rims of jasperoid quartz crystals, or were concentrated between quartz crystal boundaries. The incorporated or trapped P2a and P2b crystals and very small unidentifiable ( $<1\ \mu\text{m}$ ) opaque minerals trapped between the quartz crystal faces give the Q2 jasperoid a dirty appearance (Figure 14). The ore-stage jasperoid quartz can be subdivided into three distinct morphologies (Table 3).

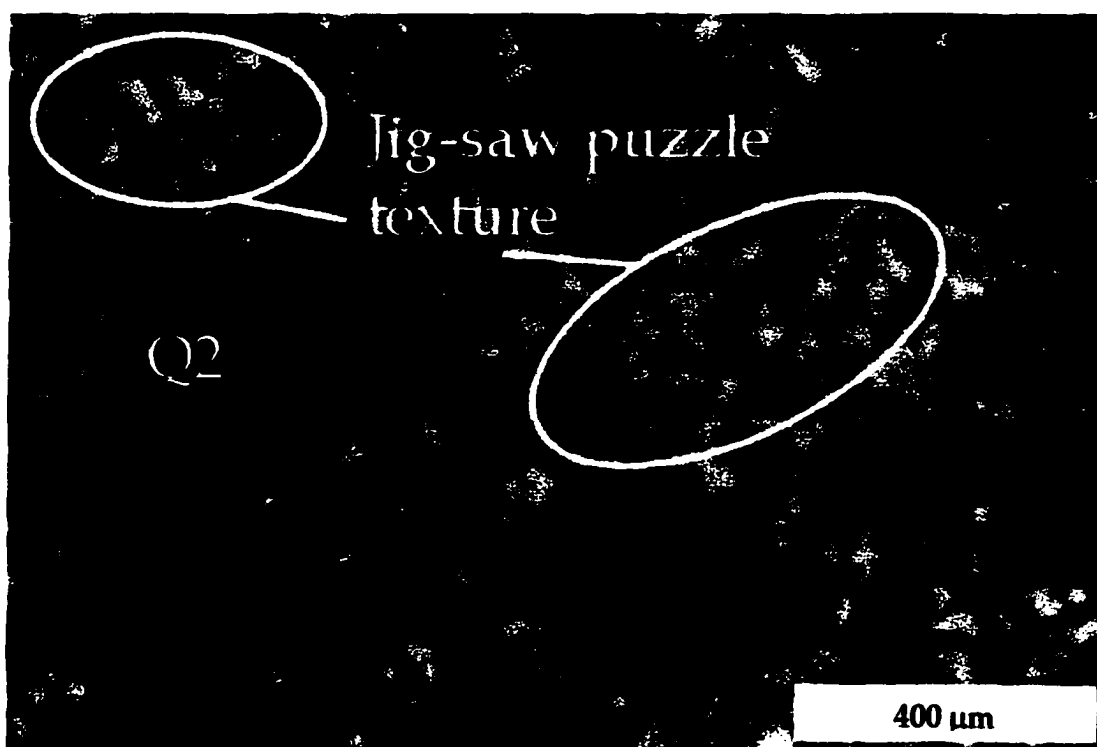


Figure 14. TL, CPL photomicrograph of Q2 jasperoid quartz in thin section UC1079-4580-181.50-38-176. Note variable crystal size and interlocking texture of the crystals and the dark unidentifiable opaque minerals trapped between the quartz crystal faces.

### Jasperoid Quartz (Q2a)

The earliest ore-stage quartz, Q2a (Table 3), often exhibits a very fine, reticulate, crystal texture that appears to be the initial stage of silicification in incompletely or partially replaced host rocks (Figure 15). This quartz contains no visible solid or fluid inclusions and is not associated with Fe-sulfide minerals or other opaque minerals. Q2a does not enclose ore-stage pyrite.

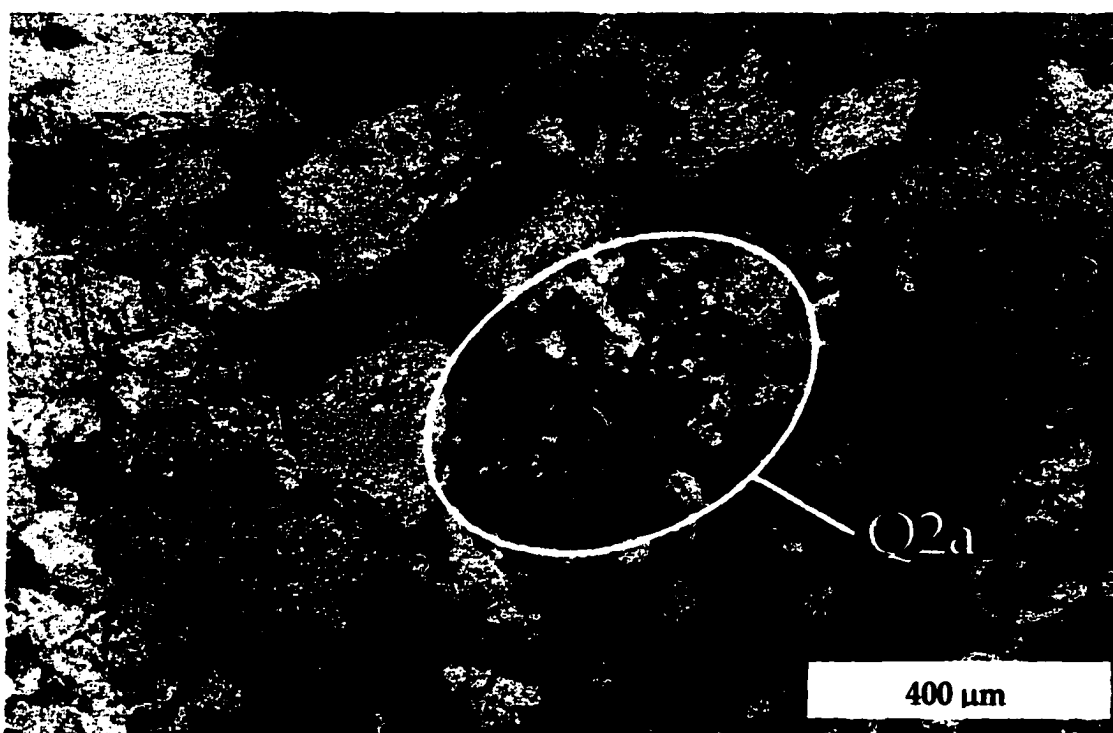


Figure 15. TL, CPL photomicrograph of Q2a in thin section UC1079-4580-181.50-38-149 showing incomplete early ore-stage jasperoid mineralization.

### Jasperoid Quartz (Q2b)

Ore-stage Q2b jasperoid is more coarsely crystalline than Q2a, and Q2b contains calcite inclusions, very fine crystals of ore-stage Fe-sulfide minerals, and other opaque minerals. Ore-stage P2a, P2b, P2c, and P2d Fe-sulfide minerals are located between and

partly incorporated into the inner edges of the Q2b jasperoid crystal boundaries. Q2b ore-stage jasperoid crystals containing ore-stage Fe-sulfide minerals, calcite, and opaque inclusions often exhibit cores that are free of opaque mineral inclusions; these “clean” cores are interpreted to be Q2a (Figure 16).

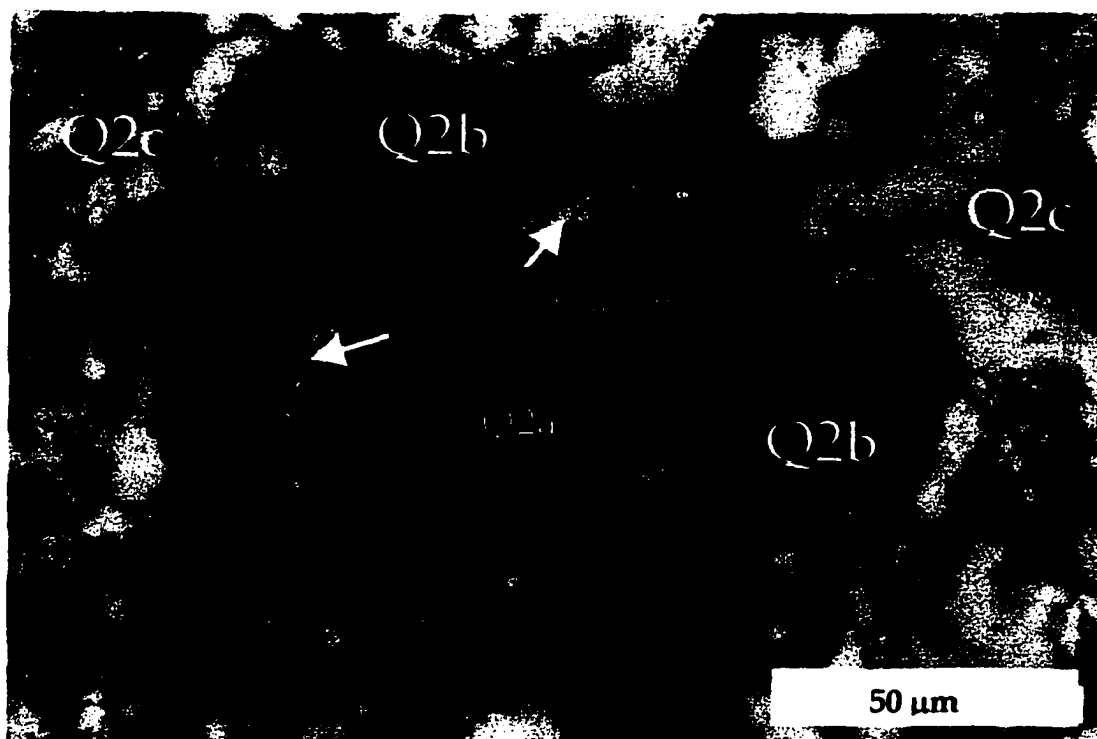


Figure 16. TL, CPL photomicrograph of thin section UC0519-4850-173.50-15-139 showing Q2b jasperoid with an inner growth zone containing small calcite inclusions. The Q2b crystal is surrounded by calcite inclusion-free Q2c jasperoid.

#### Jasperoid Quartz (Q2c)

The latest ore-stage jasperoid, Q2c, contains only small opaque minerals (less than 1  $\mu\text{m}$ ), no calcite inclusions, and often encloses the Q2b jasperoid quartz (Figure 16). Opaque and ore-stage Fe-sulfide minerals (P2a, b, c, and d) are located between and partly incorporated into the inner edges of the Q2c jasperoid (Figures 17a-b).

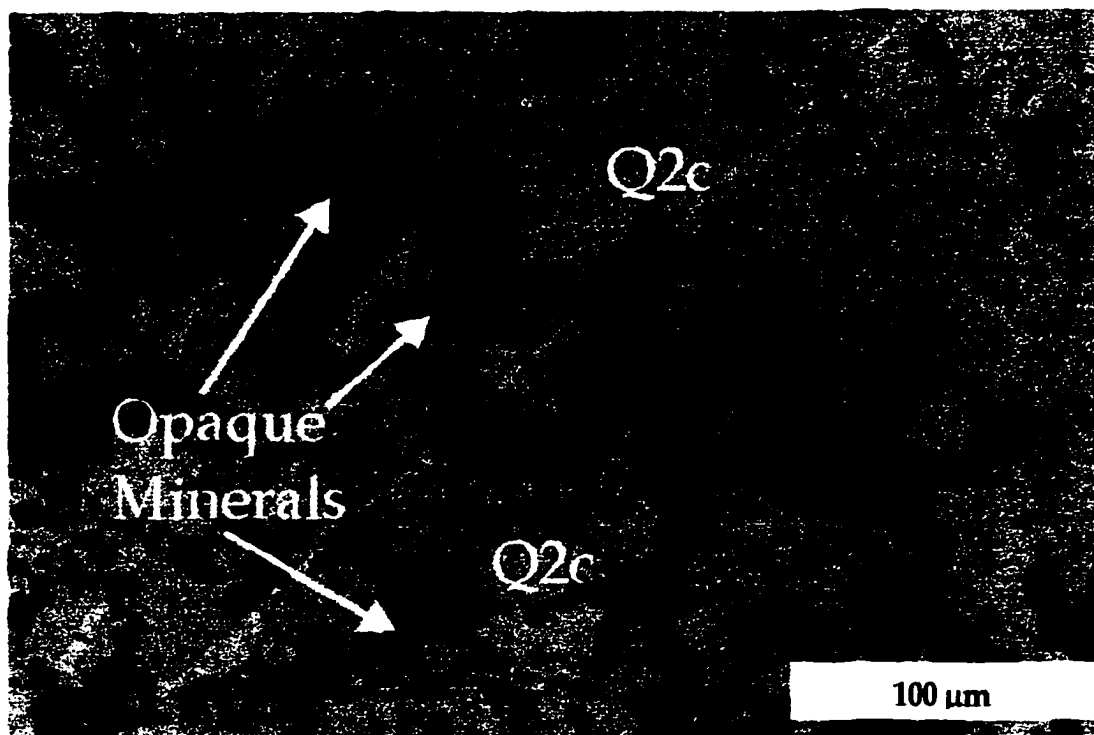


Figure 17a. TL, PPL photomicrograph of thin section UC0606-5000-184.00-15-157 showing Q2c jasperoid quartz with ore-stage pyrite/marcasite and opaque minerals between and within the quartz crystal boundaries.

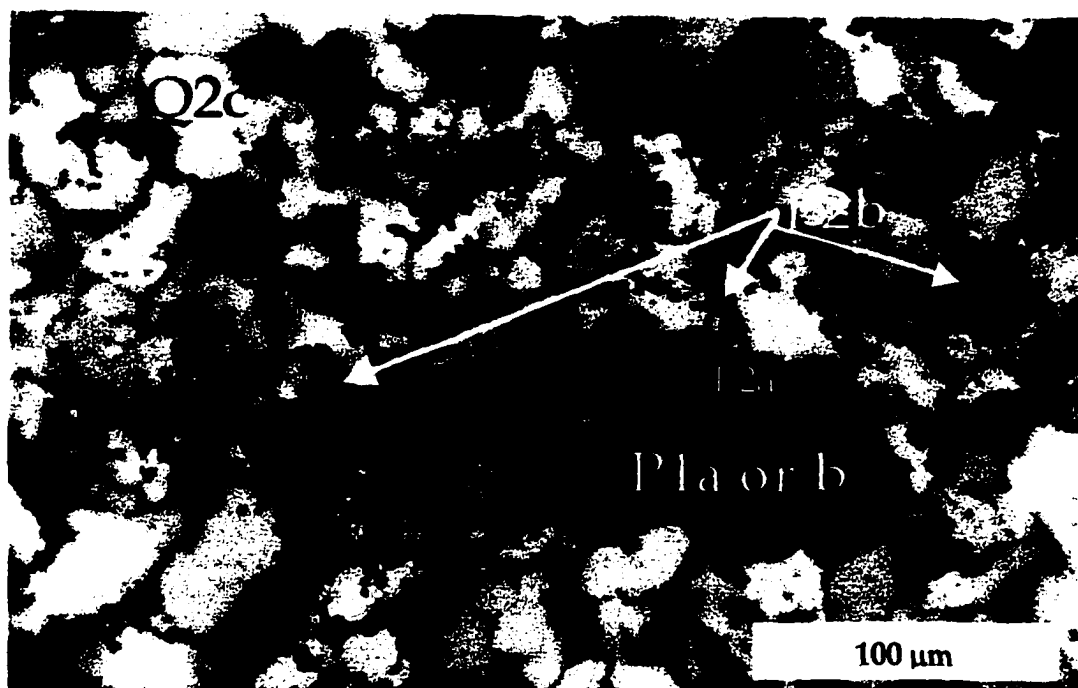


Figure 17b. TL photomicrograph of Q2c jasperoid in thin section UC0606-5000-184.00-15-157 showing P2a and P2b Fe-sulfide minerals between and partially incorporated into the crystals faces of calcite inclusion-free Q2c.

Preliminary scanning cathodoluminescence (CL) imagery revealed varying degrees of luminescence of jasperoid quartz in the ore-stage assemblages. Ore-stage Fe-sulfide minerals were trapped between Q2 jasperoid quartz crystals that had non-luminescent Q2a cores and highly luminescent Q2b or Q2c rims (Figure 18).

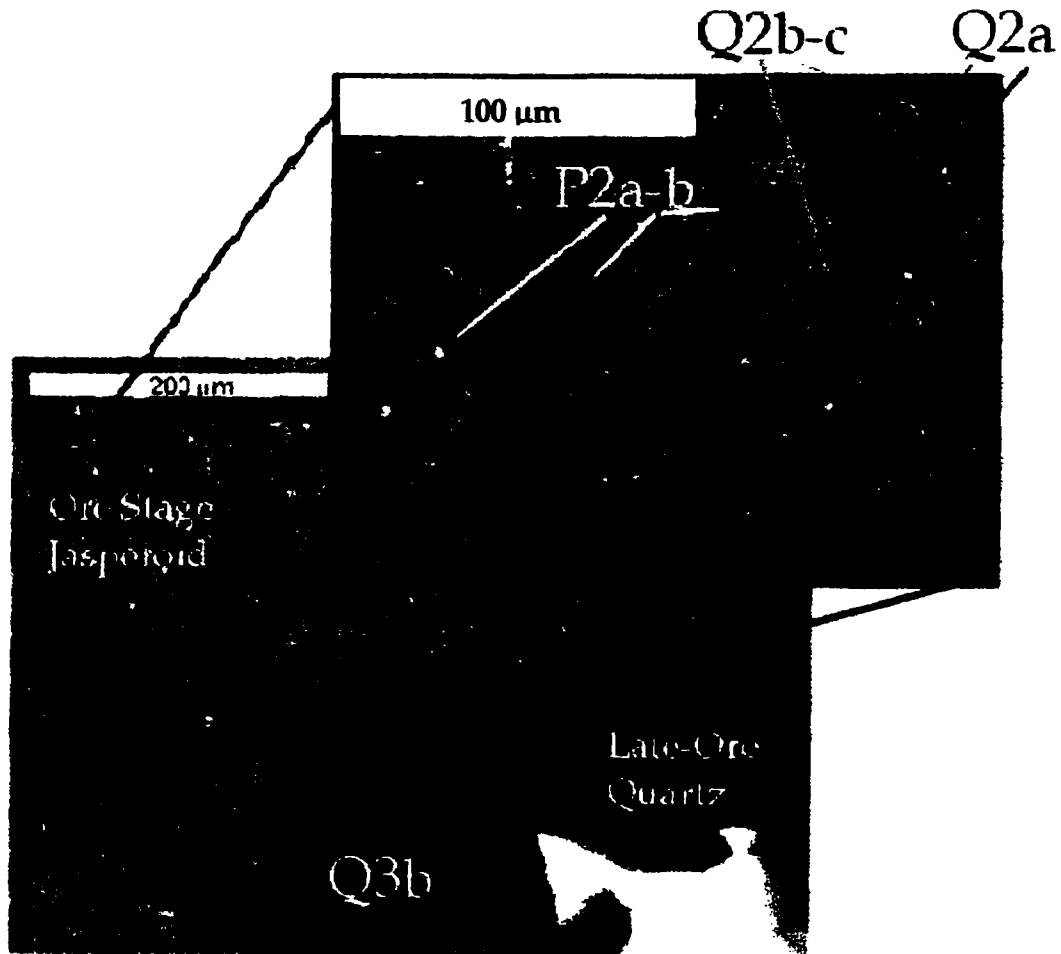


Figure 18. Cathodoluminescence image of thin section UC0606-5000-184.00-15-157 showing Q2 ore-stage and late-ore stage Q3b quartz. Note the poor luminescence of the Q2a jasperoid cores, and bright luminescence of Q2b and c rims adjacent to bands of ore-stage P2a and b Fe-sulfide opaque minerals.



Galkhaite  $(\text{Cs, Tl})(\text{Hg, Cu, Zn})_6(\text{As, Sb})_4\text{S}_{12}$

The galkhaite observed in this study is a rare sulfosalt mineral that is associated with pyrite, realgar, orpiment, and stibnite at Getchell. Galkhaite discovered at the Getchell mine was described by Botinelly et al. (1973) and Dunning (1988). This mineral forms cubes that are commonly intergrown (Figure 19a-b). The presence of euhedral crystals, commonly within vuggy zones, indicates precipitation in open space. Small cubic galkhaite crystals also were observed to be engulfed completely by Q2 jasperoid in both hand sample and microscopically. EMP, SEM, and BEI analyses on galkhaite samples show that galkhaite was replaced locally along fractures by cinnabar and metacinnabar (Stolburg and Dunning, 1985) (Figure 19b and Appendix 4).

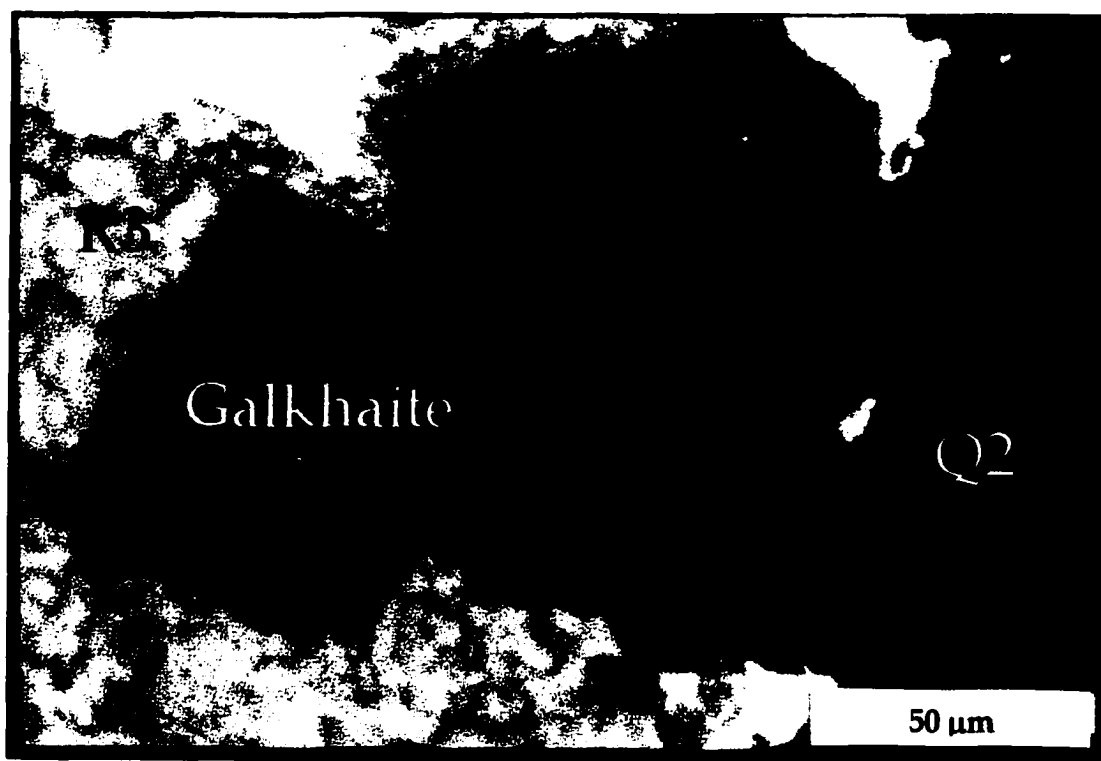


Figure 19a. TL, PPL photomicrograph of thin section UC0845-4850-160.00-13-32 showing galkhaite crystals overgrown by late-ore stage R3 realgar.

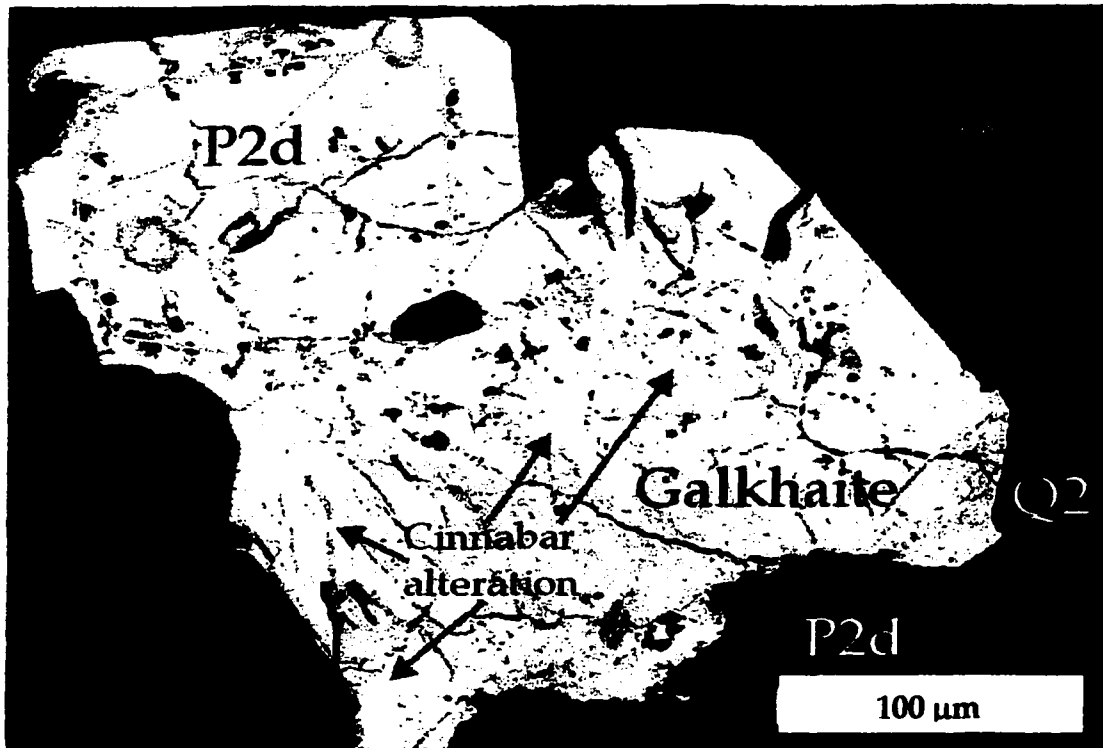


Figure 19b. BEI of galkhaite crystal in thin section UC0845-4850-160.00-13-32. The same crystal is shown in Figure 19a, rotated  $\sim 75^\circ$  clockwise. Bright white areas along fractures within the larger crystal are cinnabar. The P2d Fe-sulfide crystals (dark crystals along yellow line) are aligned along a growth zone in the galkhaite (chemical analyses in Appendix 4). Textures show that during galkhaite crystal growth, P2d crystals were forming and were enclosed by the galkhaite. Q2 subsequently overgrew galkhaite and P2d.

#### Discussion of Ore-Stage Paragenesis

Ore-stage pyrite precipitation was preceded and accompanied by decalcification and silicification of the host rocks by Q2a. Jasperoid quartz continued to replace the host limestone with precipitation of Q2b and Q2c jasperoid, which incorporated materials that survived decalcification. Gold- and arsenic-bearing Fe-sulfide minerals (P2a, b, c, and d) and galkhaite, which precipitated during Q2b and Q2c formation, were overgrown and incorporated by the jasperoid quartz groundmass.

Q2b contains both ore-stage Fe-sulfide minerals and calcite inclusions, indicating

that conditions were fluctuating near calcite stability when Q2b began to precipitate. Q2c is coarser and contains smaller and fewer opaque inclusions than Q2b, and contains no calcite inclusions. The lack of calcite inclusions indicates that at the time of precipitation of Q2c, calcite was no longer stable and had been completely removed.

The observed textures of Q2b and Q2c indicate that ore-stage pyrite inclusions were trapped within the outer rims of the jasperoid crystals and between the quartz crystal faces. Ore-stage pyrite/marcasite continued to be enclosed by quartz during the waning stages of Q2c precipitation. The pyrite/marcasite mineralization precipitated in open spaces between jasperoid crystals, forming P2b framboids and P2a and P2c rims on P1a or b pyrite cores.

The morphologically and textually distinctive fourth type of ore-stage pyrite (P2d) suggests formation by intergrowth and agglomeration of irregularly shaped ore-stage Fe-sulfide crystals. The distinct morphology and texture indicate that the conditions that formed P2d pyrite/marcasite were different from the ore-stage conditions that formed types P2a, P2b, and P2c. Paragenetic relationships indicate that P2d was forming simultaneously during galkhaite crystal growth. Subsequently, crystals of P2d were enclosed by galkhaite and then both galkhaite and P2d were overgrown by Q2.

Cathodoluminescence imagery of ore-stage jasperoid quartz suggests that the composition of ore fluids changed as jasperoid precipitated. Cathodoluminescence images show that the silica in these specimens probably precipitated outward from crystal cores. The subtle trace element differences in quartz crystals suggest that they were continually exposed to small changes in fluid composition and acquired subtle trace element differences. Non-luminescent quartz cores are encompassed by brightly

luminescent quartz rims and are adjacent to and contain ore- stage Fe-sulfide minerals. This zoning suggests that the fluids responsible for the brightly luminescent outer rims of quartz may have been the ore fluids.

### Stage 3 – Late-Ore Stage Mineral Assemblage

Late-ore mineralization is characterized by open-space filling textures that conform to, or crosscut, both Stage 1 pre-ore and Stage 2 ore-stage minerals (Table 4). Minerals that compose Stage 3 include two forms of quartz and chalcedony (Q3a, Q3b, and Q3c); two forms of marcasite (P3a and P3b), one stage of stibnite (S3), orpiment (O3), veins of realgar (R3); and three types of calcite (C3a, C3b, and C3c). These minerals exhibit a consistent paragenetic sequence illustrated in Table 4. Elemental compositions of analyzed orpiment, realgar, and stibnite are listed in Appendix 4.

#### Stage 3 Late-Ore Stage Mineral Paragenesis

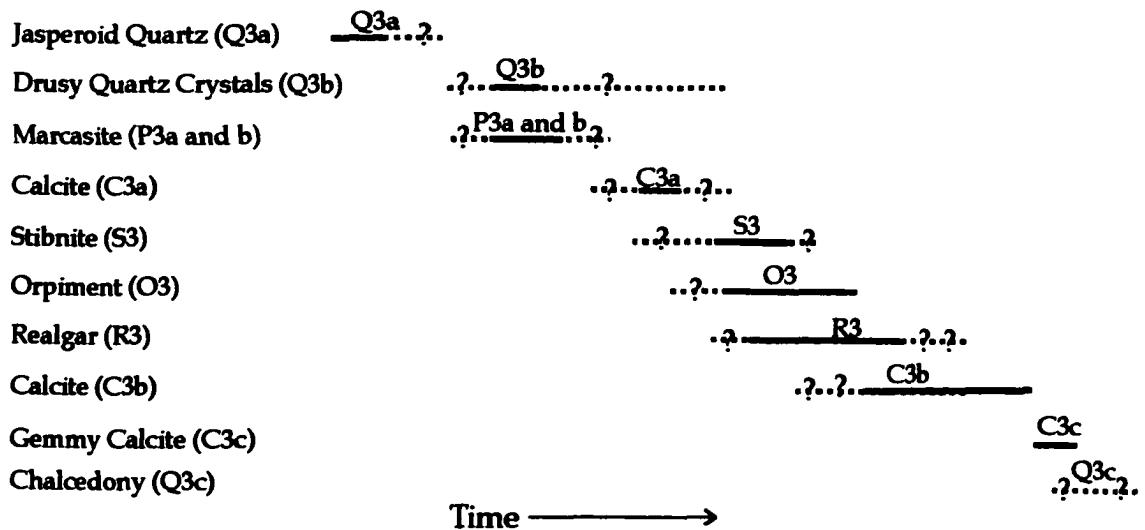


Table 4. Paragenetic sequence for late-ore stage minerals.

### Quartz (Q3a)

Q3a jasperoid encompasses Stage 2 jasperoid cores, which contain extremely fine crystals of calcite and opaque inclusions (Figure 20). Q3a late-ore stage jasperoid quartz (Table 4) can be distinguished from ore-stage Q2c jasperoid because it is coarsely crystalline and contains no Fe-sulfide minerals.

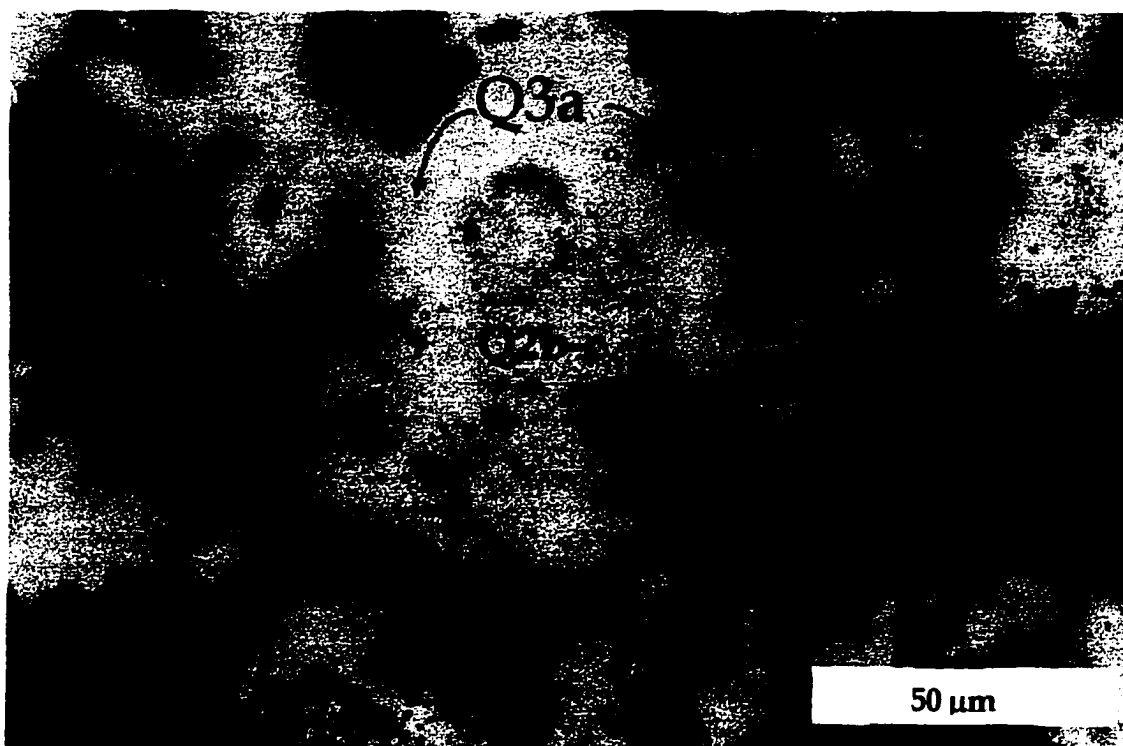


Figure 20. TL plane-polarized photomicrograph of thin section UC0519-4850-173.50-15-139 showing Q3a jasperoid. Note the opaque minerals trapped in the center of crystals (Q2 b or c) and the “clean” outer rim of Q3a.

### Quartz (Q3b)

Q3b quartz exhibits open-space filling, crustification textures along fractures and veins, and forms terminated drusy crystals (Figure 21). Q3b commonly forms overgrowths on Q2 jasperoid and on Stage 1 pre-ore C1a limestone. Although Q3b contains no ore-stage pyrite/ marcasite minerals, the quartz rarely contains small Stage 3 calcite, realgar, or stibnite inclusions within the outer growth zones and between the Q3b crystal crystals. Q3b quartz contains 2-phase, liquid-vapor fluid inclusions and is “cleaner” than ore-stage Q2 jasperoid quartz.



Figure 21. TL, CPL photomicrograph of thin section UC1075-4655-164.00-06-86 showing drusy Q3b quartz lining vug walls; vug was subsequently occluded by late stage C3c clear calcite.

Scanning cathodoluminescence imagery revealed zoning of late-ore stage drusy Q3b quartz crystals. Cathodoluminescence imagery of Q3b revealed oscillatory growth zones of different luminescent intensities within the euhedral crystals. In some Q3b crystals, the outermost growth zones are dark, and relatively non-luminescent (Figure 22).

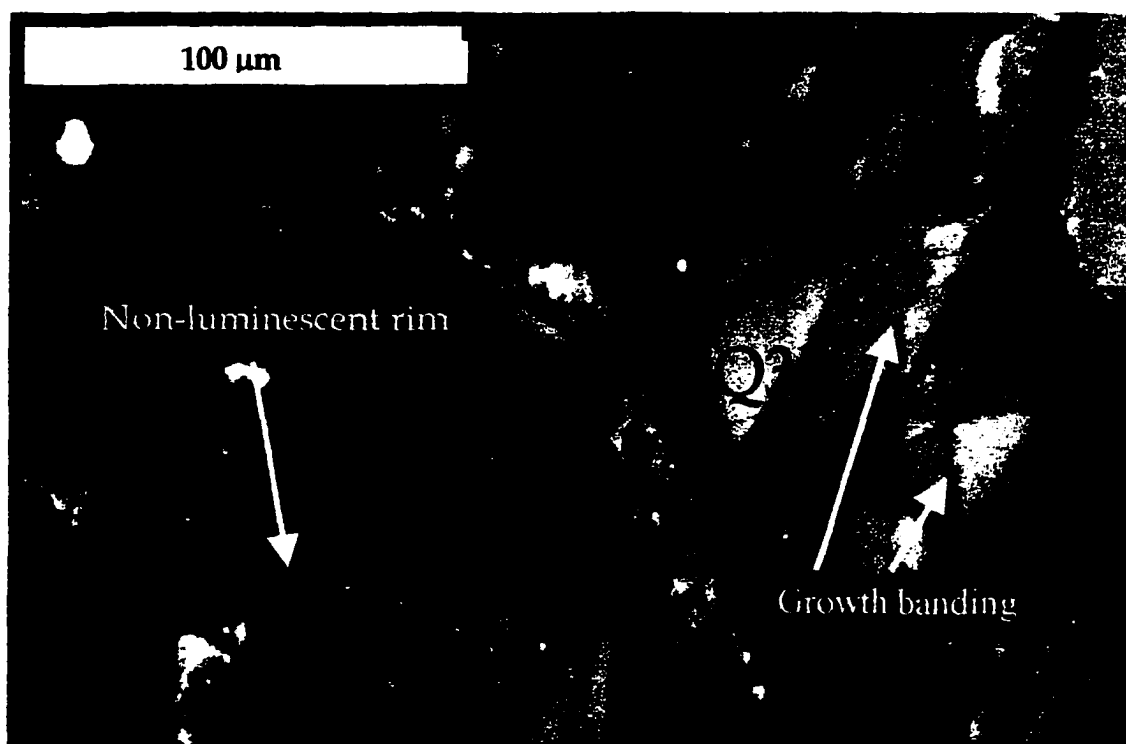


Figure 22. Cathodoluminescence image of thin section UC0606-5000-184.00-15-157 showing late-ore stage drusy quartz. Note the dim, yet visible oscillating growth banding of the drusy quartz and the non-luminescent outer rims of the Q3b quartz crystals.

### Marcasite (P3a and P3b)

Type P3a marcasite is bright white in reflected light, exhibits a good polish and high relief, and is overgrown by late-stage, “dirty” C3a calcite (Table 4). The marcasite forms both coarse, prismatic crystals (Figure 23a) and fine, lath-shaped crystals (Figure 23b).

Type P3b marcasite forms small, subhedral to anhedral cubes approximately 2  $\mu\text{m}$  in diameter. This marcasite also exhibits high relief and a good polish. P3b marcasite crystals rim the margins of veins filled with C3a late-stage calcite in contrast to P3a, which is within C3a (Figure 23c).

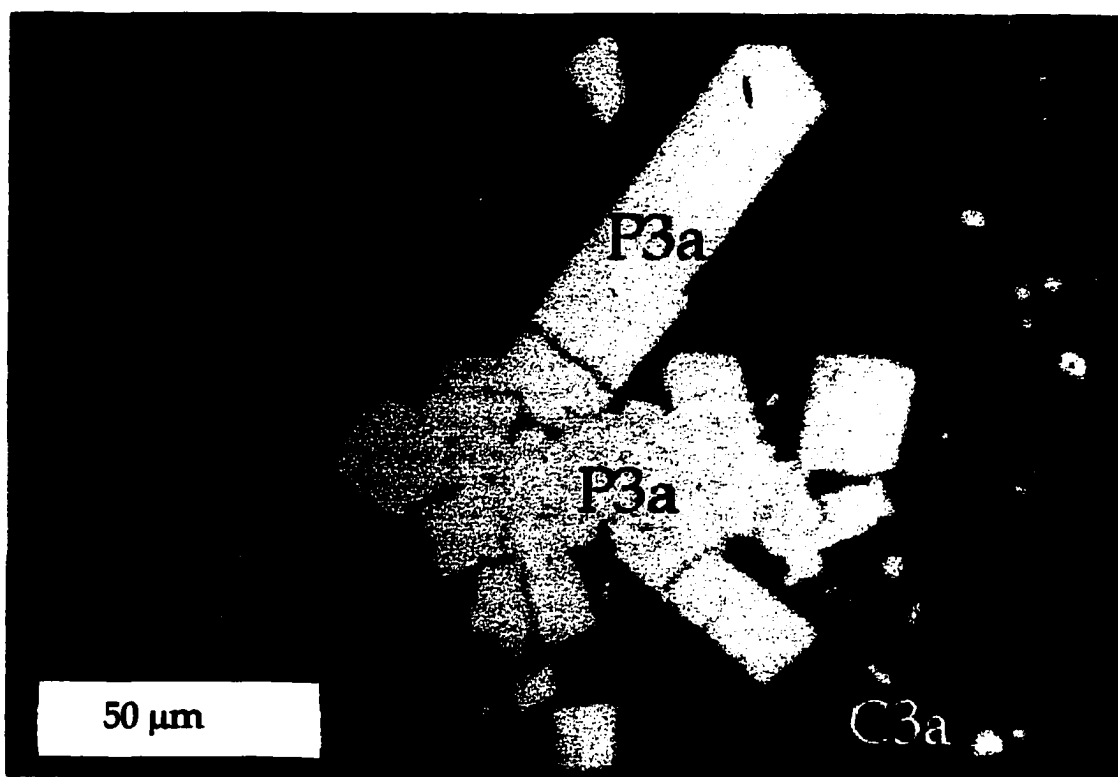


Figure 23a. RL photomicrograph of thin section UC1079-4850-181.50-38-85 showing P3a euhedral and prismatic marcasite.



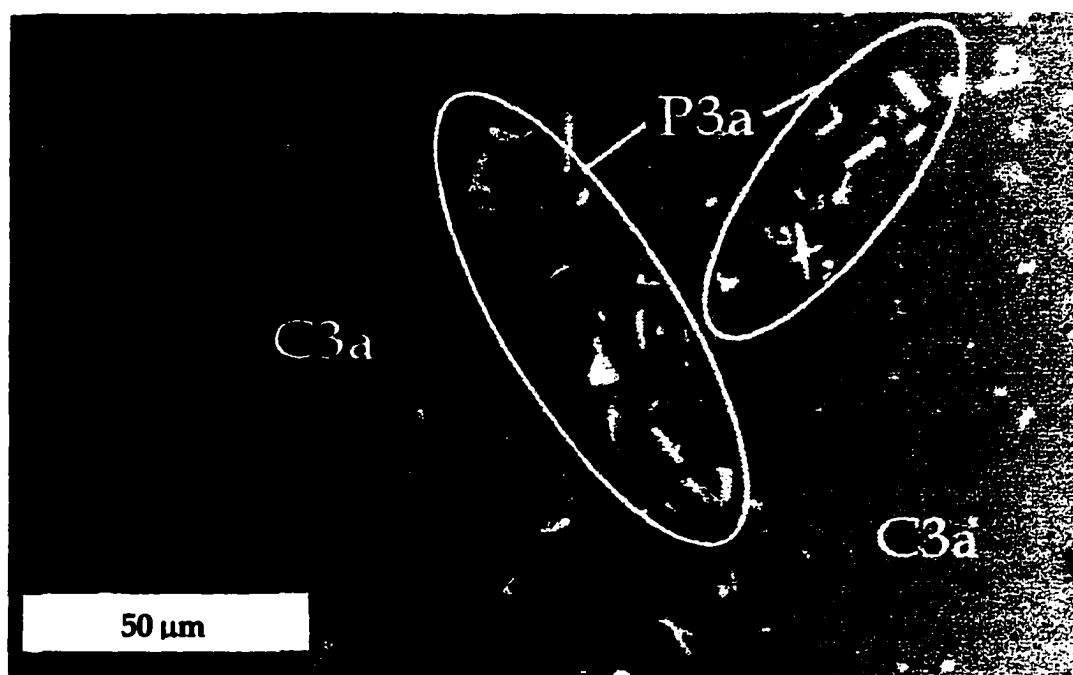


Figure 23b. RL photomicrograph of thin section UC1079-4850-181.50-38-85 showing fine crystals of lath-shaped P3a marcasite. Note that Figure 23a and b are at the same magnification.

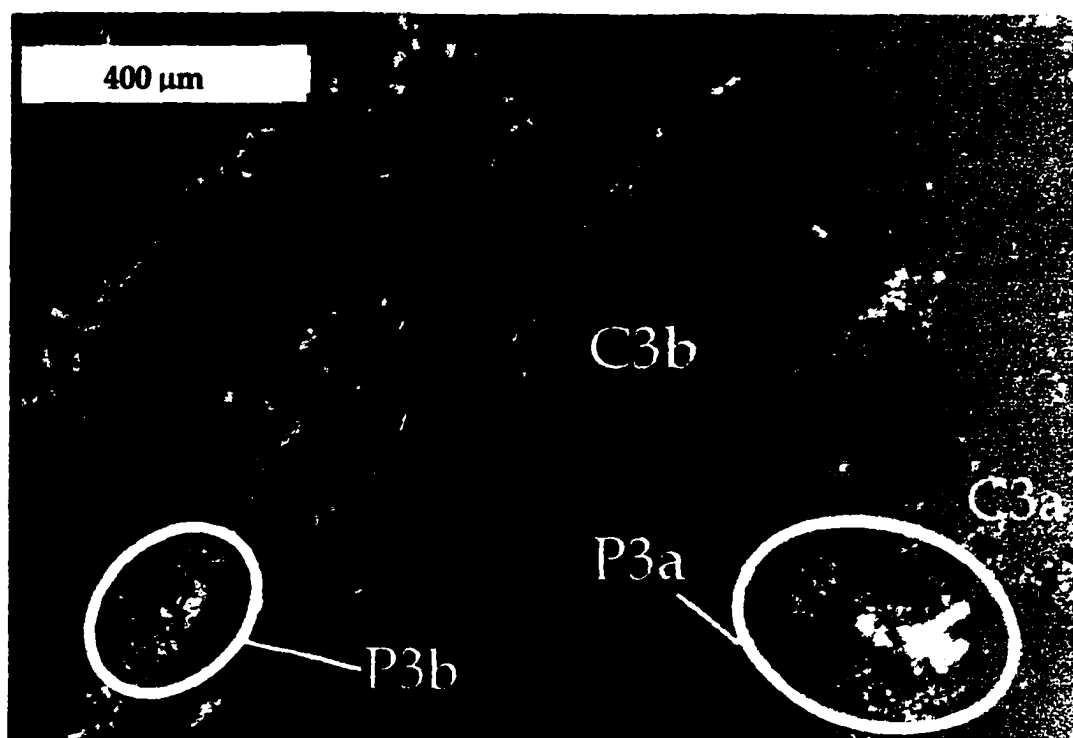


Figure 23c. RL photomicrograph of thin section UC1079-4850-181.50-38-85 showing P3b marcasite lining vein walls. Note that both types of P3a marcasite are evident within the marked region where the fine crystals of P3a appear as the very fine, white, "dusty" looking crystals surrounding the coarse euhedral marcasite.

### Calcite C3a

C3a calcite typically forms large masses and contains fine crystals of unidentified (Fe?) opaque minerals and P3 marcasite (Figures 23a-c). Calcite C3a contains no realgar or orpiment inclusions and also forms banded layers with C3b along the outer walls of fractures and veins. It is also distinguishable from the C1a limestone because it contains no vugs and is much more coarsely crystalline than limestone.

### Stibnite (S3)

Stibnite ( $\text{Sb}_2\text{S}_3$ ) (Appendix 4) often occurs with realgar, orpiment, and calcite as a late-stage, open-space filling mineral (Table 4). Stibnite precipitated as fine needles radiating outward from outer crystal faces of drusy Q3b into an open space or vug, and is commonly encapsulated by R3 realgar, C3c calcite, or incorporated within Q3b quartz (Figure 24).

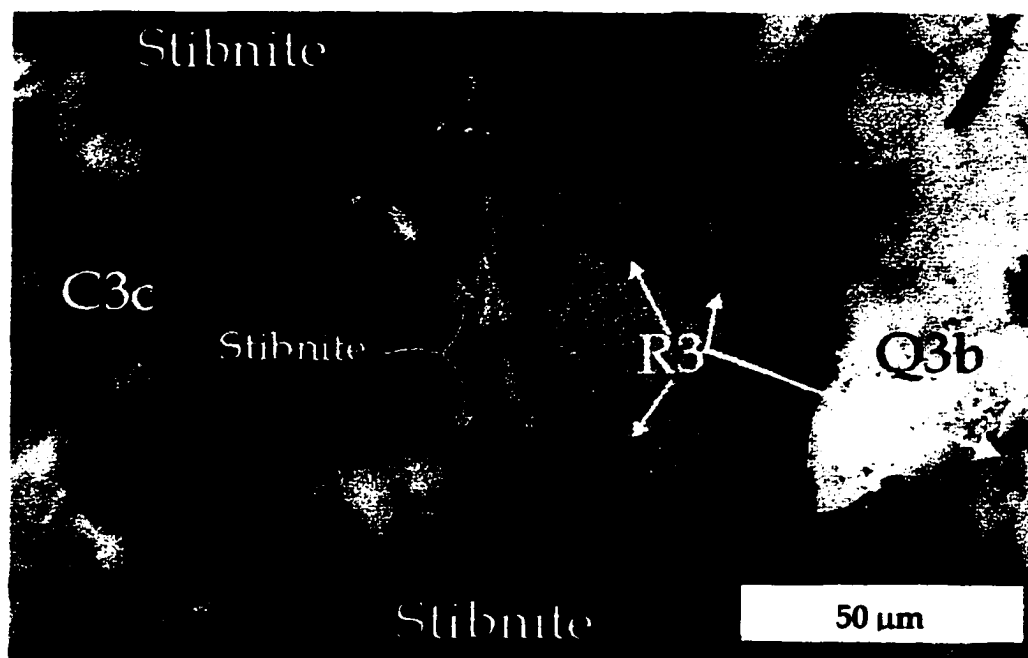


Figure 24. TL, CPL photomicrograph of R3 realgar inclusions within Q3b drusy quartz in thin section UC1075-4655-164.00-06-86. Stibnite also is present within outer growth zones in the Q3b quartz rims, and within C3c calcite.

### Orpiment (O3)

Orpiment ( $\text{As}_2\text{S}_3$ ) (Appendix 4) was found primarily as masses filling large fractures, and as yellow crystals encompassed by massive R3 realgar (Figure 25). The frequent observation of orpiment encompassed in massive realgar suggests that the orpiment formed prior to realgar precipitation (Table 4). Orpiment also occurs within realgar where realgar has partially altered to orpiment.

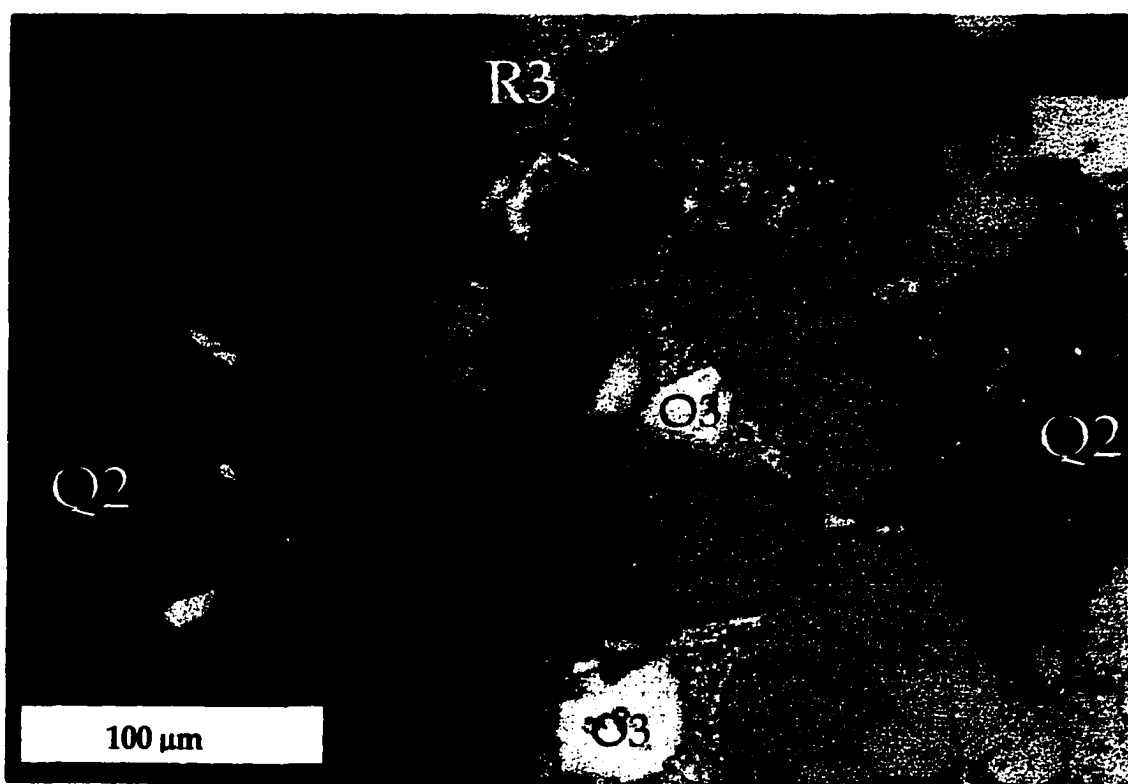


Figure 25. RL photomicrograph of thin section UC1082-4655-164.00-08-101 showing textural relationships between O3 orpiment, R3 realgar, and Q3b quartz.

### Realgar (R3)

Late-ore stage realgar (AsS) (Appendix 4) typically occurs as euhedral crystals and anhedral masses filling open spaces and cavities, and encompassing all earlier minerals (Figures 25, 26, and 27a - b) (Table 4). R3 also is present as inclusions within Q3a drusy quartz that lines cavity walls (Figure 24). Realgar commonly encapsulates stibnite crystals. Euhedral realgar faces in vugs and veins were overgrown by C3c calcite (Figure 26). R3 crystal interiors appear clean and unaltered.

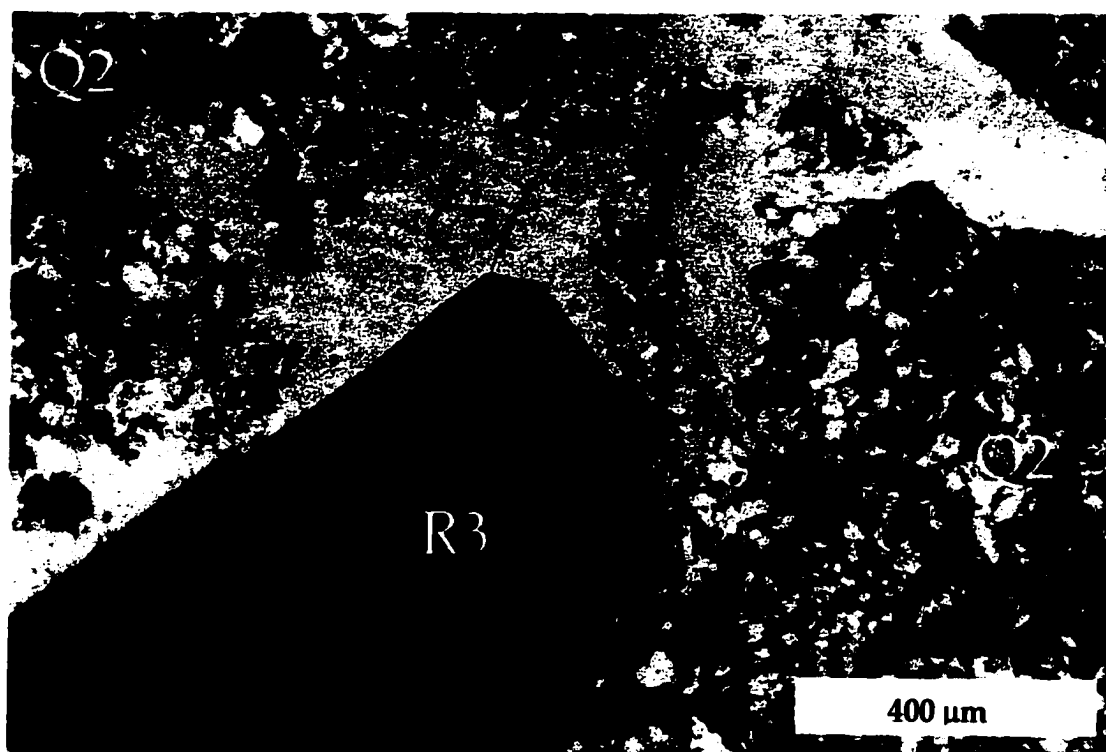


Figure 26. TL, CPL photomicrograph of thin section UC1082-4655-164.00-08-101 showing R3 realgar with euhedral faces, C3c calcite, and Q2 jasperoid.

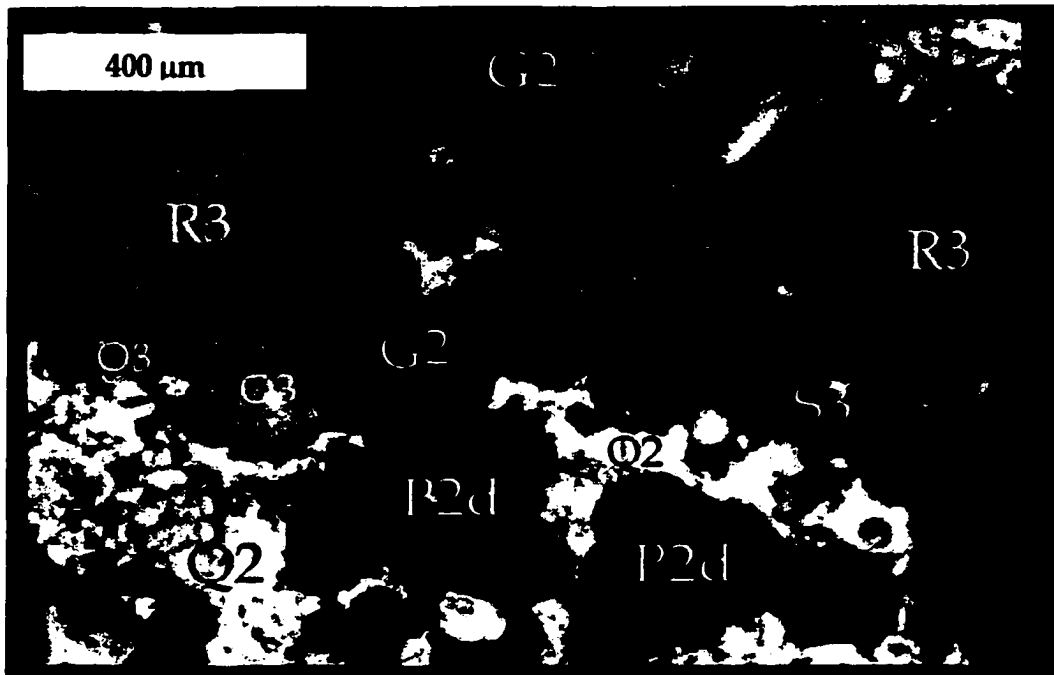


Figure 27a. TL, PPL photomicrograph of thin section UC0845-4850-160.00-13-32 showing textural relationships between P2d pyrite/marcasite, G2 galkhaite, Q2 jasperoid quartz, R3 realgar, O3 orpiment, and S3 stibnite.

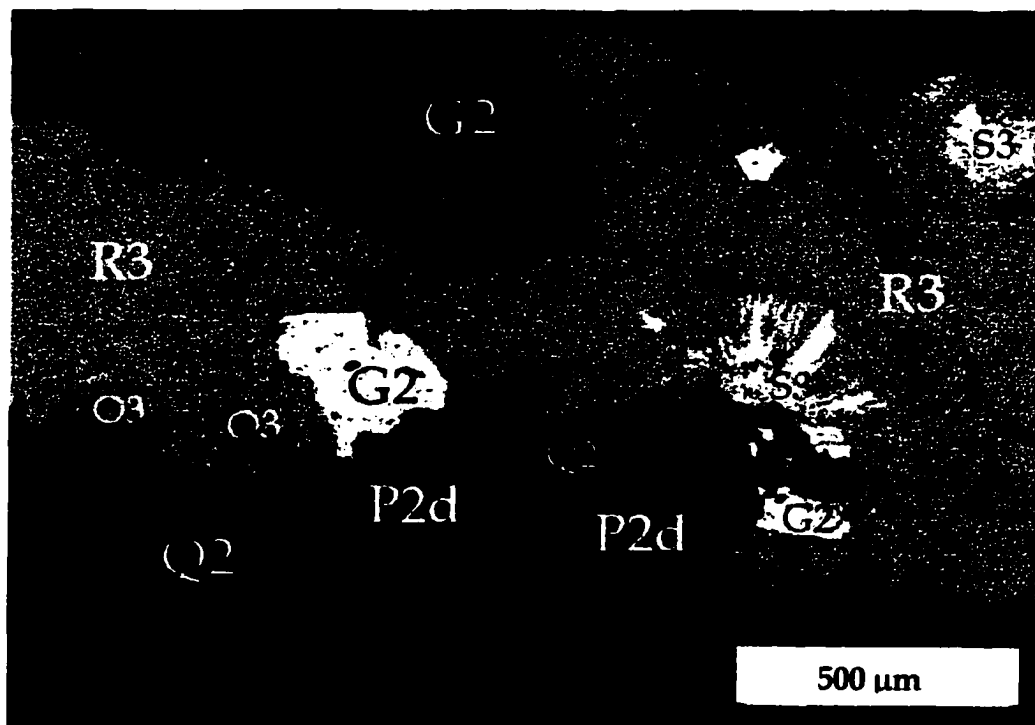


Figure 27b. BEI of same region as shown in Figure 27a; note the intergrown crystal boundaries between G2 galkhaite and P2d as compared to euhedral galkhaite faces overgrown by R3.

### Calcite (C3b and C3c)

C3b calcite typically forms the middle band of symmetrical calcite layers filling fractures and veins. This “dirty” calcite rarely contains both opaque minerals and very rare inclusions of realgar.

C3c calcite exhibits open-space filling textures and often forms or occupies the centers of vugs, veins, and fractures. Large, “clean” C3c calcite crystals crosscut or overgrow all previously formed minerals (Figures 21, 24, and 28a) (Table 4). This clear calcite commonly encapsulates R3 realgar crystals (Figure 26). Additionally, C3c fills vugs in the C1a limestone.

Calcite analyzed through cathodoluminescence imagery showed varying intensities of luminescence within layers of calcite that fill open spaces (Figure 28b). C3a luminesced weakly, C3b brightly, and the C3c pure gemmy calcite in the centers of the veins, did not luminesce (Figures 28a-b).

### Chalcedony (Q3c)

Q3c, rare chalcedony, was observed partially infilling open vugs within the ore-stage jasperoid groundmass (Figure 29).

### Discussion of Late-Ore Stage Paragenesis

Late-ore stage mineralization is characterized by a mineral assemblage (Table 4) that is superimposed upon the previously formed host, pre-ore, and ore-stage assemblages. Q3a late-ore stage jasperoid quartz contains no Fe-sulfide minerals and encompasses Stage 2 jasperoid cores. The relationship between Q3a and Q2 jasperoid quartz suggests that the precipitation of Q3a took place after ore-stage Fe-sulfides precipitated. Drusy crystals of Q3b precipitated along veins and fractures and

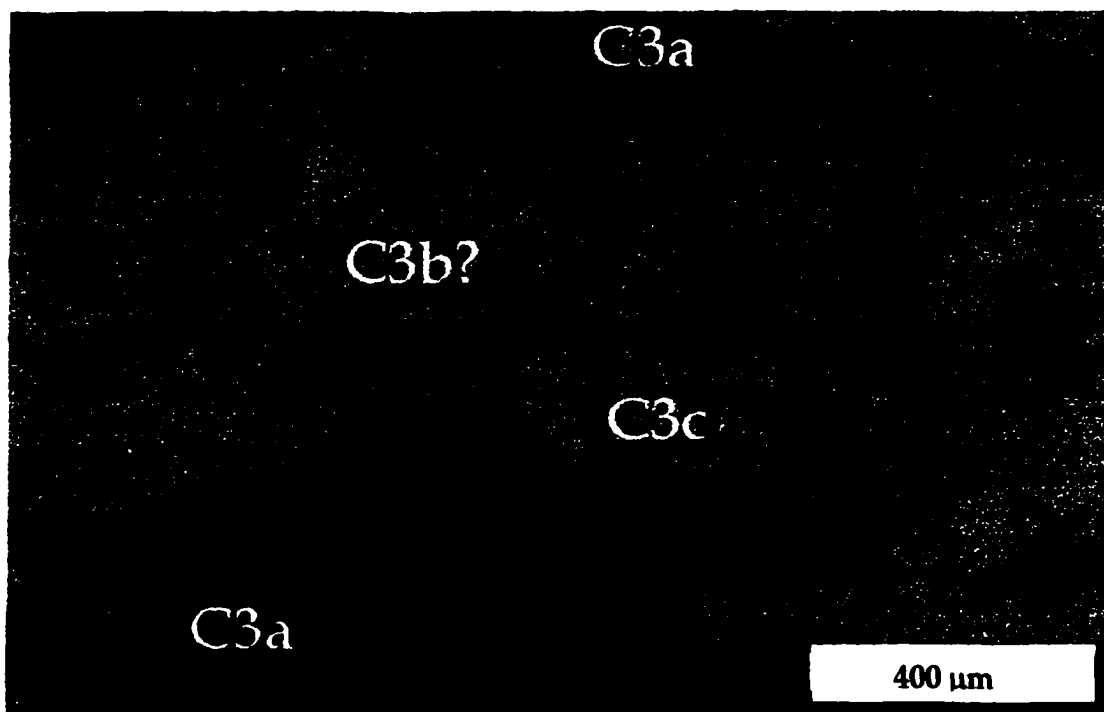


Figure 28a. TL, CPL photomicrograph of thin section UC0606-5000-184.00-15-157 showing bands of C3a, C3c, and possibly C3b. Note: small red dots are for comparison with Figure 28b.

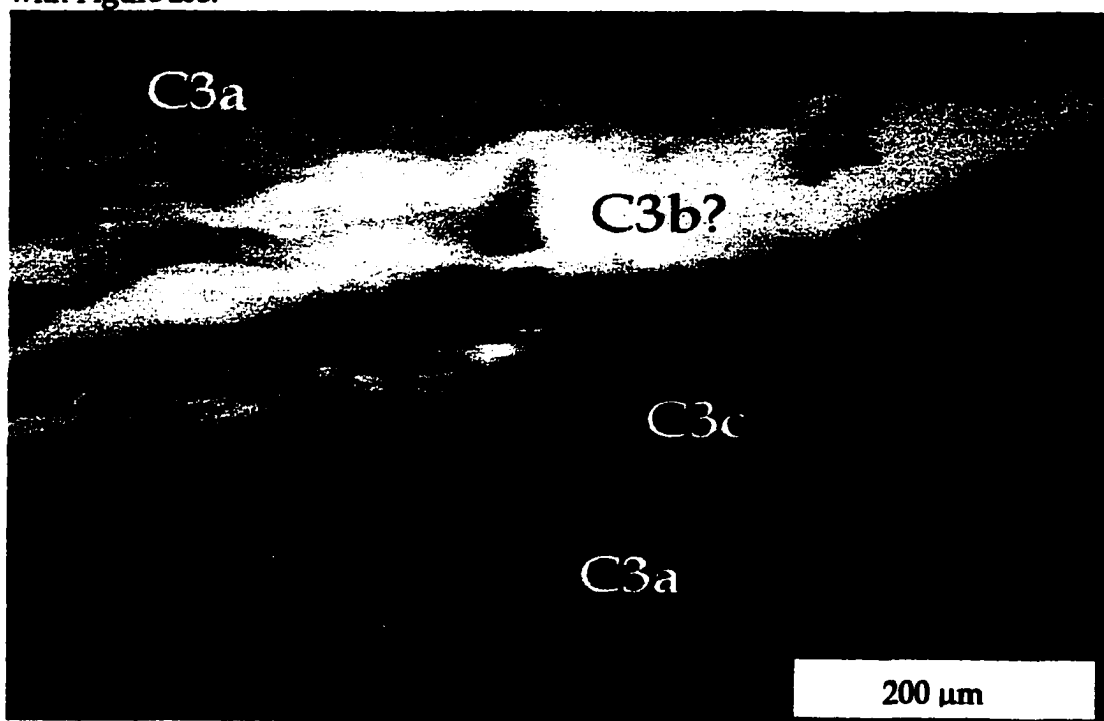


Figure 28b. Cathodoluminescence image of Figure 28a (rotated slightly counter-clockwise). Note the orientation of the dots used to relate Figures 28 a and b. Different intensities of luminescence are present in the different types of calcite within one late-ore stage calcite vein.

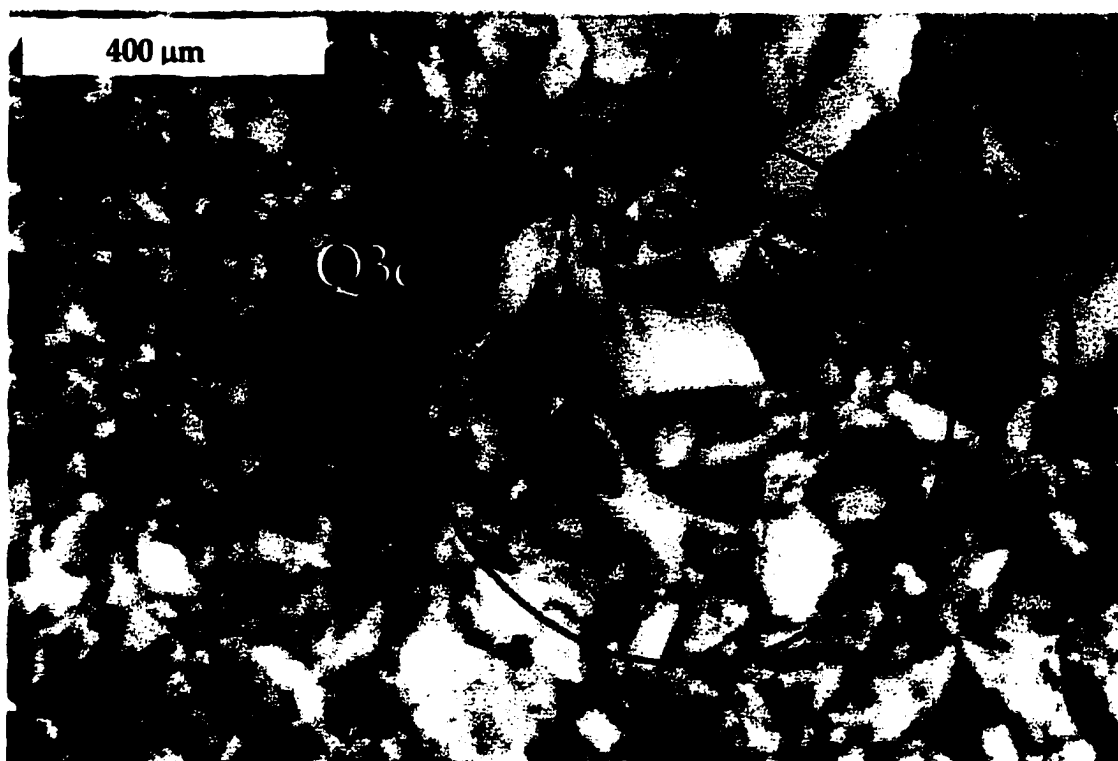


Figure 29. TL, CPL photomicrograph of Q3c chalcedony in thin section UC1079-4580-181.50-38-197.

were subsequently overgrown by other late-ore stage minerals including stibnite, orpiment, realgar, and calcite. These abundant hydrothermal minerals formed exclusively as open-space filling minerals, and are products of late-ore stage hydrothermal activity.

Marcasite (P3a and b) in the late-ore stage is morphologically distinct from all of the previous Fe-sulfide minerals, indicating changes in late-ore stage conditions as compared to ore-stage conditions. Chalcedony occurs locally within vugs and open spaces within the late-ore stage assemblage. The presence of chalcedony reflects formation in a low-temperature environment.

The variability of luminescence in different generations of quartz reflects



chemical variability of the quartz and shows that the different generations precipitated from chemically distinct fluids. Cathodoluminescence imagery of late-ore stage Q3b revealed oscillatory growth zones of different luminescent intensities within the euhedral crystals; the outermost growth zones were dark and non-luminescent.

The mechanisms that are responsible for the cathodoluminescence of hydrothermal quartz are among the least understood of all of the common minerals, and the impurities responsible for activating and quenching cathodoluminescence, if any, have not been identified with certainty (Marshall, 1988; Perny et al., 1992). Cathodoluminescence of lunar, plutonic, volcanic, diagenetic, metamorphic, and authigenetic quartz show that  $Mn^{4+}$ ,  $Cr^{3+}$ ,  $Pb^{2+}$ ,  $Al^{3+}$ ,  $Cu^{2+}$ ,  $Ti^{4+}$ , rare earth, and actinide elements may activate and enhance cathodoluminescence in quartz (Sprunt, 1981; Marshall, 1988). At the same time, studies by Marshall (1988), Bruhn (1995), and Hayward (1998) show that varying concentrations of quencher elements such as  $Fe^{2+}$ ,  $Ni^{2+}$ , and  $Co^{2+}$  can modify or inhibit the luminescence process. The concentrations and relative ratios of activators and quenchers necessary for the cathodoluminescence process in quartz are still unknown. Although color-spectral analyses were not conducted for the quartz in this study, this technique clearly would be useful in differentiating quartz stages.

Chemical oscillations in euhedral crystals of late-ore stage quartz are indicated by varying intensities of luminescence, suggesting that the crystal surfaces were exposed to continually evolving fluid compositions during growth. The presence of brightly luminescent zones in cores with non-luminescent rims suggests that fluid compositions were different when the cores and outer rims were precipitated. The varying cathodoluminescence in the observed quartz suggests that the precipitating

fluids for the late-ore stage Q2d quartz rims were either depleted in the elements that cause luminescence or contained concentrations of elements responsible for quenching cathodoluminescence.

Three types of late-ore calcite were observed as calcite bands within veins. The compositionally different bands of calcite suggest that there were either chemical changes within the system, or a late- or post-ore stage fracturing event occurred. The varying luminescence within the bands of the calcite veins suggests an evolving fluid chemistry.

## CHAPTER 6

### TRACE ELEMENT STUDY AND STATISTICAL EVALUATION

In order to determine major and trace element compositions of gold-bearing and gold-free Fe-sulfide minerals, twenty-two polished thin sections were analyzed using an electron microprobe. Major and trace element compositions of the Fe-sulfide minerals are listed in Appendix 5 and the detection limits are given in Appendix 3.

Concentrations of major elements Fe and S, and trace elements Pb, Co, Hg, Ag, Tl, Ni, As, Au, Cu, Sb, Zn and Mo were determined. EMP analyses and trace element maps were generated to provide information on zoning of major and trace elements in the Fe-sulfide minerals. The trace element suite was selected based on preliminary research on pyrite from Gatchell and pyrite that had formed under similar conditions in other deposits.

#### Pyrite Geochemistry

##### Pre-Ore Pyrite: P1a and P1b

Electron microprobe analyses (EMP) 1-50 of pre-ore Fe-sulfide minerals (Appendix 5) show that P1a and P1b pyrite contain the highest concentrations of Fe, S, and Pb, and low to nil Hg, Ag, Tl, Ni, As, Au, Cu, Sb, Zn and Mo (Table 5). P1a pyrite contains the highest average trace concentrations of Co, and the lowest average

**Table 5.** Average trace element geochemistry of pyrite determined by EMP. Pre-ore (P1a and b) and late-ore stage marcasite (P3) Fe-sulfide mineral groups contain near stoichiometric Fe and S, and trace or nil gold and ore-stage metals. Ore-stage pyrite/marcasite (P2a, b, c, and d) generally contains significant concentrations of the ore-stage trace elements Hg, Tl, As, Au, Cu, and Sb.

Average trace-elements in Fe-sulfide minerals at Getchell (wt%.)

Pyrite Type	Fe	S	Pb	Co	Hg	Ag	Tl	Ni	As	Au	Cu	Sb	Zn	Mo
P1a	45.612	54.307	0.216	0.076	0.005	0.000	0.038	0.007	0.000	0.002	0.002	0.000	0.002	0.000
P1b	45.796	54.144	0.202	0.049	0.013	0.008	0.035	0.053	0.083	0.006	0.011	0.004	0.019	0.013
P2a	40.309	49.132	0.099	0.041	0.747	0.023	0.746	0.018	6.721	0.097	0.265	0.759	0.008	0.031
P2b	36.033	46.821	0.000	0.057	1.047	0.000	1.004	0.194	9.301	0.075	0.316	1.461	0.000	0.000
P2c	36.923	45.811	0.034	0.041	0.637	0.054	1.253	0.005	13.735	0.298	0.648	0.538	0.004	0.000
P2d	44.453	52.913	0.184	0.055	0.044	0.015	0.050	0.065	1.454	0.012	0.073	0.100	0.002	0.000
P3	45.340	52.537	0.000	0.053	0.000	0.000	0.000	0.008	0.647	0.014	0.000	0.000	0.000	0.000

Stoichiometric Pyrite 46.550 53.450 0.000 0.000 0.000 0.000 0.000 0.000 0.000 0.000 0.000 0.000 0.000 0.000

concentrations of As and Au as compared to all other pyrite populations analyzed in this study. P1b pyrite contains elevated Ni as compared to P1a, and the highest average concentration of Zn in the study.

Ore-Stage Pyrite/Marcasite: P2a, P2b, P2c, and P2d

Electron microprobe analyses of P2a pyrite/marcasite indicate that the finely crystalline rims (analyses 51 to 69, Appendix 5) contain Fe and S concentrations that are less than stoichiometric. In addition, P2a pyrite/marcasite contains (1) decreased Pb, Co, and Ni, (2) elevated Ag and Mo, and (3) elevated concentrations of Hg, Tl, As, Au, Cu, and Sb as compared to pre-ore P1a and P1b pyrite (Table 5).

Owing to the small diameter of the P2b framboids, poor polish, and porous surface of this mineral, only three EMP analyses (70 to 72, Appendix 5) provided reasonably acceptable totals. P2b pyrite/marcasite contains significantly less than stoichiometric Fe and S, elevated concentrations of Hg, Tl, Ni, As, Au, Cu and Sb as compared to pre-ore pyrite, and nil Pb, Ag, Zn, and Mo. Au and As concentrations are high and average 750 ppm and 9.301 weight %, respectively (Table 5). P2b framboid-like Fe-sulfide minerals contained the lowest average Fe and Pb, and the highest average Hg, Ni, and Sb determined in the study.

EMP analyses of P2c subtle sulfide rims (analyses 73 to 79, Appendix 5) reveal slightly higher concentrations of Fe than P2b, elevated Pb, and the lowest concentrations of S, Co, and Ni determined for the pyrite populations analyzed. P2c pyrite/marcasite also contains low to nil Ni, Zn, and Mo, and exhibits the highest values and averages determined for As (13.735 average wt %), Au (2980 ppm), Ag, Tl, and Cu (Table 5). P2c pyrite/marcasite rims contain lower concentrations of Hg and Sb than P2a and P2b pyrite/marcasite. Additionally, pyrite/marcasite types P2a and P2c contained the

same low average concentrations of Co.

EMP analyses indicate that P2d Fe-sulfide minerals (analyses 81 to 142, Appendix 5) contain slightly less than stoichiometric concentrations of Fe and S and significantly less Au, As, Hg, Tl, and Sb than P2a, P2b, and P2c. Compared to P1b, P2d pyrite/marcasite contains concentrations of As, Cu, and Sb, slightly elevated Hg, Ag, Tl, Ni, and Au, and low Pb and Mo (Table 5). P2d pyrite/marcasite contains concentrations of Fe, S, Co, and Au similar to P3 marcasite.

#### Late-Ore Stage Marcasite: P3

Electron microprobe analyses (analyses 143 to 147, Appendix 5) indicate that P3 marcasite contains slightly less than stoichiometric Fe and S, and nil Pb, Hg, Ag, Tl, Cu, Sb, Zn, and Mo, and the lowest average concentrations of Hg, Cu, and Sb found in the study. P3 marcasite typically contains low As (0.647 average wt. %) and low Au (140 ppm) (Table 5). The trace element geochemistry of P3 marcasite is similar to pre-ore P1a and P1b pyrites except that P3 marcasite contains slightly elevated As and Au, and nil Pb and Hg.

#### **Pre-Ore and Ore-Stage Trace Element Maps**

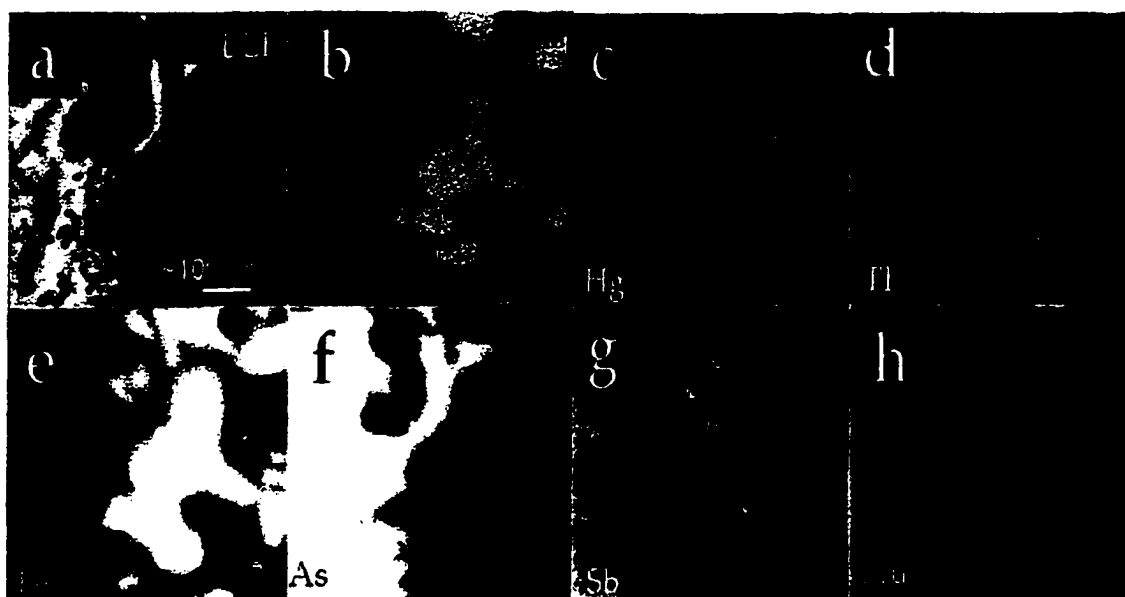
EMP maps of ore-stage pyrite crystals revealed rims enriched in Hg, Tl, As, Au, and Sb, and pyrite cores containing nil Hg, Tl, Ni, As, Au, Cu, and Sb (Figures 30 and 31). Figure 30 shows a backscatter electron image (BEI) of a P1a or b pyrite crystal, with P2a overgrowth rim and P2b framboid-like sulfide minerals in the surrounding jasperoid matrix. Note the high Fe and S concentrations (Figures 30 b and e) and the low concentrations of Hg, Tl, Ni, Sb, and As (Figure 30 c, d, f, g, and h, respectively) in P1a or b cores. Type P2a pyrite forms sharply defined rims on the P1a or b core sulfide.

The P2a pyrite/marcasite rim is approximately 2.5  $\mu\text{m}$  in width. Note the particularly sharp, bright P2a and P2b pyrite images produced by the As trace element map (Figure 30 h). Note the “dim” images for Fe and S in the rims of the pyrite, indicating a decrease in the Fe and S in the trace element-enriched rims as compared to the P1a or b trace element-poor cores (Figure 30 b and e). Ni is not elevated in either core or rim sulfides (Figure 30 f).

Figure 31 shows a BEI of a P1a or b pyrite crystal with a P2c subtle overgrowth rim, surrounded by jasperoid groundmass. The P2c rim on the pyrite is approximately 12  $\mu\text{m}$  in width. The enrichment of trace elements is evident in P2c rims that are brighter than the P1a or b cores in the maps of Hg, Tl, As, Sb and Au (Figure 31 c, d, f, g, and h). Note the “dim” rims of the pyrite highlighting decreases of Fe and S (Figure 31 b and e) as compared to the P1b trace element-poor cores. The bright region to the left of the rimmed pyrite in Figure 31 a-f is a realgar vein.



**Figure 30.** BEI and trace element maps of P1a or b and P2a and b Fe-sulfide minerals pictured in Figure 11b. The location of the transect in Figure 32 is shown as red line in a. Brightness and intensity in element maps b-h reflect the concentration of the trace elements: white = high concentration, black = nil to low concentration.

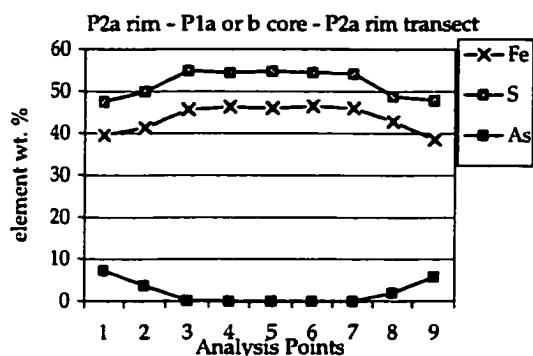
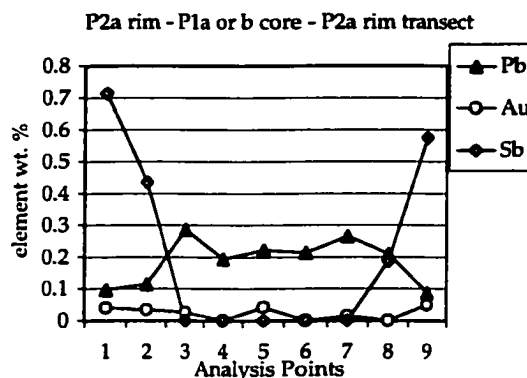


**Figure 31.** BEI and trace element map of types P1a or b and P2c Fe-sulfide minerals pictured in Figure 12. The location of the transect in Figure 32 is shown as red line in a. Brightness and intensity in element maps b-h reflect the concentration of the trace elements: white = high concentration, black = nil to low concentration.

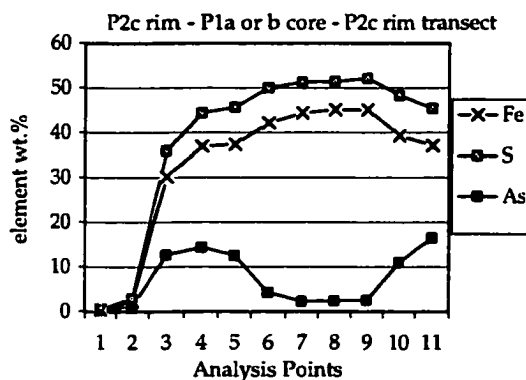
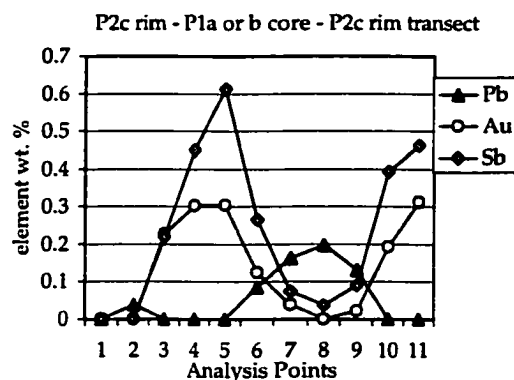
EMP data were collected along transects across the pyrite/marcasite crystals in Figures 30 and 31 (red lines on figures). Transects across pyrite crystals with ore-stage pyrite/marcasite rims further indicate the negative correlation between the ore-stage and non-ore stage trace elements (Figure 32, Table 6). Transects show that increased concentrations of ore-stage trace elements Hg, Tl, As, Au, Cu, and Sb in the rim-forming pyrite/marcasite are associated with reduced concentrations of Fe, S, and Pb. Analyses of pre-ore, non Au-bearing cores show low to nil concentrations of the ore-stage trace elements Hg, Tl, As, Au, Cu, and Sb and elevated concentrations of Fe, S, and Pb.



### Transect through P2a Pyrite Rims

**A****B**

### Transect through P2c Pyrite Rims

**C****D**

**Figure 32** -- Plots A-D show trace element transect data from Table 6. Location of transect for A and B is shown as a red line on Figure 30a. A and B show data for a transect through the P2a Au-rich rims (analysis points 1, 2 and 8, 9), and P1a or b Au-free cores (analysis points 3-7). Location of transect for C and D is shown as a red line on Figure 31a. C and D show data for a transect through P2c Au-rich rims (analysis points 3-5, and 10, 11), and P1a or b Au-free cores (analysis points 6-9). Transects A and C show the negative correlation of As to Fe and S. Transects B and D exhibit the negative correlation of Pb to Au and Sb.

**Table 6. EMP trace element transect data for Fe-sulfide minerals shown in Figures 30 and 31; the data for Fe, S, Pb, As, Au, and Sb are plotted in Figure 32.**

**Figure 30**

Transect – P2a rims	Fe	S	Pb	Co	Hg	Ag	Tl	Ni	As	Au	Cu	Sb	Zn	Mo	Total Wt. %
transect pt. 1	39.611	47.569	0.096	0.031	0.953	0.000	0.895	0.012	7.279	0.039	0.333	0.713	0.000	0.000	97.529
transect pt. 2	41.456	49.893	0.114	0.047	0.517	0.000	0.454	0.050	3.713	0.033	0.230	0.435	0.000	0.000	96.942
transect pt. 3	45.713	54.905	0.287	0.055	0.000	0.000	0.054	0.000	0.125	0.026	0.000	0.000	0.000	0.000	101.165
transect pt. 4	46.393	54.475	0.194	0.057	0.046	0.000	0.046	0.000	0.018	0.000	0.000	0.000	0.000	0.000	101.229
transect pt. 5	46.107	54.799	0.221	0.045	0.000	0.000	0.029	0.000	0.000	0.041	0.000	0.000	0.000	0.000	101.241
transect pt. 6	46.432	54.482	0.214	0.060	0.000	0.000	0.064	0.017	0.000	0.000	0.000	0.000	0.000	0.000	101.260
transect pt. 7	46.098	54.085	0.264	0.034	0.000	0.000	0.039	0.012	0.056	0.014	0.000	0.000	0.000	0.000	100.602

Due to porous surface texture of rims, EMP total wt.% for transect points 8 and 9 were less than 95% and are not shown, but were plotted in Figure 32.

**Figure 31**

Transect – P2c rims	Fe	S	Pb	Co	Hg	Ag	Tl	Ni	As	Au	Cu	Sb	Zn	Mo	Total Wt. %
transect pt. 1	36.877	44.379	0.000	0.039	0.505	0.000	1.008	0.000	14.408	0.302	0.595	0.450	0.000	0.000	98.563
transect pt. 2	37.272	45.647	0.000	0.034	0.726	0.000	1.314	0.000	12.539	0.303	0.729	0.612	0.000	0.000	99.176
transect pt. 4	44.424	51.212	0.162	0.044	0.000	0.000	0.085	0.000	2.184	0.038	0.094	0.074	0.000	0.000	98.317
transect pt. 5	45.101	51.405	0.198	0.056	0.000	0.000	0.049	0.000	2.448	0.000	0.039	0.037	0.000	0.000	99.333
transect pt. 6	45.037	52.143	0.131	0.045	0.000	0.000	0.000	0.000	2.474	0.022	0.049	0.090	0.000	0.000	99.991
transect pt. 7	39.237	48.259	0.000	0.046	0.506	0.000	1.064	0.000	11.037	0.193	0.554	0.392	0.012	0.000	101.300
transect pt. 8	37.080	45.405	0.000	0.022	0.507	0.172	1.183	0.000	16.433	0.313	0.649	0.461	0.000	0.000	102.225

Due to porous surface texture of rims, EMP total wt.% for transect points 3, 9, 10 and 11 were less than 95% and are not shown, but were plotted in Figure 32.

## Discussion of Trace Element Analyses

Quantitative EMP analyses distinguished seven populations of pyrite that have differences in major and minor trace element compositions. All analyses show that Ag, Zn, and Mo are generally low or non-detectable, and these elements will not be discussed further.

Pre-ore Fe-sulfide minerals P1a and P1b, hosted by sedimentary and igneous rocks, respectively, exhibit nearly identical major and trace-metal compositions. These non Au-bearing pyrites contain near stoichiometric Fe and S concentrations, low but measurable concentrations of Co, Pb, and Ni, and trace or nil Hg, Tl, As, Au, Cu, and Sb. EMP analysis identified four populations of ore-stage Fe-sulfide minerals, three of which contain significant Au. Ore-stage pyrite/ marcasite P2a, P2b, and P2c contain lower concentrations of Fe, S, Co, and Pb than pre-ore pyrites, and significantly elevated concentrations of Tl, As, Hg, Au, Cu, and Sb, which will be referred to as ore-stage elements. P2d pyrite/ marcasite contains slightly higher concentrations of Hg, Tl, As, Au, Cu, and Sb than the pre-ore pyrites, but lower concentrations of these elements than P2a, P2b, and P2c pyrite/ marcasite. P2d is included in the ore-stage paragenesis based on (1) its presence in jasperoid quartz, (2) its less than stoichiometric average concentrations of Fe and S, and (3) its elevated concentrations of As.

Analyses of late-ore stage P3 marcasite show that this mineral contains trace element concentrations somewhat similar to those of pre-ore stage P1a and P1b. Although P3 marcasite contains elevated As, the late-ore marcasite contains none of the other ore-stage elements. P3 marcasite is also enclosed by late-ore calcite, and is not spatially associated with other Fe-sulfide minerals.

## Statistical Analysis of Sulfide Geochemistry

Quantitative EMP analyses of major elements Fe and S and trace elements Pb, Co, Hg, Ag, Tl, Ni, As, Au, Cu, Sb, Zn, and Mo were evaluated using statistical methods. One hundred ninety-seven data points in Appendix 5 were used to generate correlation matrices and principal components data. Positive and negative correlations between the trace elements in this study are indicated by correlation coefficients of  $r = \geq 0.5$  and  $\leq -0.5$ , respectively. Significant positive or negative correlations are those with correlation coefficients of  $r = \geq 0.7$  and  $\leq -0.7$ , respectively.

Analyses of seven P1a pyrites show that Fe correlates positively with S and Co (Tables 7 and 8). No elements in P1b correlate either positively or negatively (Tables 7 and 8). Due to the low total number of analyzed points for P2b pyrite/marcasite, P2a, P2b, and P2c pyrite/marcasite were evaluated as a group (Tables 7 and 9). Statistical analysis of the geochemical data for the thirty-seven analyses of Au- and As-bearing P2a, P2b, and P2c Fe-sulfide minerals indicate that there is a positive correlation for Fe with Pb and a significant positive correlation for Fe with S ( $r = 0.864$ ) (Figure 33) and Co with Ni ( $r = 0.819$ ) (Tables 7 and 9). There is a negative correlation between As with S ( $r = -0.610$ ) (Figure 33). Fe is negatively correlated with ore-stage Tl and Cu (Tables 7 and 9), and Fe exhibits significant negative correlation with As ( $r = -0.704$ ) (Table 7, 9 and Figure 34a). Ore-stage elements As, Au, Cu, and Tl show a positive correlation with one another (As with Au,  $r = 0.749$ ; As with Cu,  $r = 0.768$ ; Au with Cu,  $r = 0.733$ ; and As with Tl,  $r = 0.563$ ) (Table 9), and there is significant positive correlation between Hg with Tl ( $r = 0.774$ ) (Figure 34b), and Cu with Tl ( $r = 0.775$ ) (Figure 34b).

Elements in P2d Fe-sulfide minerals show positive correlation for Hg with Sb ( $r = 0.693$ ) (Figure 35), Tl with Sb ( $r = 0.679$ ), As with Au ( $r = 0.523$ ) (Tables 7 and 10),

Table 7. Table illustrating trace element correlations  $r \geq 0.5$  and  $\leq -0.5$ . Correlation values of  $r \geq 0.7$  and  $\leq -0.7$  are underlined. X = correlation with  $r \leq 0.5$ , or  $\geq -0.5$ .

Stage 1: Pre-Ore		Major Elements		Ore-Stage Trace elements						Non-Ore Stage Trace elements					
		Fe	S	Hg	Tl	As	Au	Cu	Sb	Pb	Co	Ag	Ni	Zn	Mo
Type P1a	Positive correlation $r \geq 0.5$	<u>S</u> , Co	<u>Fe</u>	X	X	X	X	X	X	X	Fe	X	X	X	X
	Negative correlation $r \leq -0.5$	X	X	X	X	X	X	X	X	X	X	X	X	X	X
Type P1b	Positive correlation $r \geq 0.5$	X	X	X	X	X	X	X	X	X	X	X	X	X	X
	Negative correlation $r \leq -0.5$	X	X	X	X	X	X	X	X	X	X	X	X	X	X

Stage 2: Ore-Stage															
Types															
P2 a, b, and c	Positive correlation $r \geq 0.5$	<u>S</u> , Pb	<u>Fe</u>	<u>Tl</u>	<u>As, Cu, Hg</u>	<u>Au, Cu, Tl</u>	<u>Cu, As</u>	<u>Tl, As, Au</u>	X	Fe	<u>Ni</u>	X	<u>Co</u>	X	X
	Negative correlation $r \leq -0.5$	Tl, <u>As, Cu</u>	As	X	Fe	<u>Fe, S</u>	X	Fe	X	X	X	X	X	X	X
Type P2d	Positive correlation $r \geq 0.5$	X	X	<u>Tl, Sb</u>	<u>Sb, Hg</u>	<u>Au, Sb</u>	<u>Sb, As</u>	X	<u>Hg, Tl, As, Au</u>	X	X	X	X	X	X
	Negative correlation $r \leq -0.5$	X	X	X	X	X	X	X	X	X	X	X	X	X	X

Stage 3: Late-Ore															
Type P3															
	Positive correlation $r \geq 0.5$	X	X	X	X	<u>Au</u>	<u>As</u>	X	X	X	Ni	X	Co	X	X
	Negative correlation $r \leq -0.5$	Co	<u>Au, As</u>	X	X	<u>S</u>	<u>S, Co</u>	X	X	X	<u>Fe, Au</u>	X	X	X	X

Table 8. Trace element correlation matrices for P1a and P1b pyrite.

P1a	Fe	S	Pb	Co	Hg	Ag	Tl	Ni	As	Au	Cu	Sb	Zn	Mo
Fe	1.000													
S	0.750	1.000												
Pb	0.143	-0.290	1.000											
Co	0.615	0.387	-0.173	1.000										
Hg	ND	ND	ND	ND	1.000									
Ag	0.000	0.000	0.000	0.000	0.000	1.000								
Tl	ND	ND	ND	ND	ND	0.000	1.000							
Ni	ND	ND	ND	ND	ND	0.000	ND	1.000						
As	0.000	0.000	0.000	0.000	0.000	0.000	0.000	0.000	1.000					
Au	ND	ND	ND	ND	ND	0.000	ND	ND	0.000	1.000				
Cu	ND	ND	ND	ND	ND	0.000	ND	ND	0.000	ND	1.000			
Sb	0.000	0.000	0.000	0.000	0.000	0.000	0.000	0.000	0.000	0.000	0.000	1.000		
Zn	ND	ND	ND	ND	ND	0.000	ND	ND	0.000	ND	ND	0.000	1.000	
Mo	0.000	0.000	0.000	0.000	0.000	0.000	0.000	0.000	0.000	0.000	0.000	0.000	0.000	1.000

P1b	Fe	S	Pb	Co	Hg	Ag	Tl	Ni	As	Au	Cu	Sb	Zn	Mo
Fe % ele	1.000													
S	0.338	1.000												
Pb	-0.035	0.089	1.000											
Co	0.142	0.149	0.226	1.000										
Hg	ND	ND	ND	ND	1.000									
Ag	ND	ND	ND	ND	ND	1.000								
Tl	0.092	0.034	0.019	-0.101	-0.101	-0.082	1.000							
Ni	0.020	-0.008	0.050	0.235	0.059	-0.066	-0.065	1.000						
As	-0.028	0.071	-0.150	0.154	-0.161	0.087	0.037	0.055	1.000					
Au	ND	ND	ND	ND	ND	ND	ND	ND	ND	1.000				
Cu	ND	ND	ND	ND	ND	ND	ND	ND	ND	ND	1.000			
Sb	ND	ND	ND	ND	ND	ND	ND	ND	ND	ND	ND	1.000		
Zn	ND	ND	ND	ND	ND	ND	ND	ND	ND	ND	ND	ND	1.000	
Mo	ND	ND	ND	ND	ND	ND	ND	ND	ND	ND	ND	ND	ND	1.000

Significant correlation coefficient of  $r = \geq 0.7$  or  $\leq -0.7$

Correlation coefficient of  $r = \geq 0.5$  or  $\leq -0.5$

ND = Not enough data available for valid correlation coefficient to be determined.

Table 9. Trace element correlation matrix for P2a, P2b, and P2c pyrite/marcasite.

P2a-c	Fe	S	Pb	Co	Hg	Ag	Tl	Ni	As	Au	Cu	Sb	Zn	Mo
Fe	1.000													
S	0.864	1.000												
Pb	0.529	0.443	1.000											
Co	-0.031	0.125	0.252	1.000										
Hg	-0.349	-0.095	-0.123	0.208	1.000									
Ag	ND	ND	ND	ND	ND	1.000								
Tl	0.571	-0.330	-0.227	0.195	0.774	ND	1.000							
Ni	-0.192	-0.016	-0.039	0.819	0.174	ND	0.112	1.000						
As	0.704	0.610	-0.441	0.019	0.211	ND	0.653	0.067	1.000					
Au	-0.407	-0.370	-0.093	-0.045	-0.169	ND	0.374	-0.142	0.749	1.000				
Cu	0.533	-0.328	-0.263	0.087	0.294	ND	0.775	-0.014	0.768	0.733	1.000			
Sb	-0.219	-0.072	-0.102	0.083	0.355	ND	0.139	0.076	0.096	0.118	-0.011	1.000		
Zn	ND	ND	ND	ND	ND	ND	ND	ND	ND	ND	ND	ND	1.000	
Mo	ND	ND	ND	ND	ND	ND	ND	ND	ND	ND	ND	ND	ND	1.000

 Significant correlation coefficient of  $r = \geq 0.7$  or  $\leq -0.7$

 Correlation coefficient of  $r = \geq 0.5$  or  $\leq -0.5$

ND = Not enough data available for valid correlation coefficient to be determined.

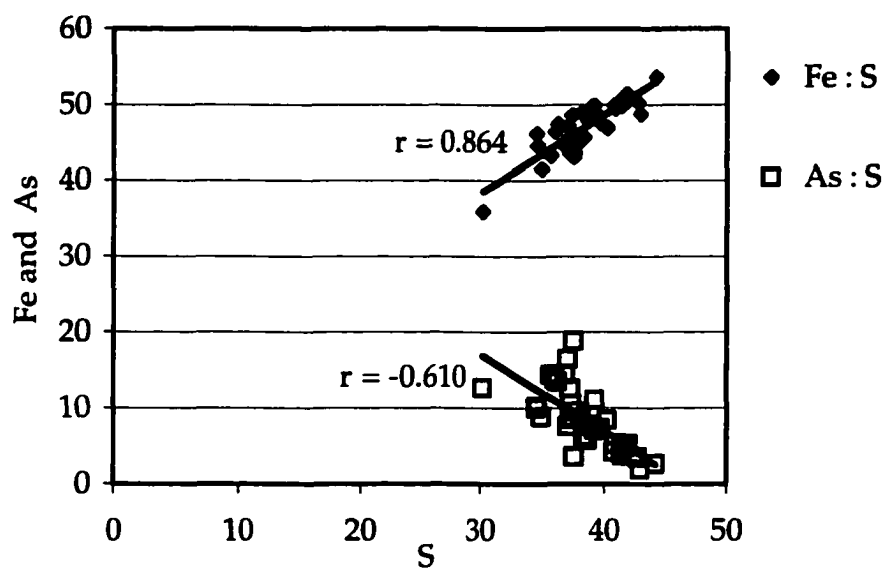


**Figure 33.**

Trace and major element linear regression plots for P2a, b, and c ore-stage pyrite/marcasite. This graph shows the negative correlation between As and S, and the significant positive correlation between Fe and S.



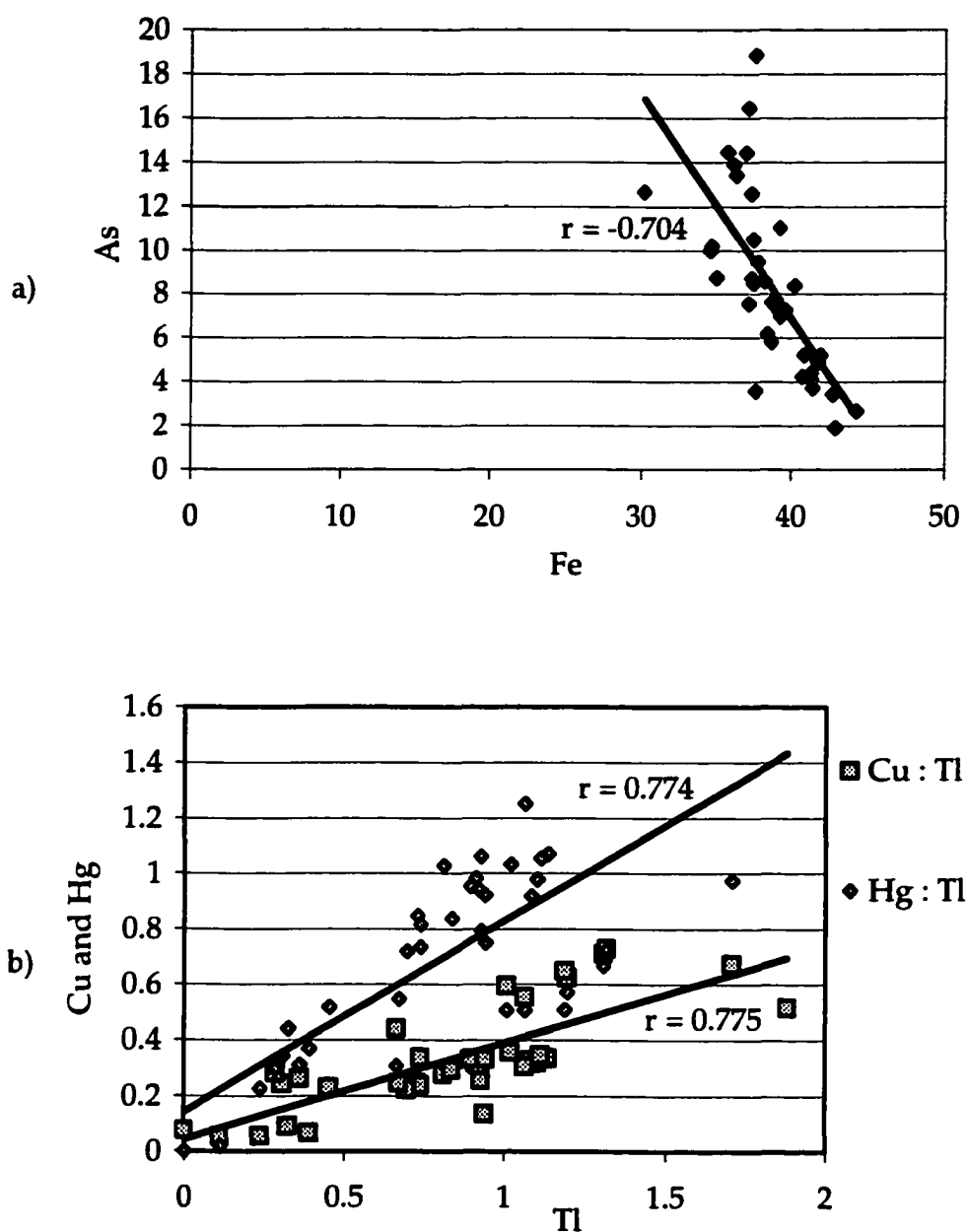


**Figure 34.** Trace element linear regression plots for P2a, b, and c ore-stage pyrite/marcasite. (34a) Fe and As show a significant negative correlation. (34b) Tl shows a significant positive correlation with both Cu and Hg.

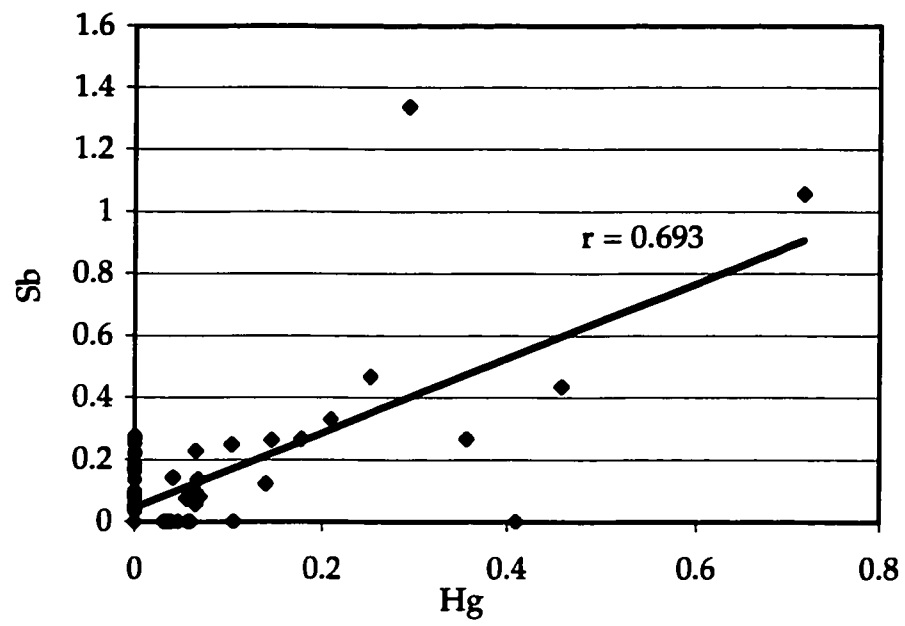


Figure 35. Trace element linear regression plot for P2d pyrite/marcasite. This graph shows the positive correlation between Sb and Hg.

Table 10. Trace element correlation matrix for P2d pyrite/marcasite.

P2d	Fe	S	Pb	Co	Hg	Ag	Tl	Ni	As	Au	Cu	Sb	Zn	Mo
Fe	1.000													
S	0.309	1.000												
Pb	0.235	0.052	1.000											
Co	0.114	0.084	-0.162	1.000										
Hg	-0.299	-0.326	-0.179	-0.067	1.000									
Ag	ND	ND	ND	ND	ND	1.000								
Tl	-0.329	-0.281	-0.218	-0.032	0.706	ND	1.000							
Ni	-0.013	-0.054	0.217	0.450	0.036	ND	0.044	1.000						
As	-0.242	-0.421	0.061	-0.225	0.464	ND	0.424	-0.022	1.000					
Au	-0.207	-0.248	-0.135	-0.086	0.359	ND	0.346	-0.107	0.523	1.000				
Cu	-0.269	-0.185	0.022	-0.172	0.398	ND	0.209	-0.143	0.365	0.211	1.000			
Sb	-0.322	-0.433	-0.101	-0.150	0.693	ND	0.679	-0.070	0.598	0.523	0.436	1.000		
Zn	ND	ND	ND	ND	ND	ND	ND	ND	ND	ND	ND	ND	1.000	
Mo	ND	ND	ND	ND	ND	ND	ND	ND	ND	ND	ND	ND	ND	1.000

 Significant correlation coefficient of  $r = \geq 0.7$  or  $\leq -0.7$

 Correlation coefficient of  $r = \geq 0.5$  or  $\leq -0.5$

ND = Not enough data available for valid correlation coefficient to be determined.

As with Sb ( $r = 0.698$ ) (Figure 36), Au with Sb ( $r = 0.528$ ) (Table 10), and significant positive correlation for Hg with Tl ( $r = 0.706$ ) (Tables 7, 10, and Figure 37).

Statistical analysis of data for P3 marcasite indicates a positive correlation between non-ore elements Ni and Co, and a significant positive correlation between ore-stage elements As and Au ( $r = 0.710$ ) (Tables 7 and 11). A significant negative correlation is indicated between S and As ( $r = -0.845$ ) (Figure 38a), S and Au ( $r = -0.724$ ), and Au and Co ( $r = -0.778$ ) (Figure 38b), and a negative correlation is indicated between Fe and Co ( $r = -0.661$ ) (Table 11).

## Conclusions

Statistical analyses of elemental concentrations distinguish ore-stage Fe-sulfide minerals from pre- and late-ore stage Fe-sulfide minerals, and further distinguish ore-stage trace elements from pre- and late-ore stage trace element compositions. Statistical analyses of pre-ore Fe-sulfide minerals revealed no significant positive or negative correlation between the trace elements. Conversely, P2a, P2b, and P2c pyrites exhibit a positive correlation for Tl with As, and significantly positive correlations for Tl with Hg and Cu, As with Au and Cu, and Au with Cu. Additionally, significant positive correlations were indicated for the non-ore elements Fe with S, and Co with Ni. Sb did not correlate with any of the trace metals in the P2a, P2b, and P2c Fe-sulfide minerals. A significant negative correlation is indicated for As with Fe; a negative correlation is indicated for As with S. The positive correlation for Fe with S and Pb, the negative correlation of Fe with Cu and Tl, the negative correlation of S with As, and the significant negative correlation of Fe with As all reflect the observed decrease in concentrations of Fe and S and the increase in ore-stage element concentrations.

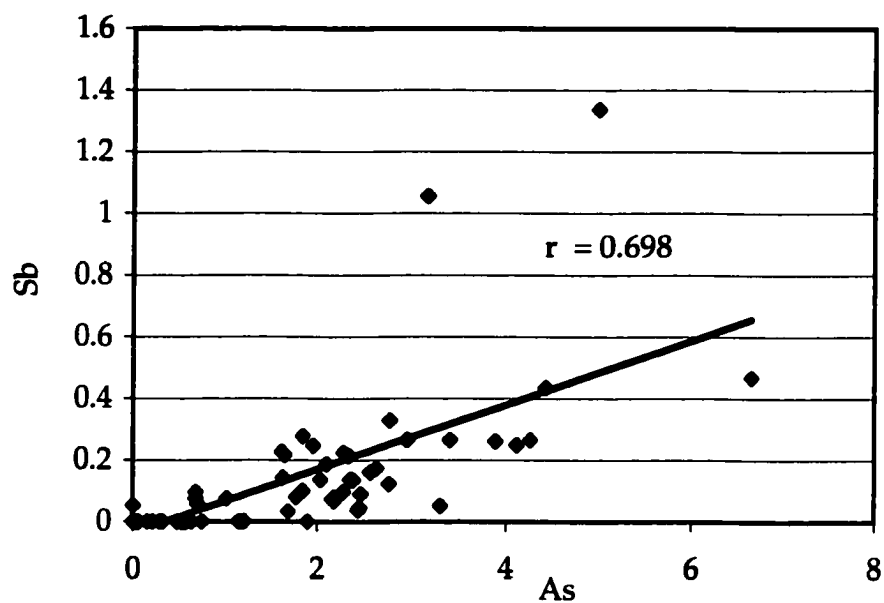


**Figure 36.** Trace element linear regression plot for P2d pyrite/marcasite. This graph shows the positive correlation between As and Sb.

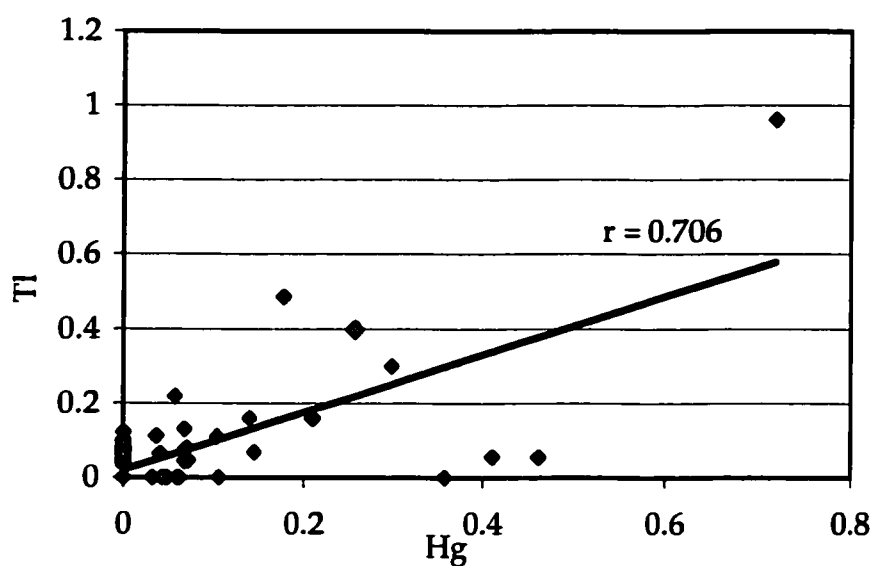


**Figure 37.** Trace element linear regression plot for P2d pyrite/marcasite. This graph shows the significant positive correlation between Hg and Tl.

Table 11. Trace element correlation matrix for P3 marcasite.

P3	Fe	S	Pb	Co	Hg	Ag	Tl	Ni	As	Au	Cu	Sb	Zn	Mo
Fe	1.000													
S	-0.431	1.000												
Pb	0.000	0.000	1.000											
Co	0.561	0.241	0.000	1.000										
Hg	0.000	0.000	0.000	0.000	1.000									
Ag	0.000	0.000	0.000	0.000	0.000	1.000								
Tl	0.000	0.000	0.000	0.000	0.000	0.000	1.000							
Ni	-0.158	-0.218	0.000	0.517	0.000	0.000	0.000	1.000						
As	0.045	0.645	0.000	-0.168	0.000	0.000	0.000	0.194	1.000					
Au	0.481	0.724	0.000	0.278	0.000	0.000	0.000	-0.330	0.710	1.000				
Cu	0.000	0.000	0.000	0.000	0.000	0.000	0.000	0.000	0.000	0.000	1.000			
Sb	0.000	0.000	0.000	0.000	0.000	0.000	0.000	0.000	0.000	0.000	0.000	1.000		
Zn	0.000	0.000	0.000	0.000	0.000	0.000	0.000	0.000	0.000	0.000	0.000	0.000	1.000	
Mo	0.000	0.000	0.000	0.000	0.000	0.000	0.000	0.000	0.000	0.000	0.000	0.000	0.000	1.000

 Significant correlation coefficient of  $r = \geq 0.7$  or  $\leq -0.7$

 Correlation coefficient of  $r = \geq 0.5$  or  $\leq -0.5$

ND = Not enough data available for valid correlation coefficient to be determined.

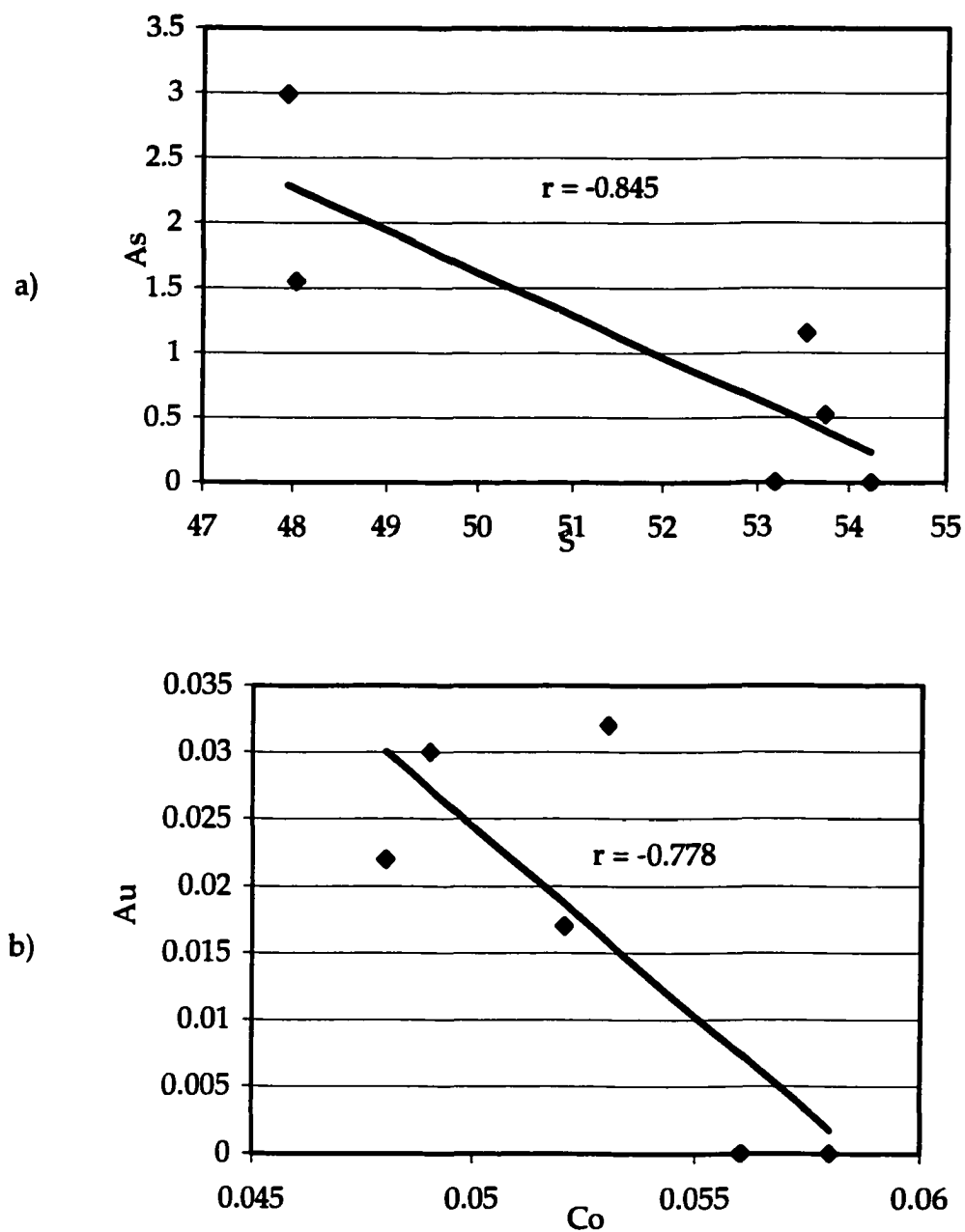


**Figure 38.** Trace element linear regression plots for P3 marcasite. (38a) As and S show significant negative correlation. (38b) Au and Co show significant negative correlation.



P2d ore-stage pyrite/marcasite shows a positive correlation for ore-stage elements Sb with Hg, Tl, As, and Au; Au with As; and Tl with Hg. Cu does not correlate with any of the trace metals. The correlation between the ore-stage elements was not as significant in P2d as in P2a, P2b, and P2c pyrite/marcasite.

P3 late-ore marcasite contains elevated concentrations of As and trace amounts of Au, but lower concentrations of other ore-stage elements. There is a significant positive correlation for As with Au, and a negative correlation for Fe with Co. Additionally, P3 shows a significant negative correlation for S with As and Au; the negative correlation between S and As is similar to P2a, P2b, and P2c; however, there is no statistical correlation between any of the other ore-stage elements.

#### CLUSTER ANALYSIS OF SULFIDE GEOCHEMISTRY

Further statistical analyses of the geochemical data using K-means clustering (Appendix 6) (STATISTICA for Windows, 1995) quantitatively distinguished two groups of Fe-sulfide minerals. K-means cluster analysis of the EMP trace element data distinguished non ore-stage P1a and P1b pyrites and P3 marcasite from the P2a, P2b, P2c, and P2d gold-bearing ore-stage Fe-sulfide minerals. The mean standardized concentrations of each element for the two groups are shown in Figure 39. Mean standardized concentrations are calculated by first subtracting the mean from each variable and then dividing by the standard deviation of the variable. Near or below mean concentrations of the elements Hg, Tl, As, Au, Cu and Sb, and near or above mean

concentrations of Fe, S, Pb, and Co are present in non ore-stage pyrite (Figure 39).

Conversely, above mean concentrations of the elements Hg, Tl, As, Au, Cu, and Sb, and below mean concentrations of Fe, S, Pb, and Co exist for ore-stage pyrite/marcasite (Figure 39).

The statistical analyses of trace elements in non-ore and ore-bearing Fe-sulfide minerals show that: (1) two different groups of Fe-sulfide minerals are distinguished by trace element composition, and (2) non-ore-bearing and ore-bearing groups identified using petrography can also be identified using statistical analyses of EMP data.

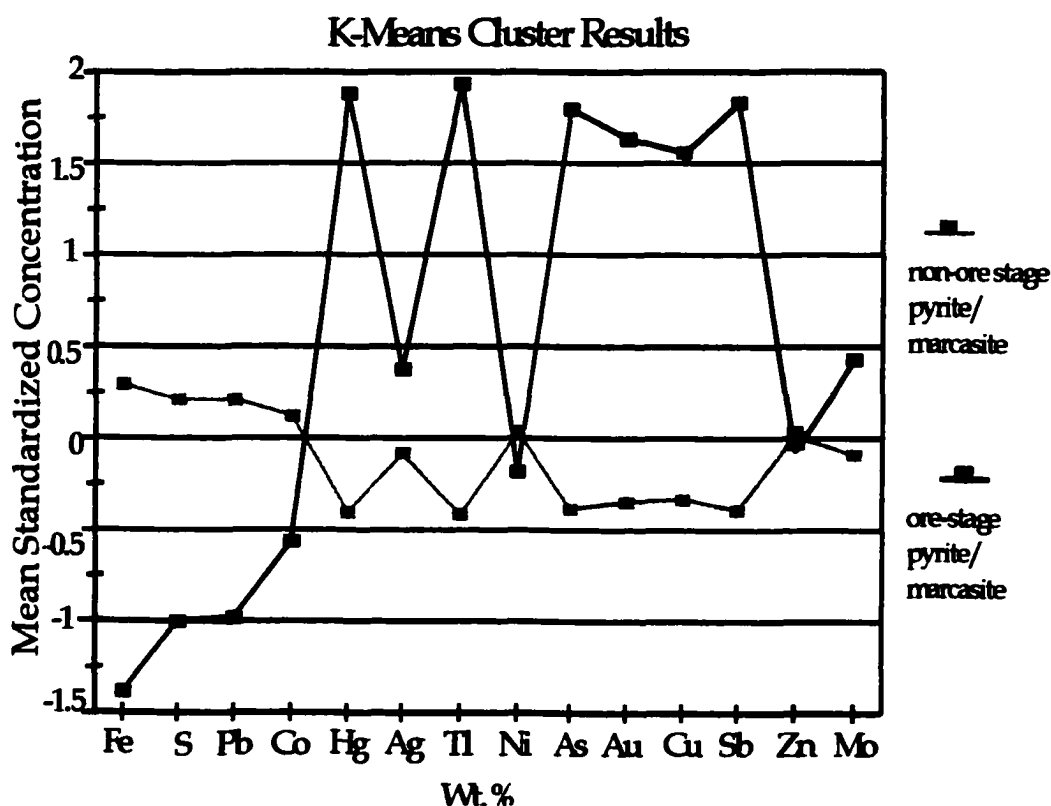


Figure 39. Mean standardized concentrations of non-ore stage and ore-stage Fe-sulfide minerals.

## CHAPTER 7

### GOLD QUANTIFICATION AND LOCATION

#### SIMS Analyses

Five samples were analyzed using secondary ion mass spectrometry (SIMS) to further quantify submicroscopic gold and arsenic in Fe-sulfide minerals and realgar. Quantitative analyses and trace element maps generated through SIMS microanalysis provided information on zoning of  $^{34}\text{S}$ ,  $^{75}\text{As}$  and  $^{197}\text{Au}$  in sulfide minerals. SIMS analyses have significantly lower detection limits than EMP analyses, but a larger spot size is analyzed and spatial resolution is reduced. The five samples were selected so that all populations of Fe-sulfide minerals observed in this study were evaluated. SIMS data are listed in Table 12.

SIMS analyses of pre-ore stage, coarse pyrite crystals revealed low concentrations of As (16.95 average ppm) and trace Au (2.67 average ppm) (Table 12). Analyses of fine crystals of aggregated, disseminated, and rim-forming P2a, P2b, and P2c Fe-sulfide minerals indicate significantly elevated average concentrations of As (691.60 ppm) and Au (698.53 ppm) (Table 12). Additionally, analyses of large, porous, P2d Fe-sulfide mineral crystals (Table 12) indicated relatively low average concentrations of As (126.31 ppm) and Au (58.46 ppm). SIMS analyses of late-ore stage marcasite average 78.23 ppm As and 52.38 ppm Au (Table 12).

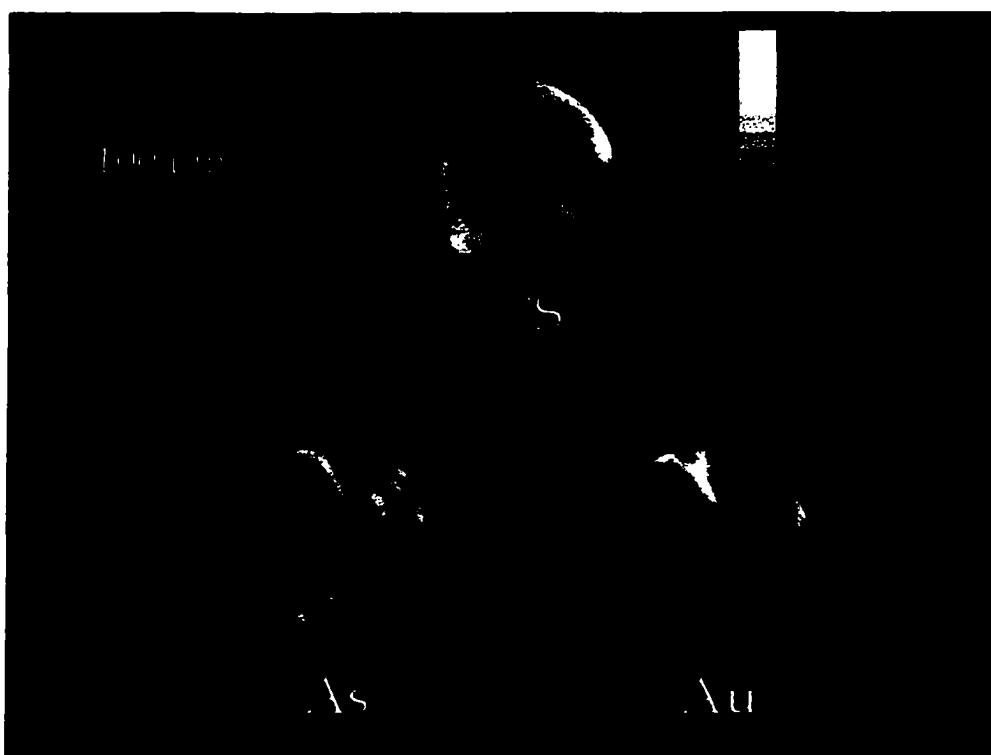
Pre-ore stage (P1a and P1b) Coarse/euhedral pyrite	Analysis #	As (ppm)	Au (ppm)		
	3	30	0.69		
	4	47	0.44		
	11	5.7	13		
	14	1.6	0.78		
	18	0.39	0.43		
	45	17	0.69	Average	As (ppm) Au (ppm) 16.95 2.67
Ore-stage (P2a, b, and c) Fine-grained pyrite/marcasite	30	20	78		
	31	87	91		
	10	1100	1100		
	32	760	550		
	33	840	340		
	34	2500	2500		
	38	1500	2300		
	12	16	2.3		
	13	93	24		
	46	110	17	Average	As (ppm) Au (ppm) 691.60 698.53
Ore-stage (P2d) Porous pyrite/marcasite masses	41	11	11		
	42	36	43		
	22	0.48	0.34		
	23	0.95	0.5		
	35	53	7.2		
	40	140	2.2		
	24	0.84	0.62		
	27	21	11		
	43	74	45		
	44	56	5		
	47	74	19		
	17	120	290		
	5	240	41		
	6	280	42		
	7	310	16		
	1	330	120		
	2	400	340	Average	As (ppm) Au (ppm) 126.31 58.46
Late-ore stage (P3) Marcasite	15	41	170		
	16	200	320		
	20	1.4	0.47		
	21	4.5	1.9		
	26	63	25		
	29	0.21	0.24		
	36	78	1.6		
	37	8	1.3		
	19	6.2	2.2		
	25	380	1.1	Average	As (ppm) Au (ppm) 78.23 52.38
Realgar	8		0.23		
	8		0.27		
	28		35		
	39		556	Average	Au (ppm) 147.88

Table 12. SIMS analyses of pre-ore and ore-stage Fe-sulfide minerals and realgar.

SIMS analyses 1-8 are from section UC1075-4655-164.00-06-86; analyses 10-22 are from section UC1079-4850-181.50-38-197; analyses 23-33 are from section UC0606-5000-184.00-15-159; analyses 34-39 are from section UC1084-4850-181.50-41-197; and analyses 41-47 are from section UC0519-4850-173.50-15-62.

## SIMS Ion Mapping

The associations between As, Au, and S in the ore-stage pyrite as indicated by the statistical analyses are confirmed by SIMS ion probe maps of sulfur ( $^{34}\text{S}$ ), arsenic ( $^{75}\text{As}$ ), and gold ( $^{197}\text{Au}$ ) (Figure 40). These maps indicate: (1) elevated concentrations of arsenic and gold in the ore-stage Fe-sulfide minerals and, (2) significant positive correlation between Au and As, and a negative correlation between those elements and S.



**Figure 40.** SIMS map of sample UC1079-4850-181.50-38-197 showing location and relative concentrations of sulfur ( $^{34}\text{S}$ ), arsenic ( $^{75}\text{As}$ ), and gold ( $^{197}\text{Au}$ ) within a Fe-sulfide crystal. These images demonstrate the significant positive correlation between Au and As in the sulfide mineral, and the poor to negative correlation between those elements and S. Color bar represents reflects relative concentrations of  $^{34}\text{S}$ ,  $^{75}\text{As}$ , and  $^{197}\text{Au}$ : dark red = low to nil concentration, white = high concentration.

## **SIMS Depth Profiling**

SIMS depth profile analyses were conducted to determine if gold is present in the ore-stage Fe-sulfides as colloids or in solid solution. Au in solid solution in the pyrite would not exhibit a change in intensity with depth profiling, thus producing a flat line. Conversely, individual clusters of colloidal gold particles can be detected and are shown by sharp peaks in intensity. One analysis of a realgar vein (R3) yielded 556 ppm of colloidal Au ( $<1\ \mu\text{m}$ ) (Figure 41a; analysis 39, Table 12). Depth profile analyses of finely crystalline Fe-sulfide minerals did not detect colloidal Au, and indicate that gold is in solid solution and uniformly distributed throughout the finely textured crystals of Fe-sulfide mineral (Figure 41b; analyses 31, Table 12).

## **SIMS Discussion**

SIMS analyses document trace gold and arsenic in the coarse, euhedral pre-ore pyrite. The presence of trace Au and As in these pyrites may have resulted from: (1) inclusions in the pre-ore pyrite of finely crystalline, ore-stage Fe-sulfide minerals that contain gold and arsenic, (2) the large radius of the ionic beam ( $20\ \mu\text{m}$ ) may have led to the inadvertent inclusion of neighboring ore-stage minerals in the analysis, or (3) trace gold may be present in these pyrites.

Analyses quantified volumetrically significant gold in finely crystalline Fe-sulfide minerals that form rims and framboid-like crystals, often showing Au:As at 1:1. The porous P2d Fe-sulfide minerals contained higher concentrations of arsenic than

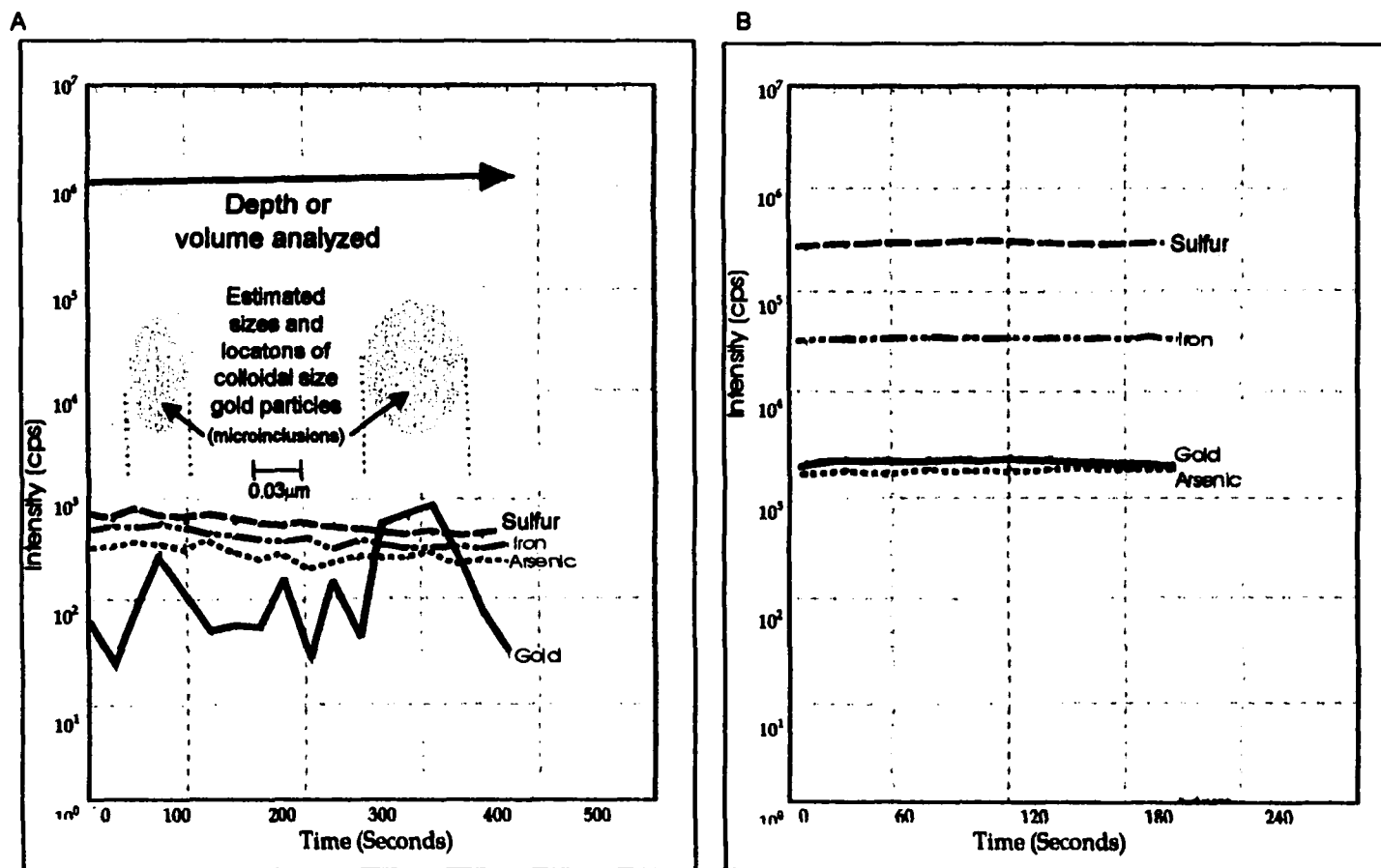


Figure 41. SIMS depth profiles of sample UC1084-4850-181.50-41-197. (A) Depth profile of SIMS spot analyses of a realgar vein illustrating the presence of colloidal-sized gold microinclusions, shown by variations in intensity. (B) Depth profile of SIMS spot analyses of a fine-grained ore-stage pyrite illustrating solid solution gold, shown by stable intensity levels. The gold concentration in this sample is 91 ppm, the arsenic concentration is 87 ppm. Counts per second = (cps).

gold. Late-ore marcasite contains elevated As and Au values as compared to coarse, euhedral, pre-ore pyrite crystals, and lower As than P2d pyrite/marcasite.

SIMS analyses and ion mapping confirmed the significant positive correlation between As and Au in the ore-stage Fe-sulfide minerals. The SIMS image shows that arsenic and gold are concentrated in the ore-stage Fe-sulfide mineral. Additionally, the image and analyses show that the concentrations of As and Au are directly correlated, and correlate negatively with S. The negative correlation of As and S in the sulfide mineral crystal lattice eliminates the possibility that the As is native arsenic (Radtko, 1985; Rytuba, 1985)

The failure of SIMS depth profiling to detect Au microinclusions in finely crystalline, ore-stage Fe-sulfide minerals and the consistent concentration of Au with increased As suggests that gold occurs in solid solution within the ore-stage Fe-sulfide minerals, and that an increase in Au is facilitated by an increase in As. Colloidal-sized microinclusions of gold in realgar probably occur because the crystal structure of realgar will not readily accept Au: as a result, Au present in the system is forced to precipitate as Au microinclusions in realgar (Chrysosoulis, pers. comm., 1999).

## LOCATION OF GOLD

### TEM Analysis

Preliminary high-resolution transmission electron microscopy (HRTEM) analyses were conducted to identify the structure and the type of Au-bearing Fe-sulfide minerals and to determine the nature of the gold within the Fe-sulfide mineral



structure. HRTEM diffraction patterns (Figure 42) reveal that at least some of the fine ore-stage Fe-sulfide crystals are arsenic-bearing marcasite, rather than pyrite. HRTEM would reveal Au if present in clusters of atoms, nanocrystals or inclusions. HRTEM analyses conducted by Bakken et al. (1991) did not detect particulate gold within ore-stage Fe-sulfide mineral samples at the Carlin deposit. No Au was detected in any of the HRTEM analyses in this study. Based on the lack of Au detection, it is inferred that Au is not present within the crystal structure as microinclusions. These results are consistent with the SIMS analyses, which also failed to identify the presence of gold microinclusions in the ore-stage Fe-sulfide minerals.

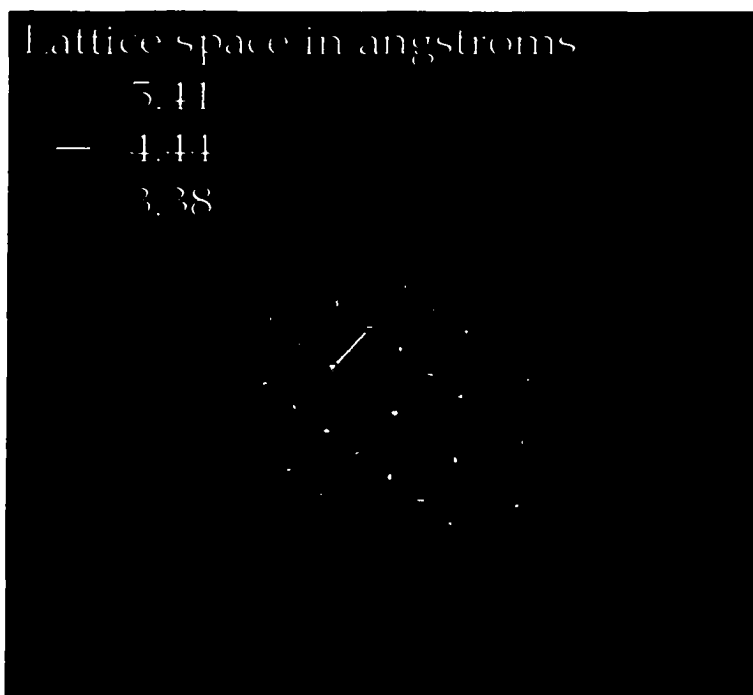


**Figure 42.** This HRTEM diffraction pattern of sample UC1079-4850-181.50-38-197 revealed that some of the finely crystalline Fe-sulfide minerals are arsenic-bearing marcasite, rather than pyrite. The pattern is a diagrammatic representation of the unit cell within the crystal lattice of marcasite. Marcasite, a dimorph of pyrite, is orthorhombic with cell edges  $a = 4.44$ ,  $b = 5.41$ , and  $c = 3.38$  Å (Deer et al., 1966), thus producing the projection above. Pyrite, a cubic mineral, would have produced a pattern with equal  $a$ ,  $b$ , and  $c$  unit cell edge lattice spaces.

## CHAPTER 8

### DISCUSSION

This study of Fe-sulfide minerals from the Getchell mine indicates the presence of: (1) euhedral, trace element-poor pyrite, and (2) finely crystalline, anhedral, trace element-rich Fe-sulfide minerals. The work of Huston et al. (1995) on trace element-enriched pyrite from volcanogenic massive sulfide deposits in Australia suggests that trace elements are likely to occur in sulfides as: (1) stoichiometric substitutions for Fe or S, or (2) as nonstoichiometric substitutions within the pyrite lattice.

Analyses of Fe-sulfide minerals in this study indicate that pre-ore and late-ore pyrite contain approximately stoichiometric concentrations of major elements Fe and S plus trace amounts of Co, Ni, and Pb. Ore-stage pyrite/ marcasite contains concentrations of Fe and S lower than pre-and late-ore pyrite and marcasite, and variable low to nil Co, Ni, and Pb.

#### Pyrite Geochemistry

Huston et al. (1995) suggest that Co and Ni substitute stoichiometrically for Fe in the Fe-sulfide crystal lattice. Co, Ni, and Fe are group 8A transition metal elements and exhibit similar electronegativities and ionic properties. These elements are chemically similar, and have similar ionic radii and charge ( $\text{Co}^{2+}$  0.73 Å,  $\text{Ni}^{2+}$  0.77 Å,  $\text{Fe}^{2+}$  ~0.71 Å)

(Brownlow, 1996). Owing to these similarities, Co and Ni likely substitute readily for Fe in the pyrite lattice without distorting the crystal or creating a charge imbalance.

Huston et al. (1995) and Cook and Chrysoulis (1990) suggest that due to some similarities in electronegativities, ionic properties, and ionic radii ( $\text{As}^{3+}$  0.72 Å,  $\text{Tl}^{3+}$  0.97 Å,  $\text{Sb}^{3+}$  0.69 Å,  $\text{Cu}^{2+}$  0.81 Å,  $\text{Au}^{3+}$  0.78 Å) (Brownlow, 1996), the ore-stage trace elements may stoichiometrically substitute for Fe ( $\text{Fe}^{2+}$  ~0.71 Å) within the Fe-sulfide mineral crystal structure. However, except for  $\text{Cu}^{2+}$ , a charge imbalance would result.

This study demonstrates that ore-stage pyrite/marcasite contain less than stoichiometric concentrations of major elements Fe and S, low trace concentrations of Co, Ni, and Pb, and enrichments of ore-stage trace elements Hg, Tl, As, Au, Cu, and Sb.  $\text{As}^{3+}$ ,  $\text{Tl}^{3+}$ ,  $\text{Sb}^{3+}$ ,  $\text{Cu}^{2+}$ , and  $\text{Au}^{3+}$  likely substitute for  $\text{Fe}^{2+}$  in the cation position.  $\text{Pb}^{2+}$  and  $\text{Hg}^{2+}$ , although exhibiting the same charge as  $\text{Fe}^{2+}$ , are larger in ionic radius ( $\text{Pb}^{2+}$  = 1.37 Å,  $\text{Hg}^{2+}$  = 1.10 Å) (Brownlow, 1996), suggesting that the substitution of  $\text{Pb}^{2+}$  and  $\text{Hg}^{2+}$  for Fe would be less likely to occur.

#### The Chemical State of Au

Early petrographic investigations into “invisible gold” by Bürg (1930) concluded that it is “present in chemical combination in the pyrite, and that the gold is often present in a submicroscopic state ( $<0.1 \mu\text{m}$ ).” Studies on gold ore using Mössbauer spectrometry, carried out by Wagner et al. (1986), confirmed that invisible gold does exist in Fe-sulfide minerals, but they did not identify the chemical state of Au.

Knowing whether gold is present as a charged or uncharged ion in the pyrite structure would aid in determining Au depositional mechanisms. Ionic Au ( $\text{Au}^{1+}$ ,  $\text{Au}^{3+}$ )

would be part of the pyrite structure (Arehart et al., 1993a; Simon et al., 1999); Au microinclusions would be uncharged ( $\text{Au}^0$ ) (Simon et al., 1999). High-resolution microscopy conducted by Bakken et al. (1989) showed no evidence for the occurrence of Au particles as microinclusions within auriferous Fe-sulfide minerals. SIMS and EMP analyses conducted on auriferous arsenopyrite and As-enriched pyrite led Arehart et al. (1993a) to suggest that charged ions of gold are present in solid solution, rather than neutrally charged microinclusions of gold ( $\text{Au}^0$ ). X-ray adsorption fine structure (EXAFS) analyses by Simon et al. (1999) suggest that gold precipitated as  $\text{Au}^{1+}$  where hydrothermal fluids were undersaturated with respect to native gold, and that it precipitated as  $\text{Au}^0$  where pyrite was deposited from fluids that were saturated with respect to gold.

SIMS depth profiling of Getchell Fe-sulfide minerals in this study documented the presence of colloidal-sized  $\text{Au}^0$  microinclusions in R3 realgar. The largest gold grain detected was 0.1  $\mu\text{m}$  in diameter. SIMS depth profiling failed to detect colloidal Au microinclusions in all evaluated Fe-sulfide mineral crystals. TEM analysis of the ore-stage pyrite/marcasite also failed to detect Au as microinclusions in the ore-stage sulfides. These analyses indicate that Au is present in an ionic state ( $\text{Au}^{+1}$  or  $\text{Au}^{+3}$ ) in ore-stage pyrite/marcasite, and suggest that: 1) the hydrothermal fluids that deposited the ore-stage pyrite/marcasite were undersaturated with respect to native gold, and 2) the later hydrothermal fluids that deposited the realgar may have been saturated with respect to native gold.

#### Trace Element Substitution in Fe-Sulfide Minerals

Studies of Carlin-type gold deposits have shown that significant As was

concentrated in pyrite with trace Sb, Hg, and Au (Wells and Mullens, 1973; Radtke, 1985; Arehart et al., 1993a; Ferdock et al., 1997; Simon et al., 1999; and Cline, 2001). These studies suggest that As plays an important role in the incorporation of the ore-stage trace elements into the Fe-sulfide mineral structure. Huston et al. (1995) concluded that ore-stage trace elements  $\text{As}^{3+}$ ,  $\text{Ti}^{3+}$ , and  $\text{Au}^{3+}$  are most likely to occur as nonstoichiometric substitutions in the Fe-sulfide mineral lattice.

Studies conducted by Fleet et al. (1989) and Huston et al. (1995) determined that the most common nonstoichiometric element substituting in the pyrite lattice is As, which forms a metastable  $\text{Fe}(\text{As,S})_2$  solid solution, and is the probable mechanism for producing As-rich Fe-sulfide minerals. Extensive incorporation of As or Sb into sulfide mineral structures leads to the formation of accessory minerals such as orpiment ( $\text{As}_2\text{S}_3$ ), Realgar ( $\text{AsS}$ ), or stibnite ( $\text{Sb}_3\text{S}_3$ ) (Cook and Chryssoulis, 1990), minerals which are paragenetically associated with ore-stage Fe-sulfide mineralization at Getchell and other Carlin-type deposits.

Arehart et al. (1993a) suggested that the covariance of Au and As in individual Fe-sulfide crystals in Carlin-type systems results from gold entering the pyrite/marcasite structure as a coupled substitution with arsenic. Coupled substitution is most likely to take place by one of two mechanisms: substitution in both cation and anion sites with substitution of  $\text{Au}^{3+}$  for  $\text{Fe}^{2+}$  and one  $\text{As}^{2-}$  for one  $\text{S}^{1-}$ , yielding  $([\text{Au}^{3+}] [\text{Fe}^{2+}])([\text{AsS}]^3 - [\text{S}_2]^{2-})$ , or substitution of one  $\text{Au}^{3+}$  and one  $\text{As}^{1+}$  for two  $\text{Fe}^{2+}$ , yielding  $([\text{Au}^{3+}, \text{As}^{1+}] [2\text{Fe}^{2+}]) 2\text{S}_2$ . Cook and Chryssoulis (1990) prefer coupled substitution in cation and anion sites and suggest that nonstoichiometric substitution of  $\text{As}^{2-}$  (0.72 Å) for  $\text{S}^{1-}$  (1.72 Å) occurs through  $[\text{AsS}]^3$  substitution for  $\text{S}_2^{2-}$ . The resulting charge

imbalance is satisfied by substitution of trivalent metal ions (Cook and Chrysosoulis, 1990; Huston et al., 1995) such as  $\text{As}^{3+}$ ,  $\text{Tl}^{3+}$ ,  $\text{Sb}^{3+}$ ,  $\text{Au}^{3+}$ , and  $\text{Hg}^{3+}$  for  $\text{Fe}^{2+}$ .

In this study, statistical analyses of EMP data from ore-stage Fe-sulfide minerals show that As, Tl, and Cu, and less commonly Hg, and Sb accompany Au.  $\text{As}^{3+}$ ,  $\text{Tl}^{3+}$ ,  $\text{Au}^{3+}$ ,  $\text{Hg}^{3+}$ , and  $\text{Sb}^{3+}$  substitute for  $\text{Fe}^{2+}$  in the cation site.  $\text{As}^{2-}$  likely substitutes for  $\text{S}^{1-}$  in the anion site.  $\text{Cu}^{2+}$  (0.81 Å) exhibits a significant positive correlation with the ore-stage elements, and its similarities to Fe suggest that Cu substitutes for Fe (~0.71 Å) in the pyrite structure.  $\text{Cu}^{2+}$  also shows positive correlation with Au in ore-stage pyrite/marcasite. Although the valence differs,  $\text{Cu}^{2+}$  exhibits geochemical properties similar to  $\text{Au}^{3+}$ .  $\text{Cu}^{2+}$  may form a coupled cation substitution with  $\text{Au}^{3+}$  for  $\text{Fe}^{2+}$ , and could be incorporated into the site of  $\text{Fe}^{2+}$ , forming  $([\text{Cu}^{2+} + \text{Au}^{3+}] [2\text{Fe}^{2+}])([\text{As}^{2-}, 1.5 \text{S}_2^{2-}][2\text{S}_2^{2-}])$ .

#### THE FORMATION OF TRACE ELEMENT-RICH FE-SULFIDE MINERALS

Huston et al. (1995) speculate that concentrations of ore-stage and non-ore stage trace elements are controlled by pyrite crystal habit, which is in turn directly affected by fluid composition and rate of crystallization of the sulfide minerals. Studies conducted by Raiswell and Plant (1980) and Huston et al. (1995) suggest that rapid precipitation during disequilibrium allows incorporation of increased nonstoichiometric components. Conditions of rapid precipitation (Huston et al., 1995) enhance disequilibria, facilitate the incorporation of trace metals, and are ultimately responsible for the metastable incorporation of high levels of arsenic into the pyrite lattice. Roedder (1968) and Huston et al. (1995) suggested that colloform, overgrowth, and framboidal morphologies form because of the rapid precipitation of the minerals.

## Pyrite and Marcasite Formation

Previous studies of Fe-sulfide mineral formation (Allen et al., 1912; Giggenbach, 1974; Schoonen and Barnes, 1991) determined that pyrite forms and is stable in neutral to alkaline solutions below 240 °C. Other experiments and models (Allen et al., 1912; Goldhaber and Stanton, 1987) confirmed the formation of pyrite above pH 4.5. Additionally, experimental investigations by Schoonen and Barnes (1991) determined that both pyrite and marcasite can precipitate simultaneously from solutions between 100 and 300°C, possibly explaining observations of both pyrite and marcasite in the ore-stage Fe-sulfide minerals in this study.

The amount of pyrite or marcasite produced by sulfidation is strongly dependent on pH (Schoonen and Barnes, 1991). Marcasite will form at all temperatures in natural solutions that are below a pH of 5 and contain  $\text{H}_2\text{S}$  and  $\text{HS}^-$  as the dominant S phases (Murowchick and Barnes, 1986). Marcasite is the predominant sulfide mineral produced in systems with pH lower than 4.5 (Allen et al., 1914, Goldhaber and Stanton, 1987). Studies conducted by Murowchick and Barnes (1986) determined that the precipitation of marcasite in nature indicates that: (1) the marcasite precipitated from acidic fluids with a pH less than 5, (2) the temperature of deposition was at or below 240° C and the post-deposition temperature remained below 160°C, and (3) that  $\text{H}_2\text{S}$  was present.

Experiments of marcasite and pyrite synthesis and precipitation conducted by Murowchick and Barnes (1987) determined that the temperature of crystal growth and the degree of supersaturation of the source fluids have profound effects on the morphologies of hydrothermally grown pyrite crystals. They concluded that two different types of Fe-sulfide crystals formed: (1) well-formed crystals with complete

faces formed primarily during steady-state conditions and, (2) fine crystals of Fe-sulfide minerals without any distinctive crystal shape formed during periods of rapid cooling. Murowchick and Barnes (1987) observed that: (1) low degrees of saturation at temperatures of 250°C produced acicular crystals, and higher degrees of saturation at 250°C produced crystals with perfectly smooth crystal faces, (2) relatively higher temperatures of 450°C and low degrees of saturation resulted in the formation of rough cubes, and (3) high degrees of saturation combined with rapid cooling gradients produced crystals with incomplete faces that often grew on older, primary crystal faces, producing a very finely crystalline sulfide that had no distinctive crystal shape.

#### Pre-Ore, Euhedral Fe-Sulfide Minerals at Getchell

Major and trace element geochemistry indicate that pre-ore P1a and P1b pyrites are near stoichiometric. The presence of pyrite rather than marcasite suggests that the pre-ore fluids had a pH above 4.5.

The morphology and chemistry of P1a and P1b pyrites suggest slow crystal growth at steady-state conditions from fluids that were not saturated in ore-stage trace metals. The euhedral crystal shape and the near-stoichiometric chemistry of the pyrite suggest that slow crystal growth allowed ordered arrangement of stoichiometric elements (Fe and S) and substitution by trace elements geochemically similar to Fe (Co and Ni).

#### Ore-Stage, Finely Crystalline, Anhedral Fe-Sulfide Minerals at Getchell

Petrographic analysis of ore-stage Fe-sulfide minerals P2a, P2b, and P2c revealed the presence of both pyrite and marcasite. The textures of the ore-stage sulfide minerals



are suggestive of rapid precipitation during system disequilibrium, and the presence of marcasite indicates that the pH fell below 4.5.

Conditions of rapid precipitation are consistent with the fine crystal habit and trace element-rich character of P2a, P2b, and P2c pyrite/ marcasite at Getchell. EMP analysis of the ore-stage Fe-sulfide minerals show that Fe plus S compose 89.44 mass % of P2a and 82.73 mass % of P2c, leaving 10.56 mass % and 17.27 mass % of the P2a and P2c pyrite structures, respectively, composed of the other trace elements. Rapid crystallization precluded an ordered arrangement of the elements in the crystal lattice and facilitated the incorporation of Hg, Tl, As, Au, Cu, and Sb into the sulfide crystal structure.

The generally positive correlation between most of the ore-stage trace elements in P2a, P2b, and P2c pyrite/ marcasite reflects the fact that rapid crystallization enhanced the incorporation of all ore-stage elements into the pyrite crystal structure, resulting in high covariance between these trace elements.

Changes in system chemistry and precipitation mechanisms within the system may explain the morphological and trace element differences between the sharp, distinct rims of P2a, the framboid-like P2b, and the very high grade, irregular, and subtle rims of P2c Fe-sulfide minerals. Fe-sulfide minerals P2a and P2b exhibit textures of open-space formation, whereas P2c sulfide rims may have formed by replacement. Replacement is indicated by rounding of the pre-ore cores, the sharp but irregular contact between pre-ore cores and ore-stage rims, and similar relief and polish of the P2c core and rim. The significant differences in the two types of rims strongly suggest that they were formed by different processes.

Geochemical analyses of P2d pyrite/ marcasite show that 97.37 mass % is composed of Fe and S, and 2.63 mass % consists of other trace elements. Although not as enriched in trace elements as P2a, P2b, and P2c, P2d pyrite/ marcasite may have precipitated either at the beginning of, or near the end of, ore-stage precipitation.

#### Late-Ore Marcasite at Getchell

The presence of late-ore P3 marcasite, rather than pyrite, suggests that  $H_2S$  and  $HS^-$  dominated the late-ore fluids and pH was below 5 (Murowchick and Barnes, 1986; Goldhaber and Stanton, 1987). Paragenetic observations and major and trace element geochemistry of the P3 marcasite indicate formation during the late-ore stage.

The coarse euhedral crystals and prismatic laths indicate slow, ordered crystal growth. Ore-stage trace elements either were not incorporated into the marcasite structure owing to their absence in the fluids, or the equilibrium crystallization processes did not allow their incorporation. Analyses show that Fe and S compose 97.88 mass % of P3 marcasite, with other elements occupying 2.12 mass %.

#### Model for Fe-Sulfide Precipitation at Getchell

Geochemical and morphological data suggest that the fluids that precipitated P1a and P1b pyrite were neutral to basic. P1a and P1b pyrite crystals precipitated slowly from fluids that were depleted in ore-stage trace elements.

Ore-stage pyrite/ marcasite precipitation was accompanied by decalcification and silicification of the host limestone. The responsible fluids may have been saturated in or contained abundant dissolved ore-stage elements and silica. The ore-stage Fe-sulfide minerals are generally paragenetically located between quartz crystals or

incorporated in the outer edges of the surrounding jasperoid. This relationship suggests that calcite was removed and Q2 quartz crystallization was in progress before the ore-stage Fe-sulfide minerals formed.

Trace element compositions of the P2a, P2b, P2c, and P2d Fe-sulfide minerals likely reflect the composition of the fluids at the time of pyrite/marcasite precipitation. Furthermore, the conditions were such that both trace element-rich pyrite and marcasite may have simultaneously precipitated. Crystal forms and geochemistry of the ore-stage Fe-sulfide minerals suggest that types P2a through P2d formed during a period of rapid precipitation and possible disequilibrium, allowing the incorporation of elevated concentrations of trace elements in the pyrite structure.

With continued quartz and pyrite/marcasite precipitation, the concentration of trace elements in the fluids became depleted, or the precipitation rate of the pyrite/marcasite decreased and nonstoichiometric trace elements were excluded from the pyrite/marcasite lattice. This transition from trace element-rich ore-stage pyrite/marcasite to trace element-poor late-ore stage marcasite marks an evolution in the physical or chemical conditions of the system.

During the post-ore stage of the system, marcasite may have precipitated slowly from saturated fluids possibly under equilibrium conditions, thus producing euhedral, blocky crystals. The system further evolved and only the acicular, blade-like marcasite precipitated. P3 marcasite was overgrown by late-ore calcite, indicating that the hydrothermal fluids in the system had further evolved to a less acidic pH conducive to calcite precipitation.

## CHAPTER 9

### CONCLUSIONS

The gold-ore at Getchell is located within decarbonatized and silicified silty carbonate and limestone rocks. The ore and gangue mineral assemblage includes calcite, barite, pyrite, marcasite, jasperoid quartz, drusy quartz, chalcedony, realgar, orpiment, stibnite and galkhaite. Of these minerals, four types of pyrite, realgar, and galkhaite are host to the economically significant gold at Getchell.

Three groups of morphologically and chemically distinct Fe-sulfide minerals are present at the Getchell Carlin-type deposit: (1) pre-ore diagenetic and hydrothermal pyrite hosted by Stage 1, non-silicified, calcite-bearing lithologies and altered igneous dikes, (2) ore-stage pyrite/marcasite hosted by Stage 2, decalcified and silicified ore-stage lithologies, and (3) late-ore stage marcasite, hosted by Stage 3 calcite that crosscuts the previous assemblages.

This study documents seven morphologically and chemically different types of pyrite and marcasite. There are four specific morphologies of the ore-stage Fe-sulfide minerals that are associated with elevated concentrations of a characteristic suite of elements, Hg, Tl, As, Au, Cu, and Sb. The pre-ore and late-ore stage pyrites contain nil or trace Hg, Tl, As, Au, Cu, and Sb. The differences in host rocks, mineral assemblages, and trace element relationships suggest that that the fluids that precipitated the pre-ore

and late-ore pyrite and marcasite were different from those that precipitated the ore-stage Fe-sulfide minerals.

Based on the study by Simon et al. (1999), the deposition mechanisms of Au at Getchell are suggested by the distribution of ionic Au within the structure of the ore-stage Fe-sulfide minerals and the presence of Au<sup>0</sup> inclusions in realgar. The differences in the structure of Au in the pyrite at Getchell indicate that the fluids that precipitated the ore-stage pyrite were undersaturated with respect to Au concentration, and the fluids that precipitated the late-ore realgar may have been saturated in Au.

Further research that may compliment this study includes sulfur isotope analyses and color cathodoluminescence. Sulfur isotope analyses would aid in distinguishing the source of sulfur for the ore-stage and non-ore stage Fe-sulfide mineral populations. Color cathodoluminescence analyses of the ore-stage jasperoid and drusy quartz populations would aid in determining the trace metals present in the ore fluids.

## **APPENDIX 1**

List of underground drill holes sampled at the Getchell Mine during 1997. Depths and northings identify locations of stopes in the Getchell underground mine. (See Figure 3). Drill hole number identifies the hole drilled in the stope. Footages for samples examined for this study are listed in Appendix 2.

**Northwest ore body**  
**197.00-181.00**

UC1085-4850-181.50-31  
UC1081-4850-181.50-32  
UC1076-4850-181.50-34  
UC1083-4850-181.50-36  
UC1078-4850-181.50-37  
UC1079-4850-181.50-38  
UC1080-4850-181.50-38  
UC1086-4850-181.50-40  
UC1084-4850-181.50-41  
UC1087-4850-181.50-42  
UC1088-4850-181.50-43  
UC1017-4775-183.00-71  
UC0573-5000-184.00-09  
UC0608-5000-184.00-14  
UC0606-5000-184.00-15  
UC1046-4790-184.00-25  
UC0571-5000-184.50-02  
UC0569-5000-184.50-03  
UC0568-5000-184.50-04  
UC1012-4790-184.50-31  
UC1019-4790-184.50-33  
UC1020-4790-184.50-41  
UC1045-4790-185.00-28  
UC1029-4790-185.00-23  
UC0879-4850-185.00-25  
UC0868-4850-185.50-32  
UC1019-4790-184.50-33  
UC0867-4850-185.50-33  
UC0872-4850-185.50-37  
UC0654-5000-186.00-12  
UC0655-5000-186.00-14  
UC0768-5000-186.00-18  
UC1049-4775-188.00-10  
UC0879-4850-187.00-24  
UC1059-4775-187.00-34  
UC1027-4775-189.50-01  
UC1031-4775-189.50-02  
UC1031-4775-189.50-03  
UC1036-4760-189.50-07  
UC1037-4760-189.50-09  
UC1048-4775-189.50-12  
UC1054-4775-189.50-14  
UC1069-4775-189.50-20  
UC1058-4775-190.50-01  
UC1047-4775-193.00-01

**Main ore body**  
**181.00-166.00**

UC0785-5100-168.50-16  
UC0736-5100-171.50-26  
UC0452-4850-173.00-14  
UC0467-4850-173.00-16  
UC0782-4775-173.00-24  
UC0782-4775-173.00-26  
UC0519-4850-173.50-15  
UC0519-4850-173.50-25  
UC- ND -4775-173.50-27  
UC- ND -4775-173.50-31  
UC0802-4775-173.50-34  
UC- ND -5100-175.50-25

**Southern ore body**  
**166.00-145.00**

UC0932-4850-157.00-02  
UC0926-4850-157.00-07  
UC0822-4850-160.00-07  
UC0828-4850-160.00-09  
UC0845-4850-160.00-11  
UC0845-4850-160.00-13  
UC1035-4655-162.00-28  
UC1018-4750-162.50-10  
UC1028-4750-163.00-09  
UC1074-4655-164.00-05  
UC1075-4655-164.00-06  
UC1077-4655-164.00-08  
UC1082-4655-165.00-09

Sample numbers contain four important specifiers that indicate:

UCXXXX -	XXXX -	XXX.XX -	XX
Getchell	Depth	Northing	Drillhole #
index #	ASL	of Getchell	within stope
		underground	
		stope	

ND = No Data

## **APPENDIX 2**



107

## **APPENDIX 3**

## EMP detection limits

EMP Analyses	Fe	S	Pb	Co	Hg	Ag	Tl	Ni	As	Au	Cu	Sb	Zn	Mo
Analysis 1	0.189	0.222	0.13	0.01	0.03	0.09	0.03	0.01	0.01	0.01	0.01	0.03	0.01	0.04
Analysis 2	0.187	0.223	0.04	0.01	0.03	0.09	0.03	0.01	0.01	0.01	0.01	0.03	0.01	0.04
Analysis 3	0.191	0.223	0.04	0.01	0.03	0.09	0.03	0.01	0.01	0.01	0.01	0.03	0.01	0.04

1.0 sigma detection limit (st. dev) (wt.%)

## **APPENDIX 4**

EMP trace element analysis of realgar, orpiment, stibnite and galkhaite.

R3 realgar															
Sample #	Fe	S	Pb	Co	Hg	Ag	Tl	Ni	As	Au	Cu	Sb	Zn	Mo	Total wt.%
UC0519-4850-181.50-41-62	0.140	19.180	0.300	0.070	0.350	0.950	0.820	0.900	73.580	0.350	0.110	0.570	0.100	0.170	96.990
UC0519-4850-181.50-41-62	0.160	27.550	0.390	0.080	0.480	1.540	0.870	0.100	74.660	0.480	0.130	0.690	0.100	0.170	107.510
UC1084-4850-181.50-41-197	0.010	12.060	0.070	0.000	0.000	0.110	0.170	0.000	78.390	0.120	0.000	0.130	0.000	0.000	91.040
UC1084-4850-181.50-41-197	0.030	20.210	0.100	0.000	0.000	0.540	0.170	0.000	78.830	0.190	0.000	0.270	0.000	0.000	100.330
UC1084-4850-181.50-41-197	0.050	27.850	0.370	0.000	0.000	1.450	0.200	0.000	78.580	0.490	0.000	0.350	0.010	0.000	109.330
UC0845-4850-160.0-13-32	0.010	27.790	0.040	0.000	0.010	0.000	0.320	0.000	80.250	0.010	0.000	0.050	0.000	0.000	108.490
UC0845-4850-160.0-13-32	0.000	14.610	0.080	0.050	0.380	0.000	0.740	0.050	78.850	0.000	0.040	0.120	0.040	0.120	95.080
UC1082-4655-165.0-09-101	0.040	26.280	0.210	0.020	0.000	0.660	0.170	0.000	80.700	0.030	0.020	0.070	0.020	0.000	108.220
UC1082-4655-165.0-09-101	0.050	26.150	0.450	0.060	0.050	0.940	0.000	0.040	79.860	0.330	0.000	0.560	0.030	0.060	108.590
UC1082-4655-165.0-09-101	0.040	20.020	0.160	0.040	0.060	0.350	0.380	0.040	80.410	0.040	0.030	0.210	0.030	0.020	101.810
UC1082-4655-165.0-09-101	0.050	25.660	0.430	0.060	0.090	1.010	0.350	0.050	78.630	0.360	0.040	0.580	0.020	0.240	107.560
UC1079-4850-181.50-38-176	0.060	29.010	0.460	0.040	0.060	1.190	0.300	0.040	71.800	0.530	0.030	0.640	0.010	0.220	104.390
UC1079-4850-181.50-38-176	0.060	29.270	0.480	0.050	0.000	1.410	0.340	0.040	72.180	0.600	0.030	0.860	0.010	0.250	105.590
Average	0.054	23.511	0.272	0.036	0.114	0.781	0.372	0.097	77.440	0.272	0.033	0.392	0.028	0.096	
Orpiment															
Sample #	Fe	S	Pb	Co	Hg	Ag	Tl	Ni	As	Au	Cu	Sb	Zn	Mo	Total wt.%
UC1082-4655-165.0-09-101	0.040	35.660	0.540	0.060	0.000	1.800	0.220	0.050	63.280	0.490	0.050	4.800	0.000	0.400	107.430
UC1082-4655-165.0-09-101	0.040	35.180	0.510	0.050	0.000	2.140	0.210	0.050	62.430	0.600	0.030	4.100	0.010	0.400	105.820
Average	0.040	35.420	0.525	0.055	0.000	1.970	0.215	0.050	62.855	0.545	0.040	4.450	0.005	0.400	

**Stibnite**

Sample #	Fe	S	Pb	Co	Hg	Ag	Tl	Ni	As	Au	Cu	Sb	Zn	Mo	Total wt. %
UC0845-4850-160.0-13-32	0.062	25.653	0.122	0.100	1.021	1.475	1.150	0.152	0.000	0.473	0.200	66.716	0.190	0.000	104.190
UC1075-4655-164.00-06-86	0.029	27.246	0.048	0.000	0.106	0.000	0.000	0.000	3.782	0.000	0.000	66.188	0.000	0.000	97.401
Average	0.046	26.450	0.085	0.050	0.564	0.738	0.575	0.076	1.891	0.237	0.100	66.452	0.095	0.000	

**Galkhaite**

Sample #	Fe	S	Pb	Co	Hg	Ag	Tl	Ni	As	Au	Cu	Sb	Zn	Mo	Total wt. %
UC0845-4850-160.0-13-32	0.490	20.750	0.830	0.260	50.860	3.330	2.960	0.250	16.350	0.970	3.460	3.180	1.590	0.600	105.890
UC0845-4850-160.0-13-32	0.300	20.930	0.740	0.270	51.800	3.350	3.130	0.250	16.580	0.970	3.490	2.730	1.530	0.600	106.660
UC0845-4850-160.0-13-32	1.450	22.210	0.790	0.230	47.530	4.350	2.410	0.220	17.580	1.070	3.400	4.670	1.650	0.640	108.200
UC0845-4850-160.0-13-32	2.600	22.280	0.810	0.250	45.550	3.310	3.620	0.230	18.170	0.950	3.540	2.650	1.520	0.560	106.050
Average	1.210	21.543	0.793	0.253	48.935	3.585	3.030	0.238	17.170	0.990	3.473	3.308	1.573	0.600	

**Cinnabar alteration within galkhaite**

Sample #	Fe	S	Pb	Co	Hg	Ag	Tl	Ni	As	Au	Cu	Sb	Zn	Mo	Total wt. %
UC0845-4850-160.0-13-32	0.810	15.420	1.050	0.380	82.840	4.260	2.890	0.340	2.020	1.250	0.600	2.780	1.630	0.650	116.930
UC0845-4850-160.0-13-32	0.990	15.300	1.010	0.380	81.870	4.060	2.800	0.340	2.380	1.260	0.660	2.740	1.730	0.670	116.200
Average	0.900	15.360	1.030	0.380	82.355	4.160	2.845	0.340	2.200	1.255	0.630	2.760	1.680	0.660	

Due to the volatile and absorbent nature of As and S in the sulfosalt minerals, sulfur and wt. % totals may be high or low because of the volatilization. Due to the high amounts of absorption and vaporization, Armstrong correction was used to "normalize" the As and S totals.

## **APPENDIX 5**

# EMP trace element data of Fe-sulfide minerals.

wt.% = 0 for analyses below detection limit.

EMP detection limits reported in Appendix 3.

P1b Igneous Pyrite																
Analysis #	Sample	Fe	S	Pb	Co	Hg	Ag	Ti	Ni	As	Au	Cu	Sb	Zn	Mo	Total Wt. %
1	UC1079-4850-181.50-38-421	45.107	54.441	0.195	0.062	0.000	0.000	0.000	0.009	0.000	0.000	0.000	0.000	0.000	0.000	99.814
2	UC1079-4850-181.50-38-421	45.130	54.434	0.196	0.064	0.033	0.000	0.067	0.000	0.000	0.000	0.015	0.000	0.000	0.000	99.939
3	UC1079-4850-181.50-38-421	44.645	52.103	0.233	0.060	0.000	0.000	0.000	0.013	0.000	0.000	0.000	0.000	0.011	0.000	97.065
4	UC1079-4850-181.50-38-421	45.190	54.374	0.226	0.042	0.000	0.000	0.000	0.029	0.000	0.000	0.000	0.000	0.000	0.000	99.861
5	UC1079-4850-181.50-38-441	46.398	55.065	0.211	0.133	0.000	0.000	0.051	0.000	0.000	0.015	0.000	0.000	0.000	0.000	101.893
6	UC1079-4850-181.50-38-441	46.354	54.681	0.211	0.081	0.000	0.000	0.054	0.000	0.000	0.000	0.000	0.000	0.000	0.000	101.381
7	UC1079-4850-181.50-38-441	46.457	55.052	0.239	0.069	0.000	0.000	0.095	0.000	0.000	0.000	0.000	0.000	0.000	0.000	101.912
Average		45.612	54.307	0.216	0.076	0.005	0.000	0.038	0.007	0.000	0.002	0.002	0.000	0.002	0.000	
Minimum value		44.645	52.103	0.020	0.042	0.000	0.000	0.000	0.000	0.000	0.000	0.000	0.000	0.000	0.000	
Maximum value		46.457	55.065	0.239	0.133	0.033	0.000	0.095	0.029	0.000	0.015	0.015	0.000	0.011	0.000	



# EMP trace element data of Fe-sulfide minerals.

P1a Meta-sedimentary Pyrite																
Analysis #	Sample	Fe	S	Pb	Co	Hg	Ag	Tl	Ni	As	Au	Cu	Sb	Zn	Mo	Total Wt. %
8	UC1045-4790-185.0-28-206	46.087	50.132	0.225	0.047	0.000	0.000	0.000	0.027	0.000	0.000	0.021	0.030	0.072	0.000	96.641
9	UC1045-4790-185.0-28-206	45.773	54.597	0.318	0.051	0.000	0.000	0.035	0.040	0.000	0.000	0.017	0.000	0.087	0.000	100.918
10	UC1045-4790-185.0-28-206	45.620	53.531	0.218	0.045	0.000	0.000	0.089	0.000	0.000	0.017	0.027	0.000	0.357	0.000	99.904
11	UC1045-4790-185.0-28-206	45.067	53.810	0.267	0.052	0.000	0.000	0.000	0.000	0.000	0.000	0.000	0.000	0.259	0.000	99.455
12	UC0606-5000-184.00-15-157	44.922	50.345	0.000	0.044	0.000	0.000	0.076	0.000	0.332	0.000	0.000	0.000	0.000	0.534	96.253
13	UC0606-5000-184.00-15-157	46.318	54.782	0.000	0.041	0.000	0.000	0.046	0.000	0.000	0.000	0.000	0.000	0.000	0.000	101.187
14	UC0606-5000-184.00-15-157	46.072	54.684	0.000	0.054	0.000	0.000	0.000	0.000	0.323	0.000	0.000	0.000	0.000	0.000	101.133
15	UC0606-5000-184.00-15-157	45.297	54.502	0.000	0.042	0.000	0.000	0.000	0.000	0.137	0.000	0.000	0.000	0.000	0.000	99.978
16	UC0606-5000-184.00-15-157	44.916	54.009	0.000	0.047	0.000	0.000	0.084	0.000	0.119	0.000	0.013	0.000	0.000	0.000	99.188
17	UC1075-4655-164.00-06-90	45.571	55.565	0.227	0.046	0.000	0.000	0.000	0.000	0.108	0.000	0.000	0.000	0.000	0.000	101.517
18	UC1075-4655-164.00-06-90	44.979	55.223	0.307	0.046	0.000	0.000	0.034	0.000	0.563	0.000	0.000	0.000	0.000	0.000	101.152
19	UC1075-4655-164.00-06-90	45.403	56.294	0.298	0.042	0.000	0.000	0.055	0.098	0.000	0.000	0.000	0.038	0.000	0.000	102.228
20	UC1075-4655-164.00-06-90	45.402	56.435	0.241	0.038	0.000	0.000	0.094	0.105	0.000	0.000	0.000	0.000	0.000	0.000	102.315
21	UC1075-4655-164.00-06-90	44.895	56.418	0.249	0.053	0.000	0.000	0.000	0.047	0.000	0.000	0.012	0.000	0.000	0.000	101.674
22	UC1075-4655-164.00-06-86	45.324	54.511	0.188	0.054	0.032	0.000	0.000	0.209	0.000	0.000	0.000	0.000	0.000	0.000	100.318
23	UC1075-4655-164.00-06-86	45.433	54.105	0.236	0.055	0.000	0.000	0.070	0.000	0.018	0.000	0.000	0.000	0.000	0.000	99.917
24	UC1075-4655-164.00-06-86	45.640	54.667	0.246	0.050	0.000	0.116	0.000	0.039	0.000	0.000	0.000	0.000	0.000	0.000	100.758
25	UC1075-4655-164.00-06-86	45.261	55.139	0.189	0.051	0.000	0.000	0.000	0.000	0.000	0.000	0.000	0.000	0.000	0.000	100.640
26	UC1079-4850-181.50-38-149	45.249	51.770	0.213	0.047	0.000	0.108	0.045	0.011	0.000	0.000	0.000	0.075	0.000	0.000	97.518
27	UC1079-4850-181.50-38-149	45.536	51.087	0.176	0.045	0.000	0.000	0.048	0.000	0.021	0.000	0.000	0.029	0.000	0.000	96.942
28	UC1079-4850-181.50-38-149	45.201	50.843	0.235	0.045	0.054	0.000	0.000	0.000	0.000	0.000	0.362	0.000	0.000	0.000	96.760
29	UC0519-4850-173.50-15-72	45.517	52.553	0.275	0.041	0.000	0.000	0.000	0.000	0.000	0.000	0.000	0.000	0.000	0.000	98.386
30	UC0519-4850-173.50-15-72	45.084	52.380	0.247	0.037	0.036	0.000	0.045	0.012	0.000	0.000	0.000	0.000	0.000	0.000	97.841
31	UC0519-4850-173.50-15-62	46.633	54.482	0.216	0.042	0.059	0.000	0.079	0.040	0.000	0.000	0.000	0.000	0.000	0.000	101.551
32	UC0519-4850-173.50-15-62	46.333	54.474	0.000	0.036	0.249	0.000	0.000	0.132	0.000	0.000	0.000	0.000	0.000	0.000	101.224
34	UC0519-4850-173.50-15-62	45.791	53.312	0.221	0.060	0.000	0.000	0.000	0.868	0.000	0.022	0.000	0.000	0.000	0.000	100.274
35	UC0519-4850-173.50-15-62	45.946	53.835	0.243	0.057	0.000	0.000	0.086	0.476	0.473	0.000	0.000	0.000	0.000	0.000	101.116
36	UC0519-4850-173.50-15-62	45.752	54.897	0.212	0.055	0.000	0.000	0.049	0.019	0.228	0.025	0.000	0.000	0.009	0.000	101.246
37	UC0845-4850-160.0-13-32	45.913	54.987	0.202	0.055	0.000	0.123	0.033	0.000	0.364	0.000	0.000	0.000	0.000	0.000	101.677
38	UC0845-4850-160.0-13-32	45.857	54.633	0.276	0.065	0.000	0.000	0.000	0.011	0.000	0.032	0.000	0.000	0.000	0.000	100.874
39	UC519-4850-173.50-15-139	46.686	55.085	0.220	0.046	0.056	0.000	0.085	0.014	0.000	0.000	0.000	0.000	0.000	0.000	102.192
40	UC519-4850-173.50-15-139	46.493	55.118	0.200	0.057	0.000	0.000	0.000	0.052	0.000	0.027	0.000	0.000	0.000	0.000	101.947

# EMP trace element data of Fe-sulfide minerals.

P1a Pyrite (con't)		Fe	S	Pb	Co	Hg	Ag	Tl	Ni	As	Au	Cu	Sb	Zn	Mo	Total Wt. %
41	UC519-4850-173.50-15-139	46.882	54.716	0.286	0.033	0.000	0.000	0.060	0.000	0.000	0.015	0.000	0.000	0.000	0.000	102.012
42	UC1082-4635-165.0-09-101	46.785	55.040	0.217	0.058	0.000	0.000	0.000	0.010	0.503	0.027	0.000	0.000	0.000	0.000	102.640
43	UC1082-4635-165.0-09-101	46.823	54.763	0.237	0.051	0.000	0.000	0.060	0.000	0.000	0.017	0.000	0.000	0.000	0.000	101.951
44	UC1082-4635-165.0-09-101	46.516	55.241	0.204	0.059	0.000	0.000	0.066	0.000	0.000	0.000	0.000	0.000	0.000	0.000	102.086
45	UC1082-4635-165.0-09-101	45.728	53.339	0.212	0.042	0.000	0.000	0.000	0.000	0.084	0.000	0.000	0.000	0.000	0.000	99.405
46	UC0606-5000-184.00-15-157	45.713	54.905	0.287	0.055	0.000	0.000	0.054	0.000	0.125	0.026	0.000	0.000	0.000	0.000	101.163
47	UC0606-5000-184.00-15-157	46.393	54.475	0.194	0.057	0.046	0.000	0.046	0.000	0.018	0.000	0.000	0.000	0.000	0.000	101.229
48	UC0606-5000-184.00-15-157	46.107	54.799	0.221	0.045	0.000	0.000	0.029	0.000	0.000	0.041	0.000	0.000	0.000	0.000	101.242
49	UC0606-5000-184.00-15-157	46.432	54.482	0.214	0.060	0.000	0.000	0.064	0.017	0.000	0.000	0.000	0.000	0.000	0.000	101.269
50	UC0606-5000-184.00-15-157	46.098	54.085	0.264	0.034	0.000	0.000	0.039	0.012	0.056	0.014	0.000	0.000	0.000	0.000	100.602
Average		45.796	54.144	0.202	0.049	0.013	0.008	0.035	0.053	0.083	0.006	0.011	0.004	0.019	0.013	
Minimum value		44.895	50.132	0.000	0.034	0.000	0.000	0.000	0.000	0.000	0.000	0.000	0.000	0.000	0.000	
Maximum value		46.882	56.435	0.318	0.065	0.249	0.123	0.094	0.868	0.563	0.041	0.362	0.075	0.357	0.534	

P2a Pyrite/Marcasite		Fe	S	Pb	Co	Hg	Ag	Tl	Ni	As	Au	Cu	Sb	Zn	Mo	Total Wt. %
Analysis #	Sample	Fe	S	Pb	Co	Hg	Ag	Tl	Ni	As	Au	Cu	Sb	Zn	Mo	Total Wt. %
51	UC1079-4850-181.50-38-176	40.751	49.864	0.156	0.044	1.028	0.000	0.809	0.015	4.221	0.053	0.280	0.865	0.012	0.000	98.098
52	UC1079-4850-181.50-38-176	41.366	50.601	0.128	0.042	0.845	0.000	0.726	0.012	4.096	0.000	0.249	0.469	0.013	0.000	98.547
53	UC1079-4850-181.50-38-176	41.335	49.824	0.156	0.045	0.734	0.000	0.736	0.017	4.407	0.055	0.240	0.324	0.010	0.000	97.883
54	UC0606-5000-184.00-15-157	37.689	44.540	0.000	0.038	1.070	0.000	1.132	0.000	9.462	0.097	0.335	1.384	0.000	0.581	96.328
55	UC0606-5000-184.00-15-157	39.229	48.775	0.000	0.042	0.982	0.000	0.912	0.014	6.961	0.054	0.320	0.907	0.000	0.000	98.196
56	UC0606-5000-184.00-15-157	39.126	49.761	0.000	0.044	1.060	0.000	0.928	0.018	7.227	0.046	0.325	0.644	0.000	0.000	99.179
57	UC0606-5000-184.00-15-157	38.612	49.128	0.000	0.034	0.719	0.000	0.694	0.000	7.606	0.081	0.223	0.741	0.032	0.000	97.870
58	UC0606-5000-184.00-15-157	38.134	48.882	0.000	0.035	0.918	0.101	1.083	0.000	8.588	0.091	0.329	1.163	0.000	0.000	99.324
59	UC0606-5000-184.00-15-157	39.611	47.569	0.096	0.031	0.953	0.000	0.895	0.012	7.279	0.039	0.333	0.713	0.000	0.000	97.531
60	UC0606-5000-184.00-15-157	41.456	49.893	0.114	0.047	0.517	0.000	0.454	0.050	3.713	0.033	0.230	0.435	0.000	0.000	96.942

# EMP trace element data of Fe-sulfide minerals.

P2a Pyrite/Marcasite (con't)		Fe	S	Pb	Co	Hg	Ag	Tl	Ni	As	Au	Cu	Sb	Zn	Mo	Total Wt. %
61	UC1079-4850-181.50-38-176	44.305	53.621	0.160	0.048	0.000	0.000	0.000	0.043	2.670	0.019	0.077	0.000	0.000	0.000	100.943
62	UC1079-4850-181.50-38-176	37.370	48.524	0.275	0.052	1.829	0.333	1.880	0.062	10.499	0.104	0.516	0.812	0.038	0.000	102.294
63	UC1079-4850-181.50-38-176	40.853	49.464	0.083	0.034	0.922	0.000	0.940	0.015	5.207	0.116	0.137	0.384	0.011	0.000	98.166
64	UC1079-4850-181.50-38-176	42.774	50.178	0.132	0.037	0.370	0.000	0.395	0.000	3.454	0.020	0.068	0.084	0.012	0.000	97.524
65	UC1079-4850-181.50-38-176	40.193	46.905	0.043	0.051	0.750	0.000	0.943	0.023	8.371	0.110	0.333	0.503	0.018	0.000	98.243
66	UC1079-4850-181.50-38-197	41.763	50.866	0.237	0.044	0.312	0.000	0.366	0.000	4.978	0.221	0.264	1.377	0.000	0.000	100.428
67	UC1079-4850-181.50-38-197	41.800	51.351	0.214	0.039	0.343	0.000	0.314	0.000	4.894	0.233	0.245	1.349	0.000	0.000	100.782
68	UC1079-4850-181.50-38-149	37.516	43.039	0.000	0.039	0.546	0.000	0.669	0.058	18.849	0.238	0.246	0.854	0.000	0.000	102.054
69	UC1079-4850-181.50-38-197	41.986	50.726	0.086	0.042	0.297	0.000	0.294	0.012	5.219	0.226	0.285	1.412	0.000	0.000	100.585
Average		40.309	49.132	0.099	0.041	0.747	0.023	0.746	0.018	6.721	0.097	0.265	0.759	0.008	0.031	
Minimum value		37.370	43.039	0.000	0.031	0.000	0.000	0.000	0.000	1.915	0.000	0.077	0.000	0.000	0.000	
Maximum value		44.305	53.621	0.275	0.052	1.829	0.333	1.880	0.062	18.849	0.238	0.516	1.412	0.038	0.581	

P2b Pyrite/Marcasite		Fe	S	Pb	Co	Hg	Ag	Tl	Ni	As	Au	Cu	Sb	Zn	Mo	Total Wt. %
Analysis #	Sample															
70	UC0606-5000-184.00-15-157	34.527	46.182	0.000	0.103	1.053	0.000	1.112	0.581	9.983	0.057	0.347	1.110	0.000	0.000	95.055
71	UC0606-5000-184.00-15-157	38.955	49.735	0.000	0.031	0.837	0.000	0.836	0.000	7.743	0.046	0.296	1.062	0.000	0.000	99.541
72	UC0606-5000-184.00-15-157	34.616	44.546	0.000	0.037	1.252	0.000	1.063	0.000	10.176	0.122	0.306	2.211	0.000	0.000	94.329
Average		36.033	46.821	0.000	0.057	1.047	0.000	1.004	0.194	9.301	0.075	0.316	1.461	0.000	0.000	
Minimum value		34.527	44.546	0.000	0.031	0.084	0.000	0.084	0.000	7.743	0.046	0.296	1.062	0.000	0.000	
Maximum value		38.955	49.735	0.000	0.103	1.252	0.000	1.112	0.581	10.176	0.122	0.347	2.211	0.000	0.000	

EMP trace element data of Fe-sulfide minerals.

P2c: Pyrite/Marcasite																
Analysis #	Sample	Fe	S	Pb	Co	Hg	Ag	Tl	Ni	As	Au	Cu	Sb	Zn	Mo	Total Wt. %
73	UC1084-4850-181.50-41-197	36.061	46.396	0.000	0.028	0.571	0.000	1.192	0.000	13.886	0.339	0.625	0.609	0.000	0.000	99.707
74	UC1084-4850-181.50-41-197	36.261	47.363	0.000	0.049	0.667	0.000	1.304	0.000	13.411	0.296	0.711	0.656	0.000	0.000	100.718
75	UC1084-4850-181.50-41-197	35.674	43.230	0.237	0.067	0.974	0.206	1.704	0.038	14.432	0.338	0.673	0.584	0.017	0.000	98.174
76	UC1084-4850-181.50-41-197	36.877	44.379	0.000	0.039	0.505	0.000	1.008	0.000	14.408	0.302	0.595	0.450	0.000	0.000	98.563
77	UC1084-4850-181.50-41-197	37.272	45.647	0.000	0.034	0.726	0.000	1.314	0.000	12.539	0.303	0.729	0.612	0.000	0.000	99.176
78	UC1084-4850-181.50-41-197	39.237	48.259	0.000	0.046	0.506	0.000	1.064	0.000	11.037	0.193	0.554	0.392	0.012	0.000	101.300
79	UC1084-4850-181.50-41-197	37.080	45.405	0.000	0.022	0.507	0.172	1.183	0.000	16.433	0.313	0.649	0.461	0.000	0.000	102.225
Average		36.923	45.811	0.034	0.041	0.637	0.054	1.253	0.005	13.735	0.298	0.648	0.538	0.004	0.000	
Minimum value		36.061	46.230	0.000	0.022	0.505	0.000	1.008	0.000	11.037	0.193	0.554	0.000	0.000	0.000	
Maximum value		39.237	48.259	0.237	0.067	0.974	0.206	1.704	0.038	16.433	0.339	0.729	0.656	0.017	0.000	

P2d Pyrite/Marcasite																
Analysis #	Sample	Fe	S	Pb	Co	Hg	Ag	Tl	Ni	As	Au	Cu	Sb	Zn	Mo	Total Wt. %
81	UC0606-5000-184.00-15-285	45.128	54.416	0.000	0.070	0.000	0.000	0.000	0.046	0.158	0.000	0.000	0.000	0.000	0.000	99.818
82	UC0606-5000-184.00-15-285	45.374	54.995	0.000	0.131	0.000	0.000	0.047	0.032	0.029	0.019	0.000	0.000	0.000	0.000	100.627
83	UC1079-4850-181.50-38-197	44.550	48.343	0.192	0.051	0.145	0.000	0.068	0.142	3.887	0.039	0.119	0.261	0.000	0.000	97.797
84	UC1079-4850-181.50-38-197	44.896	49.088	0.191	0.052	0.209	0.000	0.159	0.127	2.777	0.029	0.084	0.329	0.000	0.000	97.941
85	UC1079-4850-181.50-38-197	42.402	46.997	0.134	0.049	0.295	0.000	0.299	0.000	5.012	0.124	0.317	1.337	0.000	0.000	96.966
86	UC1079-4850-181.50-38-85	43.812	52.120	0.000	0.057	0.047	0.000	0.000	0.000	0.289	0.026	0.013	0.000	0.000	0.000	96.364
87	UC1079-4850-181.50-38-85	44.932	52.568	0.000	0.050	0.032	0.000	0.000	0.031	0.028	0.000	0.016	0.000	0.000	0.000	97.657
88	UC1079-4850-181.50-38-85	43.909	51.416	0.000	0.062	0.000	0.111	0.000	0.113	1.891	0.000	0.012	0.000	0.000	0.000	97.514
89	UC1079-4850-181.50-38-85	44.149	52.369	0.000	0.078	0.000	0.000	0.000	0.237	0.537	0.000	0.011	0.000	0.000	0.000	97.381
90	UC1079-4850-181.50-38-95	45.556	54.051	0.235	0.081	0.061	0.000	0.000	0.148	0.000	0.000	0.000	0.000	0.000	0.000	100.132
91	UC1079-4850-181.50-38-95	45.329	52.198	0.193	0.102	0.000	0.000	0.053	0.143	0.000	0.000	0.022	0.000	0.000	0.000	98.040
92	UC1079-4850-181.50-38-95	45.239	54.605	0.147	0.053	0.000	0.000	0.000	0.011	0.294	0.000	0.016	0.000	0.000	0.000	100.365

EMP trace element data of Fe-sulfide minerals.

P2d	Pyrite/Marcasite (cont)	Fe	S	Pb	Co	Hg	Ag	Tl	Ni	As	Au	Cu	Sb	Zn	Mo	Total Wt. %
93	UC1079-4850-181.50-38-95	44.664	54.917	0.203	0.049	0.105	0.000	0.000	0.011	0.000	0.000	0.000	0.000	0.011	0.000	99.960
94	UC1079-4850-181.50-38-95	44.772	52.908	0.208	0.083	0.000	0.000	0.068	0.214	0.000	0.000	0.000	0.000	0.000	0.000	98.253
95	UC1079-4850-181.50-38-95	44.270	54.211	0.260	0.067	0.036	0.000	0.112	0.252	1.192	0.000	0.073	0.000	0.000	0.000	100.423
96	UC1084-4850-181.50-41-197	43.776	54.110	0.129	0.042	0.000	0.000	0.046	0.000	2.291	0.018	0.073	0.097	0.000	0.000	100.582
97	UC1084-4850-181.50-41-197	43.762	54.427	0.179	0.028	0.000	0.000	0.101	0.000	1.674	0.018	0.057	0.032	0.000	0.000	100.278
98	UC1084-4850-181.50-41-197	44.138	54.467	0.265	0.044	0.000	0.000	0.000	0.000	2.461	0.038	0.086	0.044	0.000	0.000	101.543
99	UC1084-4850-181.50-41-197	44.311	55.206	0.340	0.047	0.000	0.000	0.080	0.014	0.219	0.036	0.023	0.000	0.000	0.000	100.276
100	UC1084-4850-181.50-41-197	42.530	50.230	0.261	0.049	0.000	0.000	0.000	0.000	3.305	0.000	0.000	0.051	0.000	0.000	96.506
101	UC0606-5000-184.00-15-225	43.095	52.408	0.189	0.058	0.254	0.140	0.398	0.259	6.681	0.029	0.087	0.467	0.000	0.000	104.065
102	UC0606-5000-184.00-15-225	45.746	53.820	0.239	0.080	0.000	0.000	0.074	0.172	0.320	0.000	0.027	0.000	0.000	0.000	100.478
103	UC0606-5000-184.00-15-225	44.693	52.629	0.201	0.061	0.069	0.000	0.079	0.208	2.363	0.000	0.021	0.137	0.000	0.000	100.461
104	UC0606-5000-184.00-15-225	45.215	54.158	0.197	0.065	0.070	0.000	0.046	0.217	1.761	0.000	0.000	0.079	0.114	0.000	101.922
105	UC1079-4850-181.50-38-149	43.964	50.478	0.194	0.044	0.000	0.000	0.122	0.014	2.953	0.000	0.043	0.265	0.000	0.000	98.077
106	UC1079-4850-181.50-38-149	45.023	50.520	0.227	0.060	0.000	0.000	0.070	0.086	0.050	0.000	0.000	0.000	0.000	0.000	96.036
107	UC1084-4850-181.50-41-197	42.067	49.988	0.086	0.051	0.177	0.000	0.486	0.000	4.269	0.124	0.304	0.266	0.000	0.000	97.818
108	UC1084-4850-181.50-41-197	44.424	51.212	0.162	0.044	0.000	0.000	0.085	0.000	2.184	0.038	0.094	0.074	0.000	0.000	98.317
109	UC1084-4850-181.50-41-197	45.101	51.405	0.198	0.056	0.000	0.000	0.049	0.000	2.448	0.000	0.039	0.037	0.000	0.000	99.333
110	UC1084-4850-181.50-41-197	45.037	52.143	0.131	0.045	0.000	0.000	0.000	0.000	2.474	0.022	0.049	0.090	0.000	0.000	99.991
111	UC1079-4850-181.50-38-176	45.340	54.977	0.201	0.043	0.058	0.000	0.000	0.026	0.542	0.022	0.019	0.000	0.013	0.000	101.241
112	UC1079-4850-181.50-38-176	43.995	51.752	0.191	0.046	0.066	0.000	0.044	0.072	0.700	0.000	0.063	0.057	0.009	0.000	96.995
113	UC1079-4850-181.50-38-176	44.604	51.317	0.172	0.046	0.032	0.091	0.000	0.066	0.565	0.000	0.015	0.000	0.000	0.000	96.908
114	UC1079-4850-181.50-38-176	45.442	52.790	0.219	0.046	0.000	0.000	0.038	0.038	0.533	0.000	0.039	0.000	0.000	0.000	99.145
115	UC1079-4850-181.50-38-176	45.731	53.162	0.233	0.042	0.000	0.000	0.000	0.027	0.531	0.025	0.019	0.000	0.000	0.000	99.770
116	UC1079-4850-181.50-38-197	42.680	51.824	0.210	0.060	0.459	0.000	0.055	0.102	4.437	0.039	0.161	0.435	0.000	0.000	100.462
117	UC1079-4850-181.50-38-197	44.409	51.870	0.144	0.059	0.000	0.498	0.000	0.054	0.000	0.000	0.000	0.000	0.000	0.000	97.034
118	UC1079-4850-181.50-38-197	44.523	51.559	0.129	0.044	0.000	0.000	0.000	0.018	0.478	0.000	0.000	0.000	0.000	0.000	96.751
119	UC1079-4850-181.50-38-197	43.257	50.289	0.199	0.054	0.357	0.000	0.000	0.099	3.409	0.057	0.106	0.266	0.000	0.000	98.093
120	UC0519-4850-173.50-15-72	45.523	54.790	0.267	0.045	0.000	0.000	0.000	0.000	0.531	0.000	0.000	0.000	0.000	0.000	101.156
121	UC0519-4850-173.50-15-72	45.522	53.553	0.204	0.059	0.000	0.000	0.000	0.000	0.536	0.000	0.000	0.000	0.000	0.000	99.874

EMP trace element data of Fe-sulfide minerals.

P2d Pyrite/Marcasite (cont)	Fe	S	Pb	Co	Hg	Ag	Tl	Ni	As	Au	Cu	Sb	Zn	Mo	Total Wt. %
122 UC0519-4850-173.50-15-72	45.170	53.286	0.210	0.046	0.000	0.000	0.000	0.000	0.543	0.000	0.000	0.000	0.000	0.000	99.255
123 UC0519-4850-173.50-15-72	43.921	51.797	0.261	0.045	0.139	0.000	0.159	0.107	2.773	0.000	0.017	0.122	0.000	0.000	99.341
124 UC0519-4850-173.50-15-72	44.544	51.697	0.259	0.038	0.000	0.000	0.000	0.000	0.520	0.000	0.000	0.000	0.000	0.000	97.058
125 UC0519-4850-173.50-15-72	44.403	52.533	0.296	0.079	0.000	0.000	0.000	0.735	0.640	0.000	0.000	0.000	0.000	0.000	98.686
126 UC1075-4655-164.00-06-86	44.338	53.150	0.249	0.039	0.000	0.000	0.000	0.000	2.635	0.000	0.355	0.173	0.000	0.000	100.939
127 UC1075-4655-164.00-06-86	43.901	52.593	0.249	0.033	0.000	0.000	0.000	0.000	2.392	0.000	0.276	0.134	0.000	0.000	99.578
128 UC1075-4655-164.00-06-86	43.566	54.285	0.242	0.059	0.000	0.000	0.000	0.000	2.291	0.015	0.312	0.225	0.000	0.000	100.995
129 UC1075-4655-164.00-06-86	44.025	52.915	0.210	0.050	0.000	0.000	0.000	0.000	2.347	0.000	0.317	0.215	0.000	0.000	100.079
130 UC1075-4655-164.00-06-90	44.466	54.530	0.244	0.037	0.000	0.000	0.000	0.000	2.031	0.000	0.052	0.136	0.000	0.000	101.496
131 UC1075-4655-164.00-06-90	44.581	54.872	0.283	0.054	0.042	0.000	0.000	0.000	1.615	0.000	0.051	0.142	0.000	0.000	101.640
132 UC1075-4655-164.00-06-112	44.970	56.057	0.207	0.040	0.000	0.000	0.051	0.000	0.000	0.000	0.000	0.000	0.000	0.000	101.325
133 UC1075-4655-164.00-06-112	44.687	56.154	0.252	0.045	0.000	0.000	0.000	0.000	0.000	0.000	0.000	0.000	0.000	0.000	101.138
134 UC1075-4655-164.00-06-112	44.692	57.368	0.212	0.059	0.000	0.093	0.061	0.016	0.327	0.000	0.000	0.000	0.000	0.000	102.828
135 UC1075-4655-164.00-06-112	43.938	55.864	0.246	0.043	0.000	0.000	0.097	0.000	0.000	0.000	0.000	0.000	0.000	0.000	100.188
136 UC1075-4655-164.00-06-112	44.953	55.768	0.224	0.055	0.000	0.000	0.000	0.000	0.000	0.000	0.000	0.000	0.000	0.000	101.000
137 UC1075-4655-164.00-06-112	43.282	54.885	0.154	0.055	0.000	0.000	0.000	0.018	1.630	0.000	0.525	0.217	0.000	0.000	100.766
138 UC1075-4655-164.00-06-112	43.606	54.068	0.251	0.053	0.000	0.000	0.000	0.000	1.833	0.000	0.543	0.277	0.000	0.000	100.631
139 UC0845-4850-160.0-13-32	44.269	50.413	0.176	0.046	0.103	0.000	0.110	0.000	1.951	0.000	0.022	0.247	0.000	0.000	97.337
140 UC1079-4850-181.50-38-95	46.618	50.827	0.275	0.109	0.000	0.000	0.061	0.172	1.139	0.000	0.000	0.000	0.000	0.000	99.201
141 UC1079-4850-181.50-38-64	44.474	53.728	0.000	0.056	0.000	0.000	0.000	0.024	0.524	0.000	0.000	0.000	0.000	0.000	98.806
142 UC1079-4850-181.50-38-64	44.786	53.515	0.000	0.025	0.000	0.000	0.000	0.000	1.154	0.017	0.000	0.000	0.000	0.000	99.497
Average	44.453	52.913	0.184	0.055	0.044	0.015	0.050	0.065	1.454	0.012	0.073	0.100	0.002	0.000	
Minimum value	42.067	46.997	0.000	0.025	0.000	0.000	0.000	0.000	0.000	0.000	0.000	0.000	0.000	0.000	
Maximum value	46.618	57.368	0.340	0.131	0.459	0.498	0.486	0.735	6.681	0.124	0.543	1.337	0.114	0.000	

EMP trace element data of Fe-sulfide minerals.

P3 Marcasite

Analysis #	Sample	Fe	S	Pb	Co	Hg	Ag	Tl	Ni	As	Au	Cu	Sb	Zn	Mo	Total Wt. %
143	UC1079-4850-181.50-38-197	47.701	48.028	0.000	0.049	0.000	0.000	0.000	0.010	1.555	0.030	0.000	0.000	0.000	0.000	97.373
144	UC1079-4850-181.50-38-197	44.474	53.728	0.000	0.056	0.000	0.000	0.000	0.024	0.524	0.000	0.000	0.000	0.000	0.000	98.806
145	UC1079-4850-181.50-38-197	44.786	53.515	0.000	0.052	0.000	0.000	0.000	0.000	1.154	0.017	0.000	0.000	0.000	0.000	99.524
146	UC1079-4850-181.50-38-197	45.373	54.235	0.000	0.048	0.000	0.000	0.000	0.000	0.000	0.022	0.000	0.000	0.000	0.000	99.678
147	UC1079-4850-181.50-38-197	44.366	53.179	0.000	0.058	0.000	0.000	0.000	0.008	0.000	0.000	0.000	0.000	0.000	0.000	97.611
Average		45.340	52.537	0.000	0.053	0.000	0.000	0.000	0.008	0.647	0.014	0.000	0.000	0.000	0.000	
Minimum value		44.366	48.028	0.000	0.048	0.000	0.000	0.000	0.000	0.000	0.000	0.000	0.000	0.000	0.000	
Maximum value		47.701	54.235	0.000	0.058	0.000	0.000	0.000	0.024	1.550	0.030	0.000	0.000	0.000	0.000	

## **APPENDIX 6**



## CLUSTER ANALYSIS OF SULFIDE GEOCHEMISTRY

### K-Means Clustering

K-means clustering requires that the number of desired clusters is first selected. Using this technique, the samples were distributed between two clusters. The samples were then distributed between two groups by minimizing the variance within each group and maximizing the variance between the groups. Prior to the cluster analysis, the data were standardized. Standardization involves first subtracting the mean from each variable (i.e. element) and then dividing the variable by the standard deviation. The standardization procedure results in a variance of one for each variable, thereby assigning the same influence on the analysis to each of the variables (Wold et al., 1987). Without standardization, cluster analysis would be highly weighted by the concentrations of Fe and S because these concentrations are several orders of magnitude greater than the other trace elements.

## REFERENCES

- Adkins, A. R., and Rota, J. C., 1984, Sediment-hosted gold deposits, the general geology of the Carlin gold mine, *in* Johnson, J. L., ed., *Exploration for Ore Deposits of the North American Cordillera: Association for Exploration Geochemists, Guidebook*, v. 1, Reno, Nevada, p. 17-23.
- Alvarez-A., A., and Noble, D. C., 1988, Sedimentary rock-hosted disseminated precious metal mineralization at Purisima Concepcion, Yauricocha district, central Peru: *Economic Geology*, v. 83, p. 1368-1378.
- Allen, E. T., Crenshaw, J. L., and Larsen, E. S., 1912, The mineral sulphides of iron: *American Journal of Science*, v. 33, p. 169-236.
- Allen, E. T., Crenshaw, J. L., and Merwin, H. E., 1914, Effect of temperature and acidity in the formation of marcasite (FeS<sub>2</sub>) and wurtzite (ZnS): *American Journal of Science*, v. 38, p. 393-421.
- Arehart, G. B., Chrysosoulis, S. L., and Kesler, S. E., 1993a, Gold and arsenic in iron sulfides from sedimentary-hosted disseminated gold deposits: Implications for depositional processes: *Economic Geology*, v. 88, p. 171-185.
- Arehart, G. B., Foland, K. A., Naesar, C. W., and Kesler, S. E., 1993b, <sup>40</sup>Ar/<sup>39</sup>Ar, K/Ar, and fission track geochronology of sediment-hosted disseminated gold deposits at Post/Betze, Carlin trend, northeastern Nevada: *Economic Geology*, v. 88, p. 622-646.
- Arehart, G. B., 1996, Characteristics and origin of sedimentary-hosted disseminated gold deposits: a review: *Ore Geology Review*, v. 11, p. 383-403.
- Ashley, R. P., Cunningham, C. G., Bostick, N. H., Dean, W. E., and Chou, I. M., 1991, Geology and geochemistry of three sedimentary-rock-hosted disseminated gold deposits in Guizhou Province, People's Republic of China: *Ore Geology Review*, v. 6, p. 133-151.
- Bagby, W. C., and Berger, B. R., 1985, Geologic characteristics of sediment-hosted disseminated precious-metal deposits in the western United States, *in* Berger, B. R., and Bethke, P. M., eds., *Reviews in Economic Geology*, v. 2, *Geology and Geochemistry of Epithermal Systems: Society of Economic Geologists*, El Paso, Texas, p. 169-202.
- Bakken, B. E., and Einaudi, M., 1986, Spatial and temporal relation between wall rock alteration and gold mineralization, main pit, Carlin gold mine, Nevada, USA, *in* A. J. MacDonald, ed., *Gold '86, Willowdale Ontario*, Konsult International, p. 388-403.
- Bakken, B. M., Hochella, M. F. Jr., Marshall, A. F., and Turner, A. M., 1989, High-resolution microscopy of gold in unoxidized ore from the Carlin mine, Nevada: *Economic Geology*, v. 84, p. 171-179.
- Bakken, B. M., 1990, Gold mineralization, wall-rock alteration, and the geochemical evolution of the hydrothermal system in the main ore-body, Carlin mine: Unpublished Ph.D. dissertation, Stanford, CA, Stanford University, 236 p.

- Bakken, B. M., Fleming, R. H., and Hochella, M. F., Jr., 1991, High-resolution microscopy of auriferous pyrite for the Post deposit, Carlin district, Nevada, *in* Hausen, D. M., Petruk, W., Hagni, R. D., and Vasiliou, A., eds., *Process Mineralogy XI: Characterization of metallurgical and recyclable products: The Minerals, Metals, and Materials Society, Warrendale, Pennsylvania*, p. 13-23.
- Berentsen, E. J., Nanna, R. F., Hazlitt, J. S., and Estes, L. D., 1996, Discovery and geology of the Turquoise Ridge gold deposit: *Mining Engineering*, v. 48, no. 10, p. 31-35.
- Berger, B. R., and Taylor, B. E., 1980, Pre-Cenozoic normal faulting in the Osgood Mountains, Humboldt County, Nevada: *Geology*, v. 8, p. 594-598.
- Botinelly, T., Neuergurg, G. J. and Conklin, N. M., 1973, Galkhaite, (Hg, Cu, Tl, Zn)(As, Sb) S<sub>2</sub>, from the Getchell Mine, Humboldt County, Nevada: *Journal of Research of the United States Geological Survey*, v. 1, no. 5, p. 515-517.
- Brownlow, A. H., 1996, *Geochemistry*: Boston University, Prentice Hall, New Jersey, 580 p.
- Bruhn, F., 1995, Combined trace element microanalyses and cathodoluminescence studies: Development of a data acquisition method for the Bochum proton microprobe (PIXIE) and case studies in sedimentary geology [Ph.D. thesis]: Univeritat Bochum Germany, 177 p.
- Bürg, G. H., 1930, Die Sichtbarmachung des Feinverteilten Goldes in Goldhöffigern Erzen und ihre Wirtschaftliche Bedeutung: *Metall u.*, v. 27, p. 333-338.
- Christensen, O. D., 1993, Carlin trend geological overview, *in* Christensen, O. D., ed., *Disseminated gold deposits of the Carlin Trend, Nevada*, Society of Economic Geologists Guidebook Series 18, Denver, p. 12-26.
- Chryssoulis, S. L., 1989, Ion probe microanalysis of gold in common sulphide minerals and implications for enhanced gold recovery from refractory gold ores: *Surface Science Western, University of Western Ontario, CANMET Contract Report no. 79037-01-SS*, 380 p.
- Chryssoulis, S. L., 1990, Detection and quantification of "invisible" gold by microprobe techniques, *in* Hausen, D. M., Halbe, D. N., Petersen, E. U., and Tafuri, W. J, eds., *Gold '90 Symposium: Society for Mining, Metallurgy, and Exploration, Inc., Salt Lake City, Utah, February 26 to March 1*, p. 323-331.
- Cline, J. S., 2001, Timing of gold and arsenic-sulfide mineral deposition at the Getchell Carlin-type gold deposit, north-central Nevada: *Economic Geology*, v. 96, p. 75-90.
- Cline, J. S., and Hofstra, A. H., 2000, Ore fluid evolution at the Getchell Carlin-type gold deposit, Nevada, USA: *European Journal of Mineralogy*, v.12, p. 195-212.
- Cline, J. S., Hofstra, A., Landis, G., and Rye, R. O., 1997, Ore fluids at the Getchell Carlin-Type gold deposit, north-central Nevada, *in* Vikre, P., Thompson, T. B., Bettles, K., Christensen, O., and Parratt, R., eds., *Carlin-type gold deposits field conference: Society of Economic Geologists, Guidebook*, v. 28, p. 155-166.
- Coney, P. J., 1978, Basin-range structure in western North America, *in* Smith, R. B., and Eaton, G. P., eds., *Basin-range structure in Western North America: Geological Society of America, Memoir 152*, p. 33-48.
- Cook, H. J., and Chryssoulis, S. L., 1990, Concentrations of "invisible gold" in common sulfides: *Canadian Mineralogist*, v. 28, p. 1-16.
- Deer, W. A., Howie, R. A., and Zussman, J., 1966, *An introduction to the rock-forming minerals*: Longman House, Burnt Mill, Essex, England, 528 p.

- Dickinson, W. R., 1992, Cordilleran sedimentary assemblages, in Burchfiel, B. C., Lipman, P. W., and Zoback, M. L. eds., *The Cordilleran Orogen: Conterminous U. S.*: Geological Society of America, v. G-3, p. 539-551.
- Driesner, D., and Coyner, A., 2001, Major mines of Nevada 2000, mineral industries in Nevada's economy: Nevada Bureau of Mines and Geology, Special Publication P-12, p. 1-28.
- Dunning, G. E., 1988, Calcium arsenate minerals new to the Getchell Mine, Nevada: *The Mineralogical Record*, v. 19, p. 253-257.
- Erickson, R. L., and Marsh, S. P., 1974, Geologic map of the Iron Point quadrangle, Humboldt County, Nevada: U.S.G.S. Geologic Quadrangle Map GQ-1175, scale 1:24000.
- Ferdock, C. G., Castor, S. B., Leonardson, R. W., and Collins, T., 1997, Mineralogy and paragenesis of ore stage mineralization in the Betze gold deposit, Goldstrike mine, Eureka County, Nevada: *Society of Economic Geologists, Guidebook*, v. 28, p. 75-86.
- Ferguson, H. G., Muller, S. W., and Roberts, R. J., 1951, *Geology of the Winnemucca Quadrangle, Nevada*: U.S. Geological Survey Quadrangle Map GQ-11.
- Finney, S. C., Perry, B. D., and Cooper, J. D., 1989, Depositional history of the Vinini Formation – results from the type area, Roberts Mountains, Nevada: *Geological Society of America Abstracts with Programs*, v. 21, no.5, p. 78.
- Fleet, M. E., MacLean, P. J. and Barbier, J., 1989, Oscillatory zoned As-bearing pyrite from strata-bound and stratiform gold deposits: An indicator of ore fluid evolution: *Economic Geology Monograph* 6, p. 356-362.
- Fleet, M. E., and Mumin, A. H., 1997, Gold-bearing arsenian pyrite, marcasite and arsenopyrite from Carlin Trend gold deposits and laboratory synthesis: *American Mineralogist*, v. 82, p. 182-193.
- Fleming, R. H. and Bakken, B. M., 1995, Isotope ratio and trace element imaging of pyrite grains in gold ores: *International Journal of Mass Spectrometry and Ion Processes*, v. 143, p. 213-224.
- Fricke, H. C., Wickham, S. M., and O'Neil, J. R., 1992, Oxygen and hydrogen isotope evidence for meteoric water infiltration during mylonitization and uplift in the Ruby Mountains-East Humboldt Range core complex, Nevada: *Contributions to Mineralogy and Petrology*, v. 111, p. 203-211.
- Gans, P. B., Mahood, G. A., and Schermer, E., 1989, Synextensional magmatism in the Great Basin: *Geological Society of America Special Paper* 233, 53 p.
- Garwin, S. L., Hendri, D., and Lauricella, P. F., 1995, The geology of the Mesel deposit, north Sulawesi, Indonesia: *Proceedings of the PACRIM '95 conference*, p. 221-226.
- Getchell Gold Corporation, 1997, Yesterday, today and tomorrow, Getchell operations: Unpublished Private Report, 195 p.
- Giggenbach, W. F., 1974, Equilibria involving polysulfide ions in aqueous solutions up to 240 °C: *Inorganic Chemistry*, v. 13, p. 1724-1730.
- Goldhaber, M. B., and Stanton, M. R., 1987, Experimental formation of marcasite at 150-200°C: implications for carbonate hosted Pb/Zn deposits (abstract), *Geological Society of America Abstracts, Program* 19.

- Groff, J. A., Heizler, M. T., McIntosh, W. C., and Norman, D. I., 1997,  $^{40}\text{Ar}/^{39}\text{Ar}$  dating and mineral paragenesis of Carlin-type gold deposits along the Getchell Trend, Nevada: Evidence for Cretaceous and Tertiary gold mineralization: *Economic Geology*, v. 92, p. 601-622.
- Hauff, P. L., Kruse, F. A., and Madrid, R. J., 1990, Defining gold ore zones zoning illite polytypes, in Raines, G. L., Lisle, R. E., Schafer, R. W., and Wilkinson, W. H., eds., *Geology and Ore Deposits of the Great Basin: Geological Society of Nevada Symposium Proceedings*, Reno, Nevada, p. 239-247.
- Hausen, D. M., and Kerr, P. F., 1968, Fine gold occurrence at Carlin, Nevada, in *Ore Deposits in the United States 1933/1967*, in Ridge, J. D., ed.: Graton-Sales Volume, Society of Mining Engineers, AIME, New York, p. 909-940.
- Hausen, D. M., 1981, Process mineralogy of auriferous pyritic ore at Carlin, Nevada, in Hausen, D. M., and Park, W. C., eds., *Process mineralogy, extractive metallurgy, mineral exploration, energy resources: Metallurgy Society of American Institute of Mining Engineers*, Warrendale, Pennsylvania, p. 271-289.
- Hausen, D. M., and Park, W. C., 1985, Observations on the association of gold mineralization with organic matter in Carlin-type ores: Denver Region Exploration Geologists Society Symposium, Denver, Colorado, April 25-26, 1985, *Proceedings*, v. 3, p. 119-136.
- Hayward, C. L., 1998, Cathodoluminescence of ore and gangue minerals and its application on the mineral industry, in Cabri, L. J., and Vaughan, D. J., eds., *Modern Approaches to Ore and Environmental Mineralogy: Mineralogical Association of Canada, Short Course Series*, Ottawa, Ontario, v. 27, p. 199-224.
- Hofstra, A. H., Leventhal, J. S., Northrop, H. R., Landis, G. P., Rye, R. O., Birak, D. J., and Dahl, A. R., 1991, Genesis of sediment-hosted disseminated-gold deposits by fluid mixing and sulfidization: Chemical-reaction-path modeling of ore-depositional processes documented in the Jerritt Canyon district, Nevada: *Geology*, v. 19, p. 36-40.
- Hofstra, A. H., 1994, *Geology and genesis of the Carlin-type gold deposits in the Jerritt Canyon district, Nevada: Unpublished Ph.D. dissertation, University of Colorado, Boulder*, 719 p.
- Hofstra, A. H., Snee, L. W., Rye, R. O., Folger, H. W., Phinisey, J. D., Loranger, R. J., Dahl, A. R., Naeser, C. W., Stein, H. J., and Lewchuk, M., 1999, Age constraints on Jerritt Canyon and other Carlin-type gold deposits in the western United States - relationships to mid-Tertiary extension and magmatism: *Economic Geology*, v. 94, p. 769-802.
- Hotz, P. W., and Willden, R., 1964, *Geology and mineral deposits of the Osgood Mountains quadrangle, Humboldt County, Nevada: U.S. Geological Survey Professional Paper 431*, 128 p.
- Huston, D. L., Sie, S. H., Suter, G. F., Cooke, D. R., and Both, R. A., 1995, Trace elements in sulfide minerals from eastern Australian volcanic-hosted massive sulfide deposits: Part I. Proton microprobe analyses of pyrite, chalcopyrite, and sphalerite, and Part II. Selenium levels in pyrite: Comparison with  $\delta^{34}\text{S}$  values and implications for the source of sulfur in volcanogenic hydrothermal systems: *Economic Geology*, v. 90, p. 1167-1196.
- Ilchik, R. P., 1990, *Geology and geochemistry of the Vantage Gold deposits, Alligator Ridge Bald Mountain Mining District: Economic Geology*, v. 85, p. 50-75.

- Irkamuddin, M., Besse, L., and Nordstrom, P. M., 1986, Thallium in the Carlin-type gold deposits: *Applied Geochemistry*, v. 1, p. 493-502.
- Joralemon, P., 1951, The occurrence of gold at the Gatchell Mine, Nevada: *Economic Geology*, v. 46, no. 3, p. 267-310.
- Kearsley, A., and Wright, P., 1988, Geological Applications of Scanning Cathodoluminescence Imagery, in Goodhew, P. J., Humphreys, F. J., and Beanland, R., eds.: *Electron Microscopy and Analysis*, 2<sup>nd</sup> edition, Taylor and Francis, London, p. 49-51.
- Kuehn, C. A., and Rose, A. W., 1995, Carlin gold deposits, Nevada: Origin in a deep zone of mixing between normally pressured and overpressured fluids: *Economic Geology*, v. 90, p. 17-36.
- Lovering, T. S., 1972, Jasperoid in the United States - it's characteristics, origin, and economic significance: U.S. Geological Survey Professional Paper 710, 164 p.
- Landis, G. P., and Hofstra, A. H., 1991, Fluid inclusion gas chemistry as a potential mineral exploration tool: Case studies from Creede, Co., Jerrit Canyon, NV, Coeur d'Arline district, ID and MT, southern Alaska mesothermal veins, and mid-continent MVT'S: *Journal of Geochemical Exploration*, v. 42, p. 25-59.
- Madden-McGuire, D. J., and Marsh, S. P., 1991, Lower Paleozoic host rocks in the Gatchell gold belt: Several distinct allochthons or a sequence of continuous sedimentation?: *Geology*, v. 19, p. 845-851.
- Maher, B. J., Browne, Q. J., and McKee, E. H., 1993, Constraints on the age of gold mineralization and metallogenesis in the Battle Mountain-Eureka mineral belt, Nevada: *Economic Geology*, v. 88, p. 469-478.
- Mao, S. H., 1991, Occurrence and distribution of invisible gold in a Carlin-type gold deposit in China: *American Mineralogist*, v. 76, 1964-1972.
- Marshall, D. J., 1988, Cathodoluminescence of Geological Materials: Unwin, Boston, Hyman, p. 1-145.
- McCollum, L. B., and McCollum, M., 1990, Paleozoic Rocks of the Osgood Mountains, Nevada, in Raines, G. L., Lisle, R. E., Schafer R. W., and Wilkinson, W. H. eds., *Geology and Ore Deposits of the Great Basin: The United States Geological Survey Symposium Proceedings*, p. 735-738.
- Merriam, C. W., and Anderson, C. A., 1942, Reconnaissance survey of the Roberts Mountains, Nevada: *Geological Society of America Bulletin*, v. 53, p. 1675-1728.
- Miller, E. L., Holdsworth, B. K., Whiteford, W. B., and Rodgers, D., 1984, Stratigraphy and structure of the Schoonover sequence, northeastern Nevada: Implications for Paleozoic plate-margin tectonics: *Geological Society of America Bulletin*, v. 95, p. 1063-1076.
- Miller, E. L., Gans, P. B., Wright, J. E., and Sutter, J. F., 1988, Metamorphic history of the east-central Basin and Range province: Tectonic setting and relationships to magmatism, in Ernst, W. G., ed., *Metamorphism and crustal evolution of the western United States*, Rubey Volume 7: Prentice-Hall, Englewood Cliffs, NJ, p. 649-682.
- Miller, E. L., Miller, M. M., Stevens, C. H., Wright, J. E., and Madrid, R., 1992, Plate Paleozoic paleogeographic and tectonic evolution of the western US cordillera: *Geological Society of America, The Geology of North America*, Boulder, Colorado, v. G-3, p. 57-106.

- Murowchick J. B., and Barnes, H. L., 1986, Marcasite precipitation from hydrothermal solutions: *Geochemica et Cosmochemica Acta*, v. 50, p. 2615-2629.
- Murowchick J. B., and Barnes, H. L., 1987, Effects of temperature and degree of supersaturation on pyrite morphology: *American Mineralogist*, v. 72, p. 1241-1250.
- Murowchick, J. B., 1992, Marcasite inversion and the petrographic determination of pyrite ancestry: *Economic Geology*, v. 87, p. 1141-1152.
- Perny, B., Ramseyer, K., Mullis, J., and Pankrath, R., 1992, Microdistribution of Al, Li, and Na in alpha quartz: Possible causes and correlation with short-lived cathodoluminescence: *American Mineralogist*, v. 77, p. 534-544.
- Radtke, A. S., and Dickson, F. W., 1976, Structural controls and genesis of Carlin-type gold deposits in the evolution of the Basin and Range province: AIME preprint, Las Vegas, Nevada, AIME Annual Meeting, 8p.
- Radtke, A. S., Rye, R. O., and Dickson, F. W., 1980, Geology and stable isotope studies of the Carlin gold deposit, Nevada: *Economic Geology*, v.75, p. 641-672.
- Radtke, A. S., 1985, Geology of the Carlin deposit, Nevada: U.S. Geological Survey Professional Paper 1267, 124 p.
- Raiswell, R. and Plant, J., 1980, The incorporation of trace elements into pyrite during diagenesis of Black Shales, Yorkshire England: *Economic Geology*, v. 75, p. 684-699.
- Rees, M. N., and Rowell, A. J., 1980, Preble Formation, a Cambrian outer continental shelf deposit in Nevada: *Brigham Young University Geology Studies*, v. 27, p. 1-8.
- Roberts, R. J., Hotz, P. E., Gilluly, J., and Ferguson, H. G., 1958, Paleozoic rocks of north-central Nevada: *American Association of Petroleum Geologists*, v. 42, no. 12, p. 2813-2857.
- Roberts, R. J., Radtke, A. S., Coats, R. R., Silberman, M. L., and McKee, E. H., 1971, Gold-bearing deposits in north-central Nevada and southwestern Idaho: with a section on periods of plutonism in north-central Nevada: *Economic Geology*, v. 66, p. 14-33.
- Roedder, E., 1968, The non-colloidal origin of 'colloform' textures in sphalerite ores: *Economic Geology*, v. 63, no. 5, p. 451-471.
- Rota, J. C., 1993, Geology and related studies at the Gold Quarry Deposit, Nevada, in Christensen, O. D., ed., *Gold Deposits of the Carlin Trend: Society of Economic Geologists Guidebook Series*, v. 18, Littleton, Co., p. 67-78.
- Rye, R. O., 1985, A model for the formation of carbonate-hosted disseminated gold deposits based on geologic, fluid inclusion, geochemical and stable-isotope studies on the Carlin and Cortez deposits, Nevada: U.S. Geological Survey Bulletin 1646, p. 35-42.
- Rytuba, J. J., 1985, Geochemistry of hydrothermal transport and deposition of gold and sulfide minerals in Carlin-type gold deposits, in Tooker E. W., ed., *Geologic characteristics of sediment and volcanic-hosted disseminated gold deposits search for an occurrence model: U.S.G.S. Bulletin 1646*, 27-34.
- Saleeby, J. B., and Busby-Spera, C., 1992, Early Mesozoic tectonic evolution of the western U.S. Cordillera, in Burchfield, B. C., Lipman, P. W., and Zoback, M. L., eds., *The Cordilleran Orogeny: Conterminous U.S.: Geological Society of America, The Geology of North America*, Boulder, Colorado, v. G-3, 107-168.

- Savio, D., 1999, Welcome to Placer Dome: <http://www.placerdome.com>, May 27, 1999.
- Schoonen, M. A. A., and Barnes, H. L., 1991, Reactions forming pyrite and marcasite from solution: III. Hydrothermal Processes: *Geochemica et Cosmochemica Acta*, volume. 55, p. 3491-3504.
- Seedorff, E., 1991, Magmatism, extension, and ore deposits of Eocene to Holocene age in the Great Basin - mutual effects and preliminary proposed genetic relationships: *Proceedings from the Geological Society of Nevada Geology and Ore Deposits of the Great Basin Symposium*, Reno, Nevada, p. 133-178.
- Sha, P., 1993, Geochemistry and genesis of sediment-hosted disseminated gold mineralization at the Gold Quarry mine, Nevada: Unpublished Ph.D. dissertation, University of Alabama, 228 p.
- Silberman, M. L., Berger, B. R., and Koski, R. A., 1974, K-Ar age relations of granodiorite emplacement and tungsten and gold mineralization near the Getchell Mine, Humboldt County, Nevada: *Economic Geology*, v. 69, p. 646-656.
- Sillitoe, R. H., and Bonham, H. F. Jr., 1990, Sediment-hosted deposits: Distal products of magmatic-hydrothermal systems: *Geology*, v. 18, no. 2, p.157-161.
- Simon, G., Kesler, S. E., and Chrysosoulis, S., 1999, Geochemistry and textures of gold-bearing arsenian pyrite, Twin Creeks, Nevada: Implications for deposition of gold in Carlin-type deposits: *Economic Geology*, v. 94, p. 405-421.
- STATISTICA for Windows, 1995, V. III: Statistics, 2<sup>nd</sup> Edition, StatSoft Incorporation., p. 3197-3234
- Speed, R. C., 1979, Collided Paleozoic microplate in the Western U.S.; *Journal of Geology*, v. 87, p. 279-292.
- Sprunt, E. S., 1981, Causes of quartz cathodoluminescence colors: *Scanning Electron Microscopy*, v. 1, p. 525-535.
- Stewart, J. H. and Suczek, C. A., 1977, Cambrian and Latest Precambrian paleogeography and tectonics in the western United States, in Stewart, H. J., Stevens, C. H., and Fritsche, A. E., eds., *Paleogeography of the Western United States: Pacific Coast Paleogeography Symposium I: Society of Economic Paleontologists, Pacific Section*, Los Angeles, California, Unites States, p. 1-15.
- Stewart, J. H., 1978, Basin-range structure in western North America, in Smith, R. B., and Eaton, G. P., eds., *Basin-range structure in western North America; a review*: Geological Society of America, Memoir 152, p. 1-34.
- Stolburg, C. S. and Dunning, G. E., 1985, The Getchell Mine, Humboldt County: *The Mineralogical Record*, v. 16, p. 15-23.
- Stenger, D. P., Kesler, S. E., Fortuna, J., and Peltonen, D. R., 1997, Role of sulfidation in deposition of gold, Twin Creeks sediment-hosted micron gold deposit, Nevada, in Vikre, P., Thompson, T. B., Bettles, K., Christensen, O. and Parratt, R., eds., *Carlin-Type Gold Deposits Field Conference: Society of Economic Geologists Guidebook Series*, v. 28, Littleton, Co., p. 147-150.
- Teal, L. and Jackson, M., 1997, Geologic overview of the Carlin-Trend gold deposits and descriptions of recent deep discoveries, in Vikre, P., Thompson, T. B., Bettles, K., Christensen, O., and Parratt, R., eds., *Carlin-Type Gold Deposits Field Conference: Society of Economic Geologists Guidebook Series*, v. 28, Littleton, Co., p. 3-37.



- Tretbar, D., Arehart, G. B., and Christensen, J., 2000, Dating gold deposition in a Carlin-type gold deposit using Rb/Sr methods on the mineral galkhaite: *Geology*, v.28, p. 947-954.
- Wagner, F. E., Marion, P., and Regnard, J. R., 1986, Mössbauer study of the chemical state of gold in gold ores, *Gold 100: Proceedings of the International Conference on Gold*, v. 2: Extractive Metallurgy of Gold, Johannesburg, South Africa, SAIMM, p. 435-443.
- Wells, D. J., and Mullens, T. E., 1973, Gold-bearing arsenian pyrite determined by microprobe analysis, Cortez and Carlin Gold Mines, Nevada: *Economic Geology*, v. 68, p. 187-201.
- Wold, S., Esbensen, K., and Geladi, P., 1987, Principal Component Analysis: *Chemometrics and Intelligent Laboratory Systems*, v. 2, p. 37-52.
- Xu, H., and Veblen, D. R., 1995, Transmission electron microscopy study of optically anisotropic and isotropic hauyne: *American Mineralogist*, v. 80, p. 87-93.

## **VITA**

**Graduate College  
University of Nevada, Las Vegas**

**Kelli D. Weaver**

**Home Address:**

**212 W. Healey St. #101  
Champaign, Illinois 61820**

**Degrees:**

**Bachelor of Science, 1992  
Ohio Wesleyan University**

**Publications:**

**Cline, J. S., Cail, T., Weaver, K. D., and Shigehiro, M., 2000, The geochemistry of the Getchell Carlin-type gold deposit, Nevada [Ext. Abs.]: Geology and ore deposits 2000: The Great Basin and beyond, Program and Abstracts, Geological Society of Nevada, Reno, Nevada, p. 42.**

**Weaver, K. D., and Cline, J. S., 1999, Geochemistry of ore-stage and non-ore pyrite and marcasite from the Getchell Carlin-type gold deposit, Nevada: Geological Society of America Abstracts with Programs, v. 31, n. 6, p. A106.**

**Woitsekhowskaya, M., Cline, J. S., Hemley, J. J., and Weaver, K.D., 1997, Gold and arsenic in iron sulfides from the Getchell deposit, Nevada: Thermodynamic evaluation, international symposium on hydrothermal reactions, Gatlinburg Tennessee, July 20-24.**

**Fryer, K. H., Weaver, K. D., Laubach, S. E., 1991, Apparent inverse metamorphic gradient below a cretaceous thrust sheet in the Maria fold-and thrust belt, western Arizona: Geological Society of America Abstracts with Programs, vol. 23, no. 5.**

**Thesis Title:**

**The Geochemistry of Gold-Bearing and Gold-Free Pyrite and Marcasite from the Getchell Gold Deposit, in Humboldt County, Nevada.**

**Thesis Examination Committee:**

**Chairperson, Dr. Jean S. Cline, Ph. D.  
Committee Member, Dr. Margaret N. Rees, Ph. D.  
Committee Member, Dr. Elizabeth Jacobson, Ph. D.**

**Graduate Faculty Representative, Dr. Barbara A. Luke, Ph. D.**